universität wien

MASTER'S THESIS

Title of the Master's Thesis

„Charging, Detection and Sizing of Aerosol Nanoparticles in Helium and Air“

submitted by

Bernhard Baumgartner, BSc.

in partial fulfilment of the requirements for the degree of

Master of Science (MSc.)

Vienna, 2018

degree programme code as it appears on the student record sheet:	A 066 876
degree programme as it appears on the student record sheet:	Master's Programme Physics
Supervisor	Ass.-Prof. Dr. Paul Winkler

Danksagung

Jedes Wort dieser Arbeit ist zwar von mir geschrieben, aber kein einziges wäre möglich gewesen ohne eine Menge von Menschen, bei welchen ich mich an dieser Stelle bedanken möchte. Dies geht an all jene, die mich vor und während meiner Zeit als Student, insbesondere aber im Zuge der Bestrebungen hinsichtlich meiner Abschlussarbeit, in meinem Leben begleitet haben und begleiten.
Großen Dank möchte ich meinem Betreuer Ass.-Prof. Dr. Paul Winkler aussprechen, welcher stets Zeit, Motivation, kritisches Hinterfragen, und vor allem sichtlich Freude an seiner betreuenden Arbeit bot. Ich danke ihm vielmals, dass ich Teil seines wunderbaren Nanodynamite-Teams sein durfte und mir somit auch die Möglichkeit geboten wurde an der CLOUD11-Messkampagne in Genf und an SAXS-Experimenten in Triest mitwirken zu können.
Des weiteren geht auch ein riesiges Dankeschön an Sophia Brilke, Christian Tauber, insbesondere aber an Paulus Bauer und Dominik Stolzenburg. Deren umfangreiches Wissen zur Aerosolphysik, Programmiertechnik und Dateninterpretation, insbesondere aber deren Willen ihr know-how stets weiterzugeben war nicht nur förderlich, sondern auch unglaublich lehrreich. Man kann sich kein angenehmeres Arbeitsumfeld als das eure wünschen und ich freue mich nicht nur dass wir Kollegen waren, sondern auch Freunde wurden.
Außerdem möchte ich mich bei folgenden Personen bedanken: Mag. Dr. Gerhard Steiner für seinen steten kritischen Input zu den Themen Ladungswahrscheinlichkeiten und der Generation von Aerosolpartikeln, Dr. Anne Maißer für ihre umgehenden fachspezifischen Tipps und Ideen zum Umgang mit dem Electrospray-Generator, Ao.Univ.Prof.i.R. Dr. Wladyslaw Szymanski für die Leihe ebendieses Generators und sämtlicher Aerosolstandards und Peter Kallinger für die Erlaubnis sein Programm zur theoretischen Berechnung der Ladungswahrscheinlichkeiten verwenden zu dürfen.
Ohne meine Familie wäre diese Arbeit trotz allem niemals zustande gekommen. Deshalb möchte ich all meinen Familienmitgliedern, insbesonders aber meiner Mutter, Danke sagen. Ohne deinen und euren Glauben an mich und eure moralische, aber auch finanzielle Unterstüzung wäre diese These niemals möglich gewesen.
Zuletzt möchte ich mich bei meiner Freundin Kerstin Fiedler herzlich bedanken. Mit Rat und Tat stand sie mir zu jeder Tages- und Nachtzeit bei, und es gab kein Tief aus dem sie mich noch nicht herausholen hätte können.

Diese Arbeit ist euch allen gewidmet. Dankeschön.

Abstract

This thesis targets two different, highly-significant issues in current aerosol science. First, physical properties of aerosol nanoparticles carried in helium instead of air are analyzed in both ways, theoretically and experimentally. Second, the performance of two different, cutting-edge instruments aiming for correct size distributions is tested and compared.
Research on both, distribution and growth of aerosol particles with diameters below 10 nm, is inevitable in order to acquire information on potential subsequent growth to cloud condensation nuclei (CCN). Retrieved knowledge further allows assertions on cloud formation processes and possible impact on climate. Corresponding size distribution measurements are often conducted utilizing information of the analyzed aerosol particles' charging state and other quantities, e.g. carrier gas pressure and temperature. Particle sizing is then possible via application of a Differential Mobility Analyzer (DMA), whereas subsequent counting typically happens by using a Condensation Particle Counter (CPC) or a Faraday Cup Electrometer (FCE).
All of these instruments, however, require certain amounts of sample flows, which is why resulting measurements are of ex-situ character. Utilization of the SAXS-technique is believed to retrieve desired size distributions without any major system disturbances. In order to maximize signal-to-noise ratios in related experiments helium-carried particles are analyzed. Two things are consequently inevitable: First, testing and calibrating the above instruments for correct operation when sampling helium. Second, information on charging state of analyzed particles as well as theoretical quantities of helium must be known and implemented into subsequent computations in order to achieve correct size distributions.
The first part of this thesis applies to the complete theoretical background and all concurring experiments introduced in the second paragraph. The second part focuses on the comparison of the DMA-train and the nano-SMPS. The former utilizes six DMAs operating in parallel at fixed voltages, respectively, thus providing related concentrations every second. The latter yields size distributions via continuously scanning voltages applied on the DMA, thereby minimizing the necessary cycle time. The overlapping sizing region of both instruments, i.e. around 6 nm, shows no perfect conformity, which is why closer investigation is of interest.
Experimental results of part I showed good agreement with theoretical computations regarding the calibration of the utilized DMA operating with particle-laden helium. Moreover, a new technique aiming for the quantification of corresponding size-dependent charging probabilities via application of an ion-trap proved to perform flawlessly. Part II highlights the benefit of the DMA-train's operating principle and the need for high-time resolution measurements of particles smaller than 10 nm.

Kurzfassung

Die vorliegende Arbeit behandelt zwei aktuelle Themen der Aerosolwissenschaft. Zunächst werden physikalische Eigenschaften von heliumgetragenen Aerosolpartikeln sowohl theoretisch und experimentell untersucht. Im Anschluss wird die Performance zweier aktueller Messinstrumente, welche jeweils Messungen zu Anzahlgrößenverteilung durchführen, getestet und verglichen.
Forschung an Größenverteilung und Wachstum von Aerosolpartikeln mit Durchmessern kleiner als 10 nm ist unabdingbar, um Information über daraus resultierenden Wolkenkondensationskernen (CCN) zu erhalten. Erhaltenes Wissen erlaubt im Folgenden das Treffen von Aussagen zu Wolkenbildungsprozessen und somit auch klimarelevante Prognosen. Bei hierfür notwendigen Experimenten macht man sich oft Information bezüglich des Ladungszustandes der analysierten Partikel und anderer Größen, so zum Beispiel Druck und Temperatur des Trägergases, zunutze. Dadurch ist die Charakterisierung der Partikel nach ihrer Größe mittels eines differenziellen Mobilitätsanalysators (DMA) möglich, wohingegen anschließendes Zählen durch Verwendung eines Kondensationskernpartikelzählers (CPC) oder eines Faraday Cup Elektrometers (FCE) stattfindet. Sämtliche genannten Instrumente benötigen jedoch einen bestimmten Probestrom, weshalb resultierende Experimente immer ex-situ-Messungen sind. Unter Anwendung der SAXS-Technologie könnten die erwünschten Größenverteilungen jedoch ohne größere Störungen des untersuchten Systems erhalten werden. Zur Maximierung des Signal-Stör-Verhältnisses werden in diesbezüglichen Experimenten heliumgetragene Partikel analysiert. Dies macht jedoch zweierlei Dinge unumgänglich: Erstens müssen sämtiche obigen Instrumente bei Operation mit Helium getest und kalibriert werden. Zweitens muss sowohl Information bezüglich der Ladungszustände der analysierten Partikel, als auch theoretischer Größen von Helium vorhanden sein, und diese in darauffolgende Berechnungen zur korrekten Größenverteilung implementiert werden.
Der erste Teil dieser Arbeit widmet sich dem kompletten theoretischen Hintergrund und sämtlichen vorkommenden Experimenten, welche in dem vorangegangen Absatz vorgestellt wurden. Im zweiten Abschnitt wird der Schwerpunkt auf den Vergleich des DMA-train und des nano-SMPS gesetzt. Das erstgenannte Instrument besteht aus sechs DMAs, welche parallel bei jeweils festgelegten Spannungen operieren und im Folgenden das Messen zugehöriger Konzentrationen jede Sekunde ermöglichen. Das nano-SMPS liefert Größenverteilungen, indem die an den DMA angelegte Spannung kontinuierlich erhöht wird, wodurch die notwendige Laufzeit minimal ist. Der Überlappungsbereich beider Instrumente, welcher in etwa bei 6 nm liegt, weist keine perfekte Übereinstimmung auf, weshalb genauere Untersuchungen von Interesse sind.
Experimentelle Ergebnisse aus Teil I bezüglich der Kalibration des DMAs bei Verwendung von Helium als Trägergas zeigen gute Übereinstimmung mit theoretischen Berechnungen. Des weiteren erwies sich eine neue Technik zur Quantifizierung der größenabhängigen Ladungswahrscheinlichkeit durch Zuhilfenahme einer Ionenfalle als einwandfrei. Teil II hebt sowohl den Vorteil der instrumentellen Technik des DMA-trains, als auch die Notwendigkeit für hoch-zeitauflösende Messungen von Partikeln, deren Durchmesser kleiner als 10 nm sind, hervor.

Table of Contents

1. Introduction

Aerosols are omnipresent in the earth's atmosphere and span size ranges from 1 nm to 100 µm. Physical and chemical reactions between particles and gaseous constituents have high impact on cloud formation, and hence the hydrological cycle and climate. Therein comprised mechanisms and potential consequent outcomes are therefore of great interest and are subject to ongoing research. These processes either occur through primary/direct aerosol particles, i.e. sea spray, sulphates or carbonaceous emission, e.g. emanating from biomass burning, or secondary/indirect contributors. The latter particle type evolves from nucleation through gas-to-particle conversion (new particle formation - NPF) (Kulmala et al., 2013) and subsequent particle growth (Tröstl et al., 2016) that lead to the formation of cloud condensation nuclei (CCN) between 50 nm and 100 nm. This evolution, starting at molecular sizes account for roughly half of all existing CCN, whereas the other half is attributed to primary emissions (Merikanto et al., 2009).

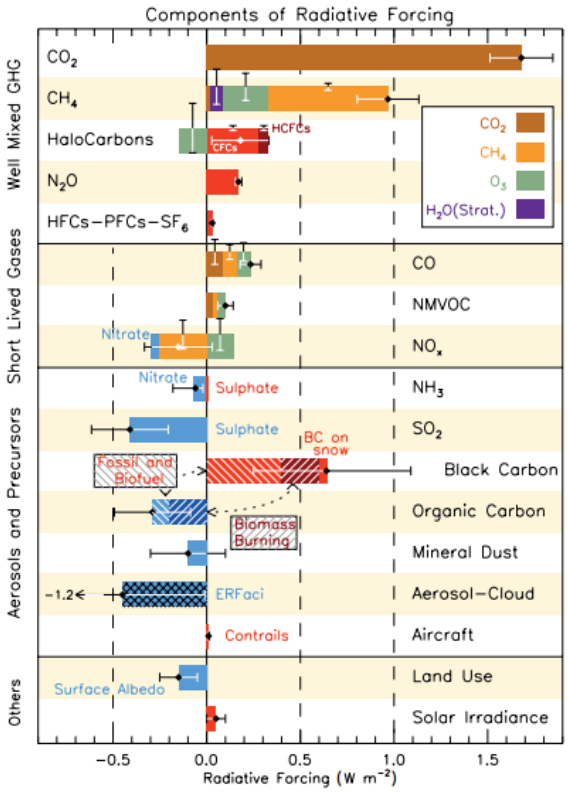

Figure 1.1: Radiative forcing contributions of most important compounds. Aerosols and their precursors are very likely to cause negative forcing, thus have a cooling effect. SOA-particles are not included due to lack of information on their contribution. source: http://www.ipcc.ch/pdf/assessment-report/ar5/wg1/WG1AR5_Chapter08_FINAL.pdf

It is evident, that distinction of aerosol particles is not only a matter of size, but also a question of origin, chemical composition and concentration. Consequently, precise analysis of complex aerosol dynamics and their impact on climate requires consideration of multiple components and yet entails various ambiguities. This becomes apparent when examining *Aerosol-Cloud interactions* and the related error bar in terms of radative forcing in figure 1.1, obtained from the IPCC-report 2013. It is worth noting, that aerosol-driven direct radiative forcing arising from scattering mechanisms of electromagnetic waves is included, however, due to lack of knowledge about their contribution, effects of secondary organic aerosols (SOA) are not taken into account. Another reason for such huge error bars is given by Carslaw et al. (2013), who found natural aerosols to be the major cause for high deviations of indirect radiative forcing, i.e. impact of cloud albedo.
Reconsideration of the above-mentioned processes regarding NPF and CCN, as well as ensuing uncertainties of radiative forcing give rise to closer scrutiny. Among others, this involves knowledge of both, size and concentration of aerosol particles. If continuously obtained and combined, these two quantities provide time-resolved size distributions, which allow even deeper insight into the complex dynamics of nucleation processes (Mäkelä et al., 1997), particle growth (Qi et al., 2015), and atmospheric physics (Jacobson, 2001). Especially investigations of freshly nucleated nano-particles smaller than 10 nm are continuously carried out. (McMurry et al., 2000), (Shi et al., 2001).
Various methods to achieve this data for further calculus, e.g. through analysis of the particles' electrical mobility (Liu, 1975, p.739-762) do exist and are in use, however, continuous improvement is needed. The combination of Differential Mobility Analyzers (DMA) and Faraday Cup Electrometers (FCE) or Condensation Particle Counters (CPC) allow physicists to attain concentrations of particles at one specific diameter. This is done by means of analysing their corresponding electrical mobility via an electric field (DMA) and integrating over the current which is directly proportional to the carried electric charges (FCE) or growing the particles up to sizes that can be detected with optical laser systems (CPC).
However, due to the stepwise decrease of the applied voltage, DMAs often lack of the crucial high time resolution, especially if measurements in rapidly changing environments are desired. Scanning mobility particle sizers (SMPS) reduce this shortcoming in time resolution by continuously increasing the electric field, yet they entail the drawback of subsequent data inversion (Wang and Flagan, 1990). Another approach is the continuous sampling of differently sized particles with multiple DMAs as done by Stolzenburg et al. (2017). Due to significantly enhanced time resolution thus obtained concentrations provide improved statistics, and consequently more precise size-distributions and subsequent computations on particle growth. Since both SMPS and DMA train operate in different size ranges the combination of both instruments allows coverage of the full size range which is needed for quantitative analysis of NPF. However, inspection of concentrations obtained close to the overlapping sizing region shows, that no perfect accordance in signal is given. Part II of this thesis targets this discrepancy and aims for possible explanations.
One major disadvantage of all mentioned measurement methods is their remote character, i.e. the necessity of drawing specific sample flows out of the system of interest into the measurement devices. Optical particle counters (Rosen and Hofmann, 1986) are able to work in-situ and analyse physical particle properties via detection of scattered light. Since particles smaller than 100 nm

do not scatter electromagnetic radiation sufficiently "optical" detection below this size is usually not possible.

In order to minimise this lower detection threshold the need of electromagnetic radiation with comparatively short wavelength is evident and investigated. X-rays have been used in various medical (Brooks and Chiro, 1975) and physical research methods (Als-Nielsen and McMorrow, 2011) for decades, theoretically fulfil the needs of appropriate wavelengths and have already been deployed in particle concentration measurements (Ghosh et al., 2010). However, it is worth noting that experiments related to the latter publication have been conducted under non-ambient conditions, i.e. lower pressures ($<$200 Pa) and higher concentrations ($10^{11}\,\mathrm{cm}^{-3}$) . Due to large scattering background arising from carrier gas molecules, SAXS measurements on aerosol particles under ambient conditions do not yield reasonable signal to noise ratios, out of which convenient size distributions could be computed. By using helium instead of air more promising outcomes are achieved when utilizing the SAXS-technique, however, other theoretical and experimental challenges have to be taken into account.

Challenges of experimental character occur when adapting instruments, which commonly are used for measurements on nanoparticles carried in air, to the operation when particle-laden helium is under observation. Theoretical issues are caused by the different physical properties of helium compared to air, e.g. viscosity or mean free path. Part I of this work scrutinizes the mentioned problems and aims for the correct evaluation of the number size distribution of helium-carried particles.

2. Fundamental Background Information and Motivation

2.1 Aerosols - an Overview

An aerosol is a two-component system, which consists of a gas, wherein solid or liquid particles are suspended. Particles are found in different size ranges starting at single-digit nm and ending at several µm, therefore spanning ∼5 orders of magnitude. However, aerosol particles are classified by numerous other parameters, which are discussed in more detail later on in this section. An exemplary list of numerous frequently used categories is given below:

- particle number concentrations in units of cm^{-3} and mass density in $\mu g\, m^{-3}$ (Kannosto et al., 2008)
- size dependent concentrations, typically denoted as $dN/d\ln D_p$ (Kleinman et al., 2012)
- molecular aerosol particle composition (Hoffmann et al., 1998)
- primary/secondary and biogenic/anthropogenic character of aerosol particles and classification in terms of origin (Sun et al., 2016)
- direct/indirect contribution to radiative forcing (Charlson and Schwartz, 1992)

The first two categories typically are considered when analysis regarding air pollution is carried out. For instance, Wang et al. (2014) found the number concentration to increase for all particle sizes, if (photochemical) haze was present in Shanghai. Especially particles in the size range of 100nm have higher chances of deposition in the human lung, thus causing various health issues (Jaques and Kim, 2000). The third and fourth point have been studied for decades and their variations play a significant role in the radiation budget of the earth and affect the formation of cloud condensation nuclei (Cruz and Pandis, 1997) (Novakov and Penner, 1992). Therefore, aerosol particles contribute to both, direct (Charlson and Schwartz, 1992) and indirect (Jones et al., 1994) radiative forcing.
As indicated in the previous section, studies on the nucleation of aerosol particles by means of trace condensable vapours of both, biogenic and anthropogenic sources may play a significant role in climate. The study of fundamental nucleation mechanisms thus constitutes an active field of research which is oftentimes carried out in various laboratory and chamber environments. One of the world-leading chamber experiments in this respect is currently conducted at the

CLOUD (Cosmics Leaving OUtdoor Droplets) facility located at the proton synchrotron CERN, Switzerland. There, nucleation and NPF can be investigated under best controlled and cleanest conditions ever. A unique feature of this experiment is the possibility to study effects of galactic cosmic rays on NPF (Kirkby, 2011). A detailed explanation is given in the following section.

2.2 Overview of the CLOUD-project

The CLOUD-project involves 17 research groups from 9 different countries[1] and targets the analysis of various significant and climate-relevant processes, which contribute to new particle- and cloud formation. In the following a short summary on the participating reactions is outlined.
Earlier studies on atmospheric nucleation processes already emphasized the key role of sulphuric acid, (SA), which emerges from the oxidation of sulphur dioxide (Sihto et al., 2006). Despite of that, binary reactions of SA with water are no sufficient explanation for further particle growth, but other contributors, e.g. ammonia or organic compounds, must be considered (Wang et al., 2010). Initial CLOUD-experiments thus focused on these interactive effects and found that SA-particle nucleation intensively depends on standard ambient ammonia mixing ratios (Kirkby, 2011). Furthermore, it was shown that galactic cosmic rays (GCR) lead to somewhat enhancing impacts on NPF-events as well.
Succeeding studies included, among others, effects of amines on early particle growth, since contributing effects to nucleation processes were expected (Facchini et al., 2008). It was consequently investigated, that dimethylamine preserve freshly formed SA-clusters from evaporation by base-stabilization mechanisms (Almeida et al., 2013). Further on, oxidized organic compounds were found to play an important role in nucleation processes with water and SA from the beginning. For instance, Riccobono et al. (2014) showed that oxidation products of pinanediol participate in both, production of clusters of lower evaporation rates as well as enhanced subsequent growth. Consideration of these contributors even allows reproduction of corresponding nucleation rates in the lower atmosphere.
Dunne et al. (2016) again outlined the significant impact of amines as well as organic compounds on NPF and highlights, that most of all nucleation events in the troposphere are of ternary character. It was also found that solely organic vapours alone might initiate NPF as well, and their contributors to early particle growth are of extremely low volatilities (Tröstl et al., 2016). Consequently, global aerosol models also allow insight on particle formation caused effects to radiative forcing (Gordon et al., 2016).

The centre-piece of all experiments is the CLOUD-chamber. Therein prevailing physical properties regarding both, gas and particle phase, are permanently monitored and/or controlled. An exemplary list of obtained parameters as well as the scheme of the CLOUD-chamber (figure 2.1) are given as follows:

[1] Source: `http://cloud.web.cern.ch/content/institutions`

- temperature, pressure and relative humidity
- size-dependent aerosol particle concentrations, nucleation- and growth rates
- wide mass-to-charge ratio analysis of ion properties
- sulphuric acid concentration
- wide-range volatile organic compounds concentrations
- NO_x, O_3 and SO_2 concentrations

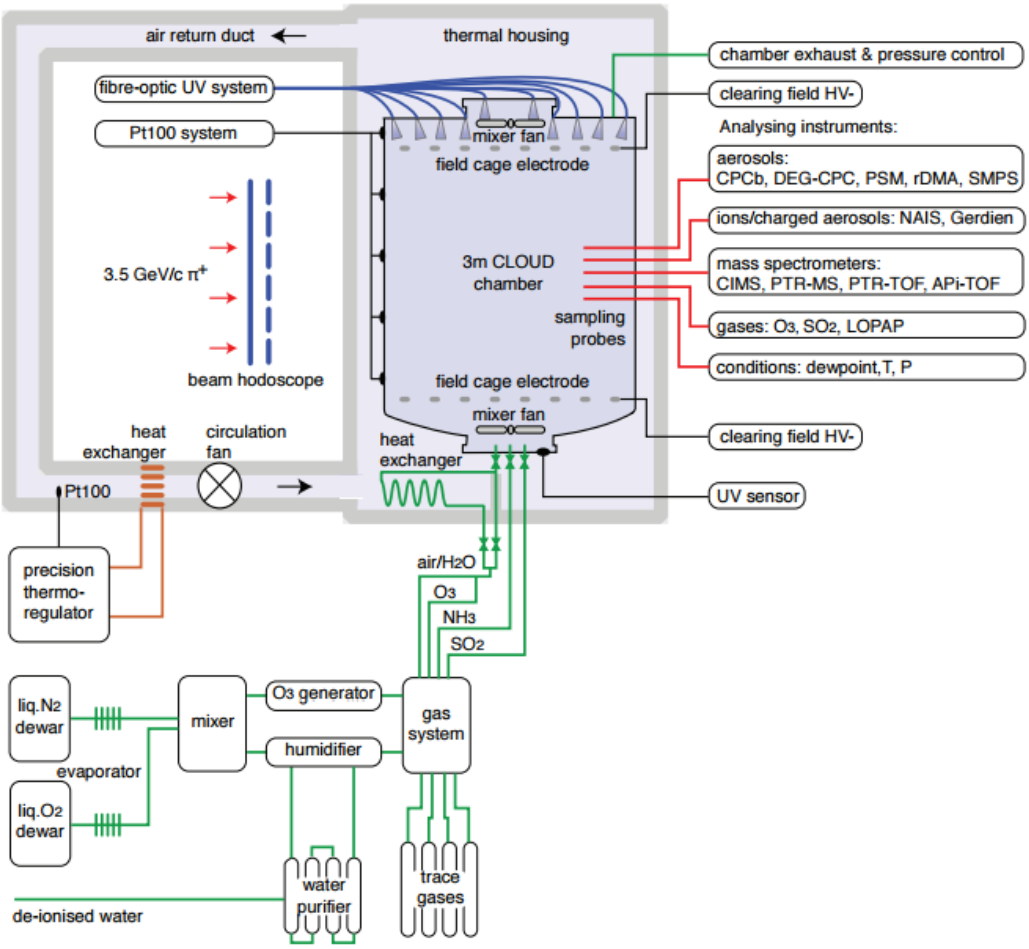

Figure 2.1: Schematic setup of the CLOUD-chamber (blue). Permanently sampling measurement instruments (red) necessitate controllable (trace-)gas input (green). Applied 'cosmic rays' provided by the Proton Synchrotron (PS) are detected by beam hodoscopes.

Since sampling instruments continuously draw air out of the chamber the gas system compensates for this air efflux and provides controllable concentrations of N_2, O_2, O_3, SO_2, O_3 and diverse organic compounds, such as α-pinene, β-caryophyllene or naphthalene. Higher ion concentrations, corresponding to those in the upper troposphere, are simulated by a π-particle beam, which is generated by the proton synchrotron (PS), and its energy detected by a beam hodoscope. An applicable high-voltage clearing field removes all charged particles, thus enabling analysis of effects contributed by neutral particles only, but also allows the removal of larger particles for new, subsequent measurement runs. Furthermore, sunlight simulating UV-systems are installed, and their wavelength dependent intensity considered as well (Kupc et al., 2011).

Reconsideration of the above-mentioned contributors to processes concerning nucleation and particle growth in the cloud chamber causes interest in highly time resolved analysis of low nm-sized particle concentrations. Two instruments, i.e. the nano-SMPS and the DMA-train (Stolzenburg et al., 2017), fulfil these requirements in different size ranges. However, non-negligible discrepancies in terms of particle concentration between the overlapping detection limits gives rise to questions regarding the correctness of obtained data. It is thus of great interest to find the reason for this mismatch and therefore initial experiments, as well closer insight into the working principles of both instruments are given in chapter 8.

2.3 Charging Mechanisms

Information on the aerosol particle's state of charge is absolutely necessary if investigation on their mobility equivalent diameters is conducted by means of differential mobility analysis (see section 3.1). Although the formation of particles itself leads to a certain charged fraction no reproducible or satisfying experimental results are thus achievable, since for subsequent data evaluation the corresponding charging probabilities must always be known. In the ideal (and simplest) case these size-dependent values do not change throughout the whole experiment.
Charging of aerosol particles may proceed via different processes, some of the most important ones are given in the list below. The two last-mentioned methods are explained in detail further on, since these processes are present in consecutively utilized charging devices:

- Flame charging (Burtscher, 1992)
- Spray electrification (Vaaraslahti et al., 2002)
- Corona discharge (Chang et al., 1991)
- Field charging and
- Diffusion charging.

Field charging mechanisms happen by means of an existing electric field. As a consequence of distorted field lines, which are caused by the neutral fraction, accelerated ions collide with these uncharged particles and subsequently transfer their charge. The induced field line distortions depend on both, the particle's material and their initial state of charge. The latter point has the consequence, that already charged particles are less likely to obtain an additional one (Hinds, 1999, p.325).
In contrast to field charging mechanisms diffusion charging processes are not caused by an electric field, but happen due to random collisions between unipolar ions and particles, and are observable in the earth's atmosphere. Consequently, parts of the previously neutral fraction are charged and vice versa. Since this process is dependent on Brownian motion of the ions, it correlates with their velocity, which in turn follows the Boltzmann distribution. It is thus less likely for the already charged fraction to acquire an additional charge, since the needed ion has to move with a higher velocity. Otherwise it is unable to overcome the existing particle's repulsive effect. However, since the Boltzmann distribution has no upper velocity limit, the charging rate never reaches zero (Hinds, 1999, p. 364).
Neutralization processes are occurring if ions of both polarities are present (bipolar diffusion charging). Originating equilibrium charge states are called Boltzmann, or steady-state, equilibrium charge distributions.
However, according to Fuchs (1963), kinetic methods are inevitable if correct computations on steady-state probabilities of particles smaller than 100 nm are desired. Furthermore the Boltzmann equilibrium charge distribution does not comply at all with experimentally obtained charging probabilities for lower size ranges (Kallinger and Szymanski, 2015) (Reischl et al., 1996). Fuchs' charging theory bases on the quantification of interactions between particles and ions by means of

a steady state ion flow towards limiting spheres. Each of these spheres encompasses one aerosol particle, and ions are solely attracted/repelled when entering this boundary. A complete overview of Fuchs' charging theory is given in Reischl et al. (1996) and Fuchs (1963).

Even though only mass and electrical mobility of the charge-providing ions must be known if concrete calculations are required, computations of Fuchs' charging theory are labour-intensive. Simplification is achieved using the approximated function and included parameters given in (Wiedensohler, 1988). Utilization provides continuous information on the probabilities caused by bipolar diffusion charging in the size range of 1 nm to 1 µm for neutral or singly charged particles (i=±1, i=0) and from 20 nm to 1 µm for the doubly charged fractions (i=±2). Conduction of the corresponding calculations, and implementing two corrected coefficients as given in Flagan (2008), result in figure 2.2. Considering the black line, it is evident that aerosol particles <100 nm most likely do not obtain a charge at all. Moreover the probability for negatively charged particles (blue) always exceeds the one for the positively charged fraction (red).

As mentioned above, comprehensive knowledge on the charged particle fractions is inevitable for analysis by means of an external electric field. Since charge transfer mechanisms heavily depend on properties of the carrier gas all given functions in figure 2.2 only hold true for airborne particles and are thus deviating if other gases are present. Charged fractions of different size consequently have impact on further computations of number concentrations. As a consequence measurements on charging probabilities of helium-carried particles represent a main theme of this thesis and are explained in great detail in chapter 3.5.

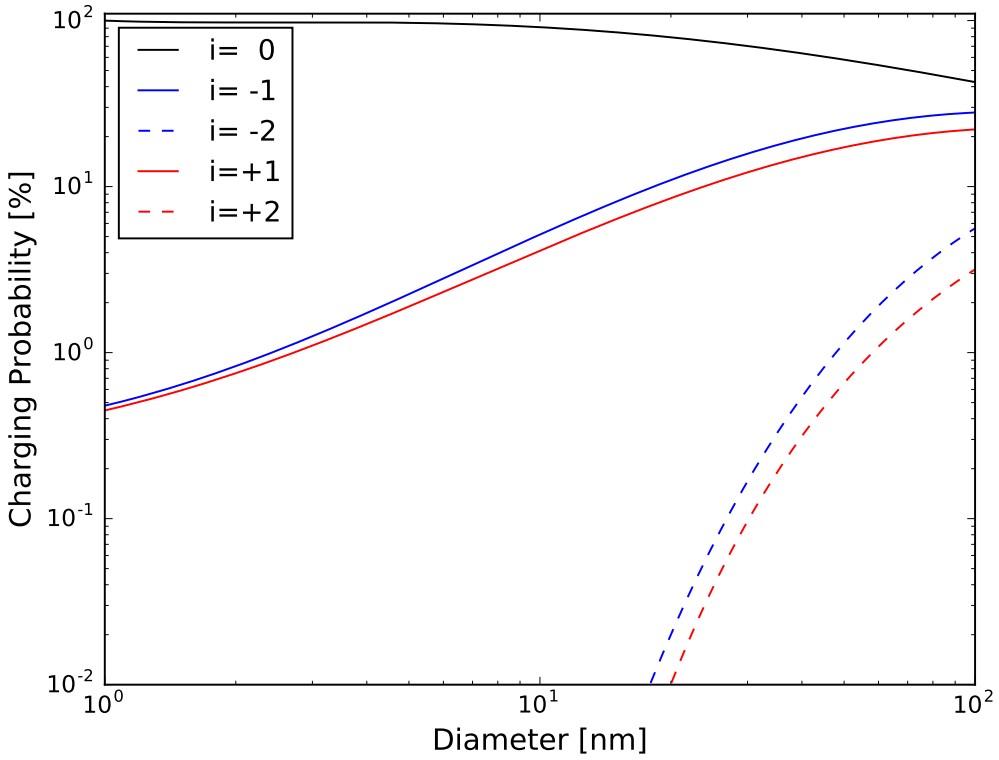

Figure 2.2: Calculated charging probabilities according to Wiedensohler (1988) and corrected coefficients as stated in Flagan (2008). The black line indicates the neutral fraction (i=0), the blue and red curves denote negatively (i<0) and positively (i>0) charged particles, respectively. Solid and dashed lines state, whether the considered particles are singly (i=±1) or doubly charged (i=±2).

3. Experimental Methods

A multitude of instruments targeting the generation and subsequent analysis of aerosol nanoparticles is used throughout this study. Knowledge of their physical bases as well as their working techniques are thus of great interest, especially if other carrier gases than air are involved. Differences in gaseous compounds not only give rise to inevitable experimental adaptions, but additionally have impact on the numerous conversion of the full size distribution out of raw data. Typical experimental setups include the

- Vienna type DMA, which allows the classification of aerosol particles by means of their electrical mobility,
- CPC and FCE, which permit continuous information on number concentrations,
- X-ray charger and ^{241}Am alpha-ray ionizer, both yielding particles in equilibrium charge distributions,
- aerosol particle generators, i.e. WO_x-generator, hot-wire generator, nebulizer and electrospray
- and the ion trap, i.e. a filter for charged particles up to one specific electrical mobility.

Parts of these instruments, i.e. the X-ray charger, DMA and CPC are used in the nano-SMPS and DMA-train. Both of these particle sizers allow high-time resolution concentration measurements of aerosol particles in different size ranges (see section 8).

3.1 Differential Mobility Analysis

The differential mobility analysis is a powerful method to study the size distribution of airborne particles. It can be used to retrieve size information over 3 orders of magnitude: studies below 10nm (Stolzenburg et al., 2017) exist as well as investigations of up to 1 µm (Kulmala et al., 2012). Over all this range the resolution as well as the principle of measurement do not change, however, size dependent particle losses (Kousaka et al., 1986) and charging efficiency have to be taken into account and are discussed in detail later on.
The concept of the differential mobility analysis is the classification of aerosol particles according to their electrical mobility Z, which is indirectly related to their mobility equivalent diameter D_p. This connection, as well as more information on the mentioned electrical mobility, is given

in section 3.1.2. The above-mentioned classification is achieved by utilizing a differential mobility analyzer (DMA) (E. O. Knutson, 1975). Its apparatus corresponds to a capacitor, i.e. two electrodes of different electrical potential generate an electric field. Various types are in use, e.g. parallel plate DMAs (J.P. Santos et al., 2009), radial DMAs (Brunelli et al., 2009), or cylindrical DMAs as described by Winklmayr et al. (1991), who proposed the so-called Vienna type DMA. Throughout this study the latter type is used and its structure, working principle and theoretic background are thoroughly discussed in the following subsections.

3.1.1 Structural set-up of the Vienna type DMA

The schematic structure of a Vienna type DMA is given in figure 3.1, in which two different types of parameters are comprised, namely those of geometrical kind as well as the operating conditions, i.e. the volume flows:

- geometrical parameters

  R_1: inner radius of the outside electrode

  R_2: outer radius of the inner electrode

  L: axial distance between aerosol-inlet and -outlet

- flow conditions

  Q_{sh}: clean and dry sheath air flow

  Q_a: aerosol particle-laden air flow

  Q_s: sampled/classified aerosol particle-containing air flow

  Q_{ex}: excessing particle-laden air flow

The flow Q_a, which contains the particles of interest, is overlaid with clean and dry sheath air Q_{sh}, providing a laminar gas flow moving in axial direction inside the DMA. Herein the charged aerosol particles move in radial direction towards the inner electrode caused by the present electric field, whose intensity changes depending on both, the voltage V applied to the mentioned electrodes and the momentary distance r to the passing object. This correlation is evident in equation (3.1), which quantifies an electric field inside a cylindrically shaped capacitor.

$$E(r) = \frac{Q}{2\pi \cdot r \cdot L \cdot \epsilon_0 \epsilon_r} \tag{3.1}$$

Q is the object's electrical charge, ϵ_0 the vacuum permittivity, ϵ_r the relative permittivity and $E(r)$ the corresponding electric field intensity. Furthermore, considering standard conditions for pressure and constant temperature, the two flows entering the system must be equal to those exiting it, see equation (3.2).

$$Q_a + Q_{sh} = Q_s + Q_{ex} \tag{3.2}$$

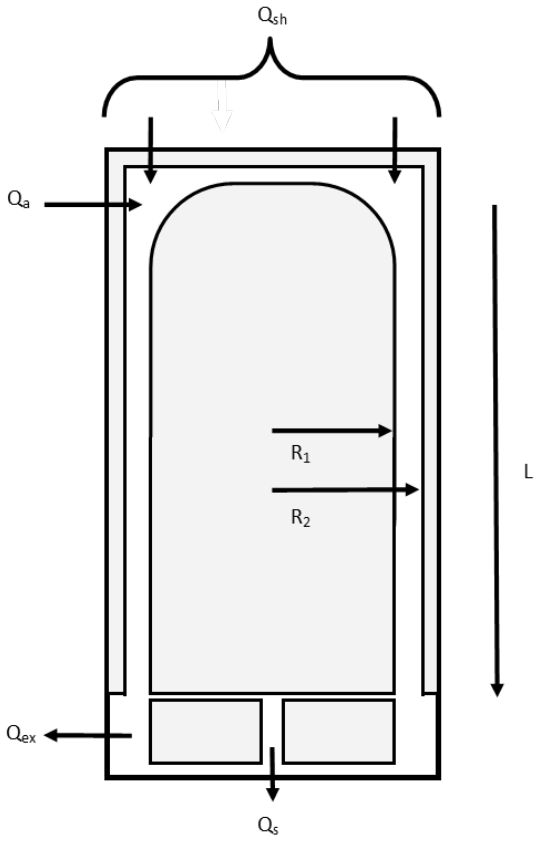

Figure 3.1: Schematic of a coaxial-cylinder Vienna type DMA. The radii R_1 and R_2 are the outer radius of the inner electrode and the inner radius of the outer electrode, respectively. L denotes the separation-length. Q_a and Q_{sh} denote the ingoing aerosol- and sheath-flow, Q_s and Q_{ex} the outgoing sample- and excess-flow.

3.1.2 Functional Relation between Voltage, Diameter and Flow Rates

Theoretical derivation of the functional relation between the voltage V, which is applied on the DMA, and thus selected aerosol particles with diameters D_p necessitates the consideration of two acting forces: electric field intensity and drag from the carrier gas.
As mentioned before, D_p corresponds to the particles' electrical mobility Z, which is why it is formally called electrical mobility equivalent diameter. Considering an ion, which propagates through an electric field (with a given intensity E), the electrical mobility determines its final drift velocity v_d according to equation (3.3).

$$v_d = Z \cdot E \tag{3.3}$$

Electrical mobility Z is determined by (3.4) wherein i equals the number of elementary charges on the particle and B is mechanical mobility. As can be seen Z is directly proportional to both quantities. Based on this relation Millikan experimentally found, that all states of charge are multiples of the elementary charge e_0 (Millikan, 1913).

$$Z = i \cdot e_0 \cdot B \tag{3.4}$$

It is obvious that the ion's field-caused acceleration not only depends on its state of charge, but also on its mechanical mobility B, see equation (3.5), whose determining factors are discussed further on.

$$B = \frac{v_d}{F_S} \tag{3.5}$$

When a particle with known diameter D_p penetrates through the DMA, constant drag acts on it. The corresponding force F_S is quantified by Stokes' equation (3.6), which assumes spherical particles. The comprised η denotes the carrier gas' viscosity, and v the particle's velocity.

$$F_S = \frac{3\pi \cdot D_p \cdot v_d \cdot \eta}{C(D_p)} \tag{3.6}$$

The Cunningham slip-correction factor $C(D_p)$, see equation (3.7), corrects for the drag on particles caused by potential non-continuum gas behaviour (Cunningham, 1910). The corresponding constants are obtained from the studies of Allen and Raabe (1985).

$$C(D_p) = 1 + a_1 \cdot \frac{\lambda}{D_p} + a_2 \cdot \frac{\lambda}{D_p} \cdot exp\left(-a_3 \cdot \frac{D_p}{\lambda}\right) \tag{3.7}$$

$$a_0 = 2.284$$

$$a_1 = 1.116$$

$$a_2 = 0.4995$$

These values should be treated with caution since ambiguities in terms of their correctness exist. Presenting a theoretical approach describing the transport of aerosol particles in gases Li and Wang (2003) provide numerous experimental results for the above coefficients. $C(D_p)$ increases with decreasing D_p, therefore becoming essential for calculus concerning particles with diameters close to the mean free path of the carrier gas molecules. Hence, the correction factor additionally varies with the composition of the gaseous medium. This behaviour is clarified in picture 3.2, where the size- and gas-dependency of $C(D_p)$ is illustrated for air and helium. For larger particles ($\geq 10\,\mu m$) $C(D_p)$ equals 0, irrespective to the carrier gas composition.

Including equation (3.6), the mechanical mobility can now be written as follows:

$$B = \frac{v_d}{F_S} = \frac{C(D_p)}{3\pi \cdot D_p \cdot \eta} \tag{3.8}$$

Putting 3.4 and 3.8 together yields equation 3.9. If only one state of charge exists, e.g. when

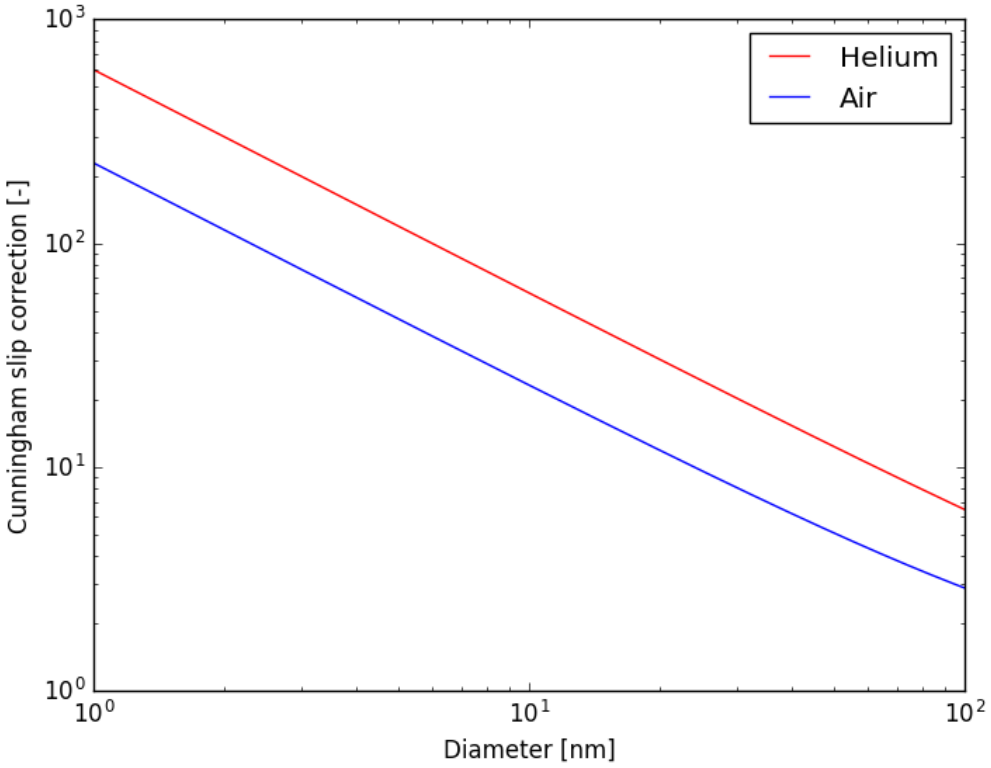

Figure 3.2: The Cunningham slip correction for particles between 1nm and 100nm for air (blue) and Helium (red) as carrier gases. Implemented values for the viscosities are taken from http://www.engineeringtoolbox.com/gases-absolute-dynamic-viscosity-d_1888.html

i=1 for all particles, only one corresponding value for Z exists. However, it should be kept in mind, that this situation may not be true as particles of one diameter are likely to carry different numbers of elementary charges.

$$Z = \frac{i \cdot e_0 \cdot C(D_p)}{3\pi \cdot \eta \cdot D_p} \tag{3.9}$$

Differential mobility analysis utilizes this equation and relates it with the penetrating volumetric flows. In order to achieve this relation the flow pattern inside the DMA is assumed to be cylindrically symmetrical. Based on this physical circumstance , equation 3.10, derived from Ohm's law, indicates, that the drift velocity v_d depends on the distance to the cylinder axis alone. Further extension results in equation 3.11, wherein the electric-field strength, which is present between the electrodes, is substituted.

$$v_d(r) = Z \cdot E \;\Rightarrow\; \frac{dr}{dt} = Z \cdot |E(r)| \tag{3.10}$$

$$\frac{dr}{dt} = Z \cdot \frac{V}{r \cdot ln\,(R_2/R_1)} \tag{3.11}$$

More detailed information concerning the working principle of the DMA can be obtained from figure 3.3. Herein the direction of flow is from left to right, as the arrows, which represent $v(r)$, suggest. The dashed red line indicates an exemplary trajectory of a selected particle.

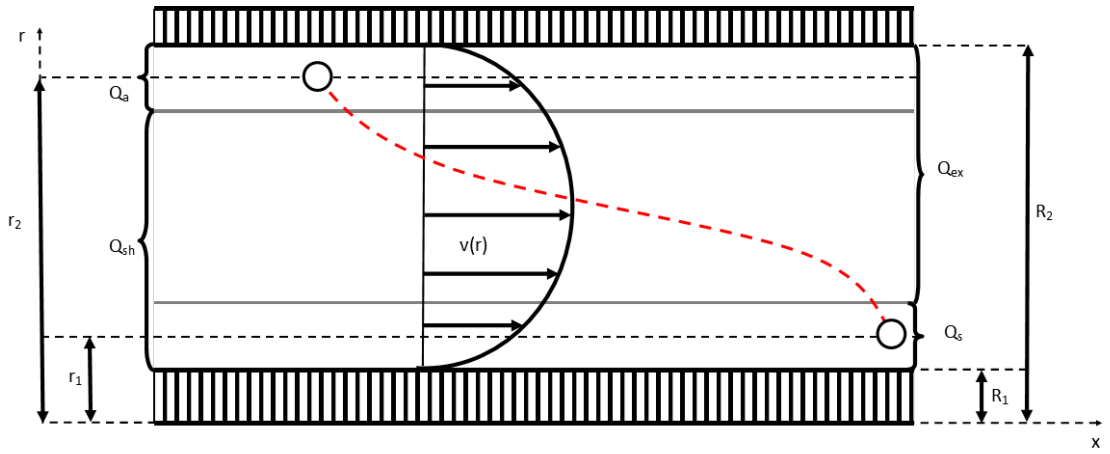

Figure 3.3: Detailed schematic of the cylinder-symmetrical flow, indicated by the right-pointing arrows, inside the DMA. $v(r)$ implies the drift velocity depending on the relative position to the electrodes. The dashed red line marks a possible trajectory of one classified particle, which is represented by white circles.

By multiplying the term $\frac{dx}{dt}$ with both sides of equation 3.11 yields

$$\frac{dx}{dr} = \frac{dx}{dt} \cdot \frac{dt}{dr} = \frac{ln(R_2/R_1)}{Z \cdot V} \cdot r \cdot v_d(r) \;\Rightarrow\; \int_{x_1}^{x_2} dx = \frac{ln(R_2/R_1)}{Z \cdot V} \cdot \int_{r_1}^{r_2} r \cdot v_d(r) \cdot dr \quad (3.12)$$

The arising differential equation is solved by separation of the variables x and r. If the coordinate origin is set to the lower left corner of figure 3.3 the first expression corresponds to the length of separation L. Multiplication with $\frac{2\pi}{2\pi}$ and adjusting leads to

$$Z = \frac{1}{V} \cdot \frac{ln(R_2/R_1)}{2\pi \cdot L} \cdot \int_{r_1}^{r_2} 2\pi r \cdot v_d(r) \cdot dr \quad (3.13)$$

By examination of this equation it is evident, that the expression $2\pi r$ results in a unit of area when integrated. Thus the complete integrand equals the volumetric flow present between the DMA's electrodes. The latter integral is solved by splitting it into three further integrals, see equation 3.14, which allows an easier solution method. Close scrutiny of image 3.3 shows, that if a particle possessing the mean electrical mobility Z^* is existing it may follow the red dashed line, starting at $Q_a/2$ and ending at $Q_s/2$. This assumption leads to

$$\int_{r_1}^{r_2} 2\pi r \cdot v_d(r) \cdot dr = \int_{R_1}^{R_2} 2\pi r \cdot v_d(r) \cdot dr - \int_{R_1}^{r_1} 2\pi r \cdot v_d(r) \cdot dr - \int_{r_2}^{R_2} 2\pi r \cdot v_d(r) \cdot dr. \quad (3.14)$$

Considering equation 3.2 the solution of equation 3.14 can be written as

$$Z^* = \frac{1}{V} \cdot \frac{ln(R_2/R_1)}{2\pi \cdot L} \cdot \frac{Q_{sh} + Q_{ex}}{2}. \quad (3.15)$$

As a consequence a functional relationship between the adjustable carrier flows and a resulting mean electrical mobility Z^* at any given voltage V is achieved. If compared with equation 3.9

this leads to

$$\frac{i \cdot e_0 \cdot C(D_p)}{3\pi \cdot \eta \cdot D_p} = \frac{1}{V} \cdot \frac{ln(R_2/R_1)}{2\pi \cdot L} \cdot \frac{Q_{sh} + Q_{ex}}{2}. \tag{3.16}$$

This equation allows the determination of the (only V-dependent) selected particle's electrical mobility equivalent diameter, if the DMA-characteristics, flow rates and carrier gas properties are known. However, it is worth noting that solving this problem requires iterative computation due to its transcendental character. Various studies aiming for simplification of the functional relation between Z and D_p in equation 3.9 are presented in Mäkelä et al. (1996), including the author's own convenient approximation given in equation 3.17.

$$Z = 2.2458 \cdot 10^{-22} \cdot D_p^{-1.9956} \tag{3.17}$$

Therein, diameters D_p and electrical mobilities Z have to entered in m and m^2/Vs, respectively. It is worth noting, that this approach is only valid for particles in the range 0.5 nm and 5 nm.

3.1.3 The Transfer function

The transfer function Ω (E. O. Knutson, 1975) is an important instrument function that describes the fraction of out- and ingoing concentrations of electrical mobility equivalent particles ($Z{=}Z^*$) moving through the DMA, wherein an electric field is present caused by an applied voltage V. This function can be written as

$$\Omega = \text{Min}\left(1, \frac{Q_s}{Q_a}\right). \tag{3.18}$$

It is obvious, that Ω cannot exceed 1, since this would be equivalent to the situation of more particles exiting than entering the DMA. Neglecting diffusional losses the presumption of the transfer function equalling 1 may hold true, however, it does not if further particles with small deviations ($Z{=}Z^* \pm \Delta Z$) regarding their electrical mobility enter the instrument.
Among other things, especially due to diffusional broadening, this is also caused by the non-infinitesimal character of inlet- and outlet-slit providing the aerosol flow Q_a and drawing the sample flow Q_s, respectively. This issue is illustrated in figure 3.4, where two particles of different electrical mobilities are shown. The red one barely is selected, penetrating from the top left corner down to bottom right exit slit, thus possessing the maximum Z equalling Z_{max}. However, the blue one almost is drawn from the outstreaming Q_{ex}, consequently having the smallest possible Z identical to Z_{min}. The indicated pathways drawn as dashed lines of corresponding colours solely serve the purpose of guiding the eye and clarifying the situation explained above, indeed the particles' actual trajectory is of no importance.

For further calculus the mentioned minimum/maximum electrical mobilities Z^* are transformed so that notations just in terms of flow rates are possible, leading to $Z^{*\prime}$. Considering equation

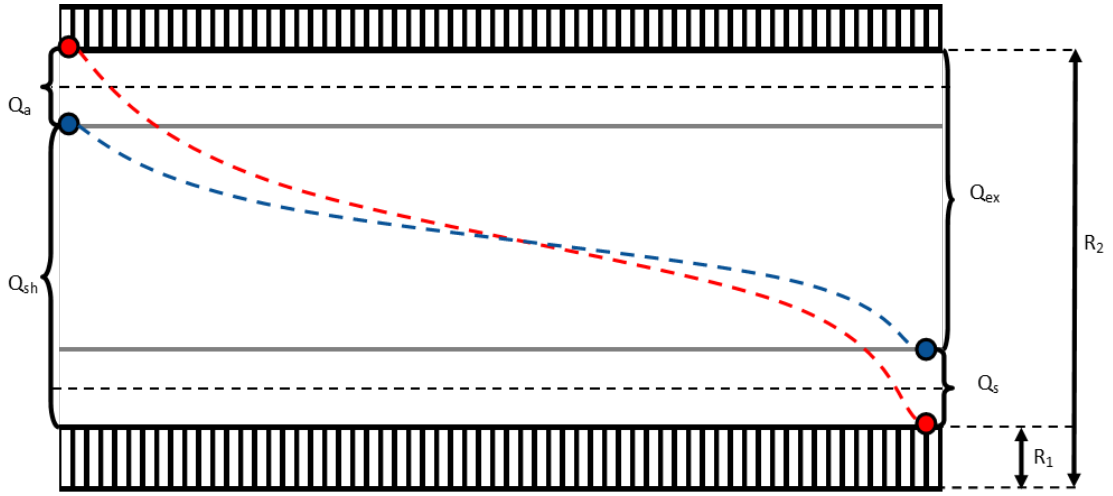

Figure 3.4: Schematic of selected particles possessing the maximum (red) and minimum electrical mobility in order to contribute to Q_s. The corresponding trajectories are merely of exemplary character.

3.9 yields

$$Z^{*\prime} = Z^* \cdot V \cdot \frac{2\pi \cdot L}{ln(R_2/R1)} \tag{3.19}$$

where the latter factor is constant and $Z^{*\prime}$ can be written as

$$Z^{*\prime} = \frac{Q_{sh} + Q_{ex}}{2}. \tag{3.20}$$

In order to achieve the flow rates Z'_{max} and Z'_{min} the expression $2\pi r \cdot v_d(r) \cdot dr$ is integrated once again, whereby the required boundaries are obtained observing figure 3.4: In respect to the 4 existing volumetric flows the initial particle positions define the lower limits, the endpoint determines the upper ones, respectively. This yields:

$$Z'_{max} = Q_{sh} + Q_a \qquad Z'_{min} = Q_{sh} - Q_s \tag{3.21}$$

Considering particles with mobilities $Z'_{\downarrow max}$ somewhat lower than Z'_{max} as well as $Z'_{\uparrow min}$ being slightly higher than Z'_{min} consequently leads to effective selection either way. However, as suggested in figure 3.5, the former particle's trajectory would end concisely above the transparent red one's, the latter closely below the transparent blue trajectory's final position. Each case results in an additional flow Q_x, which quantifies the outlined situation in the following way

$$\begin{aligned} Z'_{\downarrow max} < Z'_{max} \;\Rightarrow\; Z' = Q_{sh} + Q_a - Q_x = Z'_{max} - Q_x \\ Z'_{\uparrow min} > Z'_{min} \;\Rightarrow\; Z' = Q_{sh} + Q_a - Q_x = Z'_{max} - Q_x \end{aligned} \tag{3.22}$$

Recalling equation 3.18 the sample flow Q_s is now the divisor of Q_x in equations 3.22.

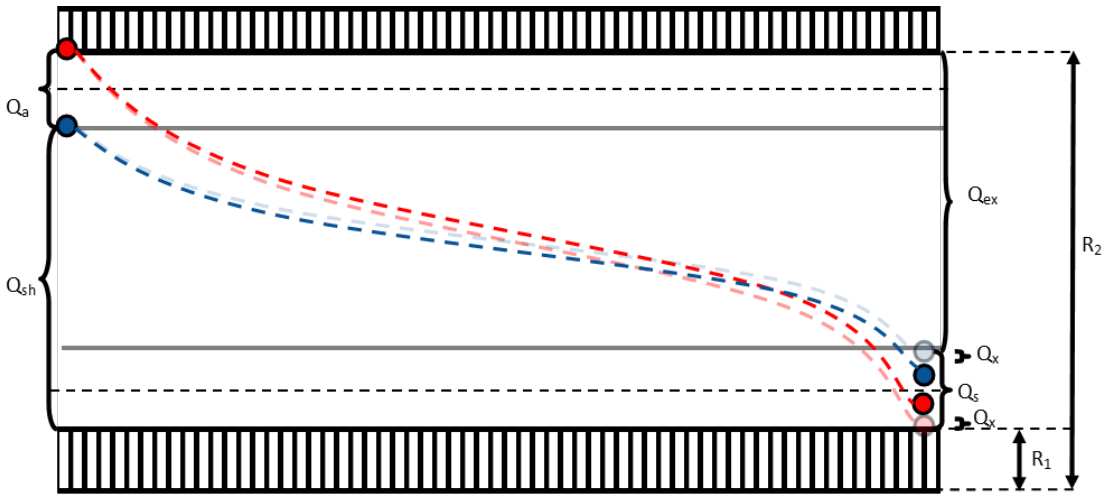

Figure 3.5: Schematic of selected particles with mobilities slightly lower than Z_{max} (red) and a bit higher than Z_{low} (blue). Each of these non-extreme cases raises another flow Q_x as implied at the bottom right corner.

As a conclusion the complete transfer function is given in equation 3.23.

$$\Omega = \text{Min}\left(1, \frac{Q_a}{Q_s}, \frac{(Q_{sh}+Q_a)-Z'}{Q_s}, \frac{Z'-(Q_{sh}-Q_s)}{Q_s}\right) \tag{3.23}$$

Approaching this situation with $Z' = 0$ and thenceforward constantly increasing, the fourth expression causes a rise of Ω as soon as Z' equals the subtrahend, thus exceeding 0 and becoming the overall minimum. After a linear increase a plateau is reached at

$$\begin{aligned} \Omega &= 1 \qquad \text{if} \quad Q_a > Q_s \quad \text{and} \\ \Omega &= Q_a/Q_s \quad \text{if} \quad Q_a < Q_s, \end{aligned} \tag{3.24}$$

what is evident if the first and second terms are examined. However, if starting with $Z' > Z'_{max}$ and subsequent decrease, the third expression must be taken into account. Similar to the case exemplified before an increase of Ω is observed when Z' decreases below the minuend, thus becoming the minimum again.

The above explanations, which initially may seem confusing, are also illustrated in figure 3.6. Therein, the entire possible constellations, namely

$$\begin{aligned} &\text{(a)} \quad Q_a > Q_s, \\ &\text{(b)} \quad Q_a = Q_s \text{ and} \\ &\text{(c)} \quad Q_a < Q_s \end{aligned} \tag{3.25}$$

are given.

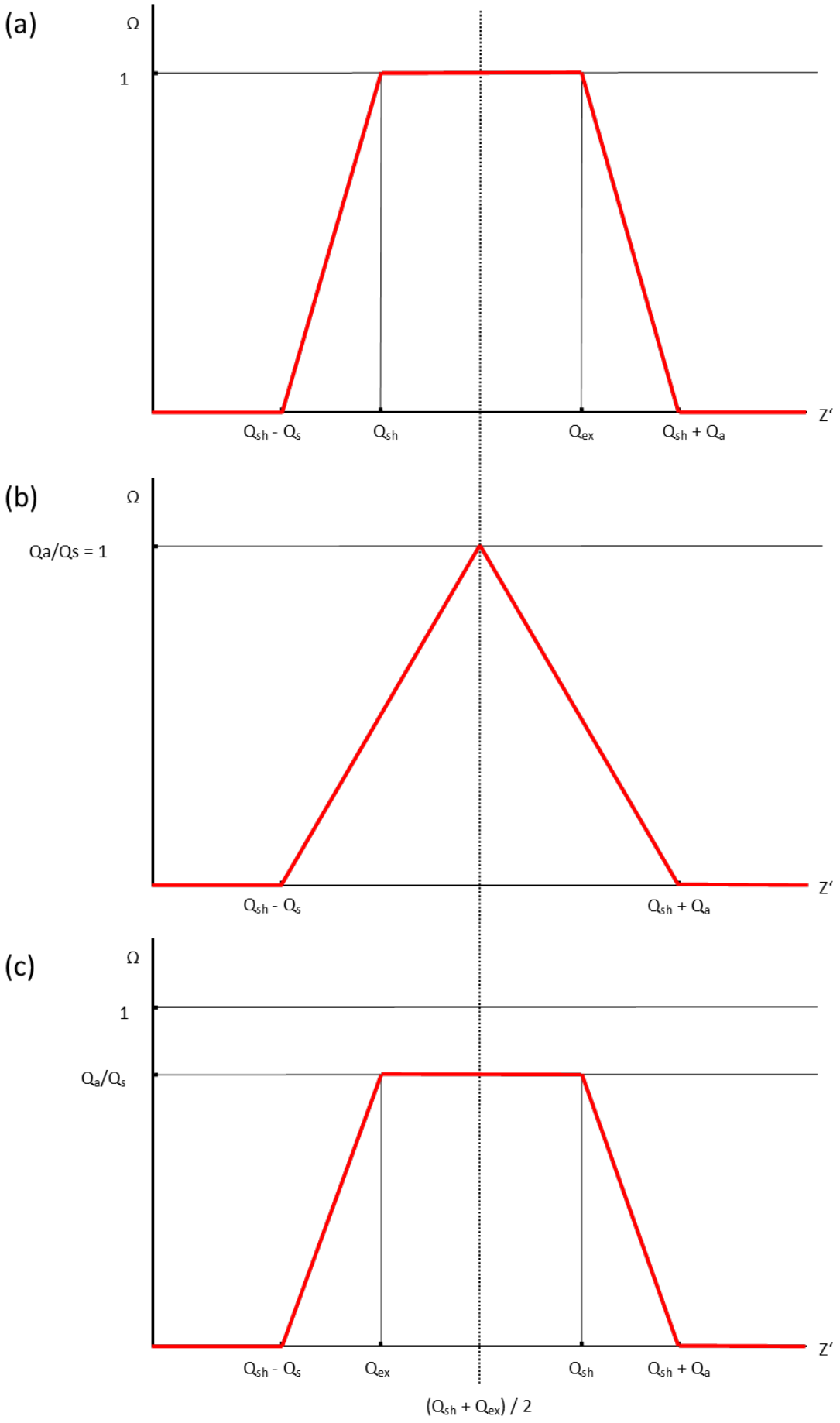

Figure 3.6: The transfer function Ω for (a) $Q_a > Q_s$, (b) $Q_a = Q_s$ and (c) $Q_a < Q_s$. Only in the favoured case (b) the function has no plateau, but just a global maximum.

3.1.4 The Resolution Power of the DMA

By means of the previous chapter pertaining to the transfer function the resolution power of a DMA is attainable. Taking figure 3.6 into account the lowest full width half maximum (FWHM) is displayed in the symmetrical case (b), where $Q_{sh} = Q_{ex}$ and $Q_a = Q_s$. Thereupon the resolution power equals to

$$\frac{dZ}{Z} = \frac{FWHM}{Z'} = \frac{Q_a}{Q_{sh}}. \tag{3.26}$$

In order to describe this quantity with D_p-dependency one can write

$$\frac{dD_p}{D_p} = \frac{d\ ln(D_p)}{d\ ln(Z)} = \Psi(D_p) \cdot \frac{Q_a}{Q_{sh}} \tag{3.27}$$

where $\Psi(D_p)$ arises when substituting 3.9 into the second expression of equation 3.27 and subsequent computation:

$$\Psi(D_p) = -\frac{C(D_p)}{(D_p)^2} \cdot \left(\frac{d\left(\frac{C(D_p)}{D_p}\right)}{dD_p} \right)^{-1} \tag{3.28}$$

Figure 3.7 exhibits both, the dependency of Ψ on D_p and on two different carrier gases, i.e. air and helium. It is remarkable, that Ψ converges to 0.5 if D_p is small. This trend causes the resolution power to increase by a factor of 2 if particles $\lesssim$10nm are analysed.

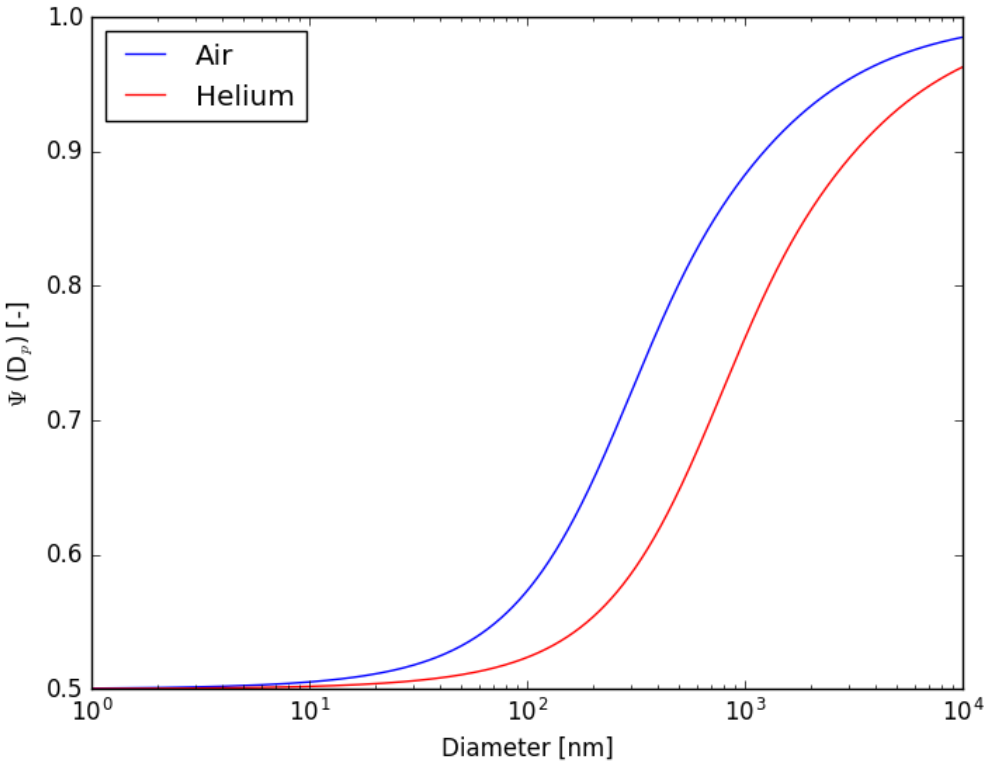

Figure 3.7: Ψ-function as a function of D_p and $C(D_p, \lambda)$ for air (blue) and He (red) computed with equation 3.7. For small particles a convergence towards 0.5 is clearly evident. For micrometer sized particles the function approaches 1. The different curve shapes are due to distinct η and λ, which results in a steeper slope of the graph valid for helium.

3.2 Generation of Nanoparticles

Throughout this work 4 different methods for generation of aerosol nanoparticles are used, depending on the desired size (or size range) and carrier gas:

- Tungsten-oxide - generator
- Hot-wire - generator
- Nebulizer
- Electrospray

The tungsten-oxide - generator (Grimm Nano Aerosol Generator Model #7.860) produces airborne nano particles by means of a tungsten coil. If heated, tungsten oxide sublimates into a low flow of carrier air (denoted 'WO_x air') and, through subsequent coagulation, yields particles in the size range of 1.25 nm and 10 nm (Steiner et al., 2006). Subsequently, the aerosol flow is mixed with filtered and dried particle free 'Carrier air'. The complete flow schematic is given in figure 3.8. If lower concentrations are required an optional dilution flow ('Diluting air') can be added.

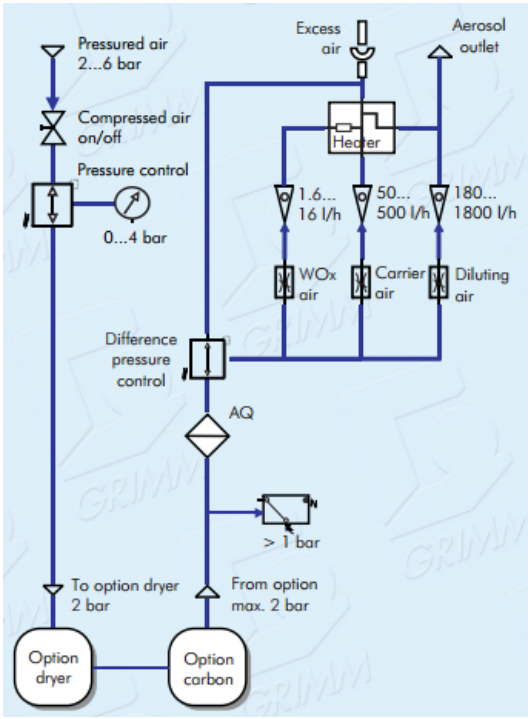

Figure 3.8: Flow schematic of the WO_x - generator. Tungsten oxide particles sublimate from a heated WO_x coil and grow by means of coagulation processes. Subsequently the produced particles are moved outside by the flow denoted as 'WO_x-Air'. Additional 'Carrier Air' ensures sufficient flow in order to transport all particles to the aerosol outlet. By means of another flow, i.e. 'Diluting Air', a decrease in concentration is attainable. (Grimm, 2005)

The hot-wire - generator is a non-commercial product which operates in a similar way as the tungsten-oxide - generator: By applying current to an arbitrary metal coil, corresponding particles sublimate. Again, through subsequent coagulation aerosol particles in the size range of 1 nm and 15 nm are produced. Its schematic can be seen in figure 3.9.

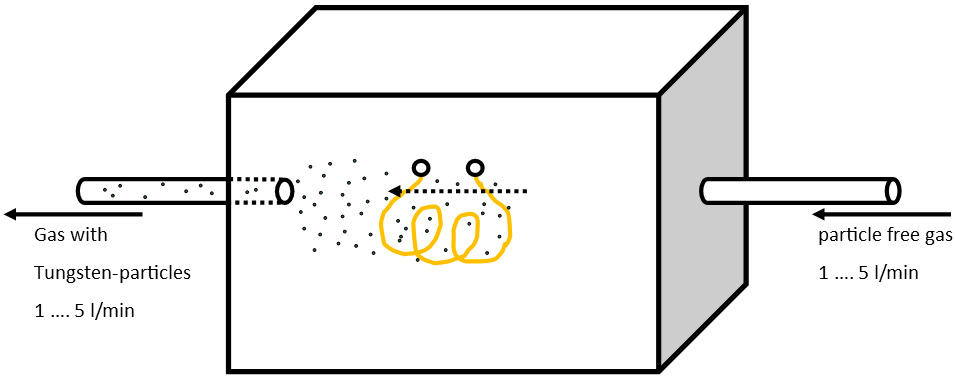

Figure 3.9: Schematic of the Hot-Wire - generator. Applied voltage and current on a wire causes sublimation, subsequent coagulation, and thus formation of aerosol nanoparticles. The resulting size distribution strongly depends on both, electrical settings and penetrating gas flow. The latter carries the produced particles out of the instrument, therefore providing an aerosol stream for further investigations.

Contrary to the previous generator it is necessary to adjust the flow rate before the filament chamber, wherein this gas stream carries the aerosol particles outside. Furthermore, rapid changes of applied current might lead to rupture of the coil and thus should be avoided. However, careful application and permanent cooling of the generator's housing yield constant particle output, no matter which carrier gas is used. This is a major advantage compared to the tungsten-oxide - generator which malfunctioned when operated with helium. This circumstance might be ascribed to the lack of oxidation, and thus the sharp decrease of sublimating particles.
The nebulizer allows the generation of sub-micron sized aerosol nanoparticles by atomizing droplets. The working principle is depicted in figure 3.10. Pressurized air between 1 and 3 bar leads to a liquid upflow from a reservoir caused by the Bernoulli's principle. The solution/suspension, in which the particles of interest are dissolved/suspended is nebulized by a fast air jet emanating from a small slit and arising from the applied pressure as well. Droplets of larger sizes fall back down and exit the nebulizer through the excess, either back into the primary reservoir or a separate one. Smaller aerosols leave the instrument via an opening at the opposite, yielding a constant output, e.g. the suspension of polystyrene latex (PSL) spheres in air. (Schmid et al., 2002).
The electrospray is a powerful tool if monodisperse aerosols smaller than 100nm are of interest (Hogan and Biswas, 2008) (Kallinger and Szymanski, 2015). Its theoretical basis was described by Taylor (1964). The working principle is as follows (see picture 3.11): A high voltage platinum wire as well as a capillary with a diameter of 25 µm dip into the sample solution/suspension if the pressure chamber bottom is plugged into the instrument. The wire charges the liquid, which subsequently is pushed through the capillary by means of an applied differential pressure. When reaching the capillary tip an electric field forces the liquid outside, forming a Taylor Cone (Taylor, 1964) if all parameters, i.e. pressure, voltage and CO_2/air flow, are adapted the right way: From the tip of the Taylor cone highly charged droplets are released towards the counter electrode and get airborne. Subsequently, the highly charged primary droplets are neutralized (see section 2.3) which is accomplished with a radioactive Po-210 - ionizer, and the remaining liquid vaporizes, leaving solely the aerosol particles excessing the chamber for further experimental research.

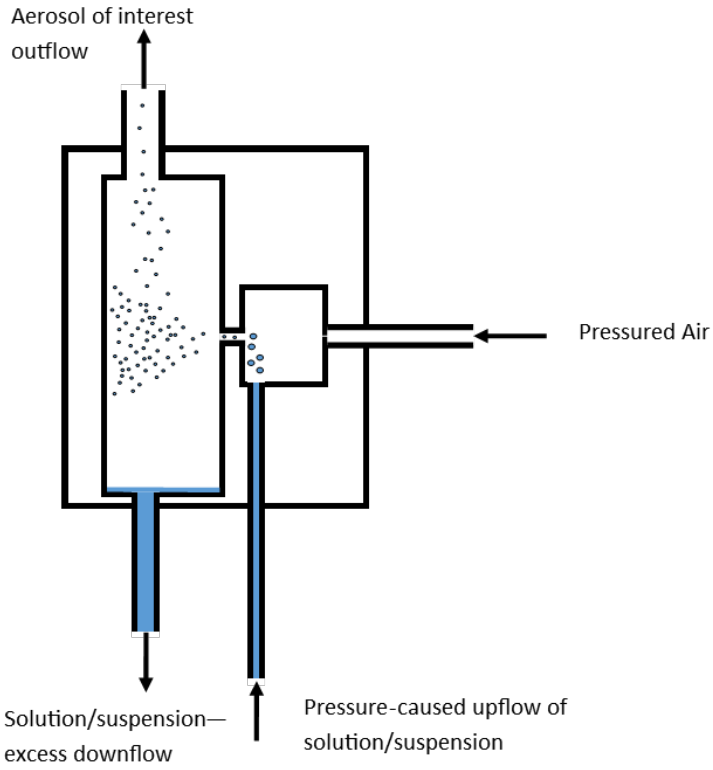

Figure 3.10: Schematic of the Nebulizer. Applied pressure yields both, an upflow of the particle containing liquid, and a fast air jet. The latter nebulizes the suspension/solution, producing aerosol particles, which subsequently move into another chamber. If small/light enough the atomized sub-micrometer sized products move to the outflow, therefore providing an aerosol flow.

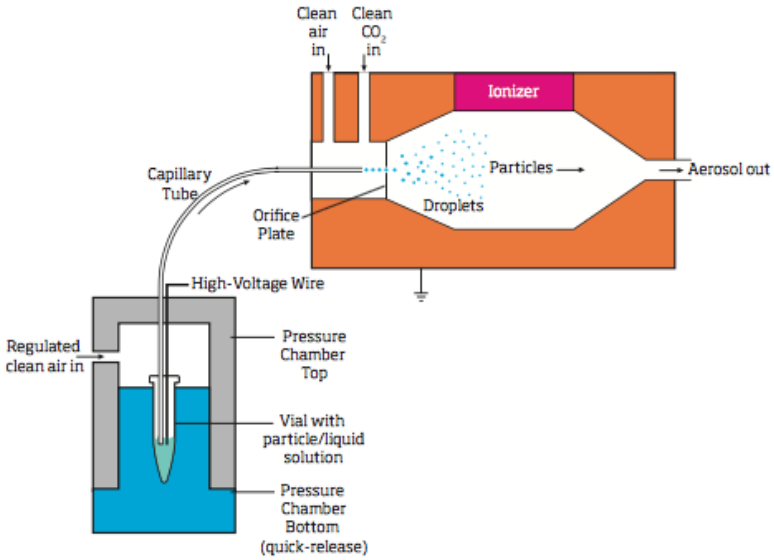

Figure 3.11: Schematic of the TSI Electrospray Generator 3480 obtained from its manual. The platinum wire charges the liquid sample. Subsequent transport through the capillary is achieved by applied differential pressure. An electric field causes a Taylor cone, resulting in outgoing primary droplets. Additional CO_2 eases the achievement of this voltage-, pressure-, and solution-dependent shape. The implemented Po-210 ensures a steady state charge equilibrium of the nanoparticles.

3.3 Detection of Aerosol Nanoparticles

3.3.1 Measurements with the Condensation Particle Counter (CPC)

If not explicitly mentioned all following investigations are performed using an ultrafine CPC (UCPC, TSI 3776) with butanol as working fluid. Necessary characterisations (Hermann et al., 2007) and countless practical laboratory and field measurements (Kulmala et al., 2012) have already been performed with this well-established instrument.
Figure 3.12 shows the flow schematic of the CPC. At the sample inlet a specific sample flow of 0.3 l/min (low flow mode) or 1.5 l/min (high flow mode) is drawn. Irrespective which mode is used the flow is split up into an aerosol flow (0.05 l/min), a sheath flow (0.025 l/min) and, if the high flow mode is on, an additional bypass flow (1.2 l/min). The critical orifice at the top of the schematic sets the 0.3 l/min, the necessary subdivision happens by adjusting the variable orifice at the bottom left part. The latter flow depends on the setting of the variable orifice in the top left corner.

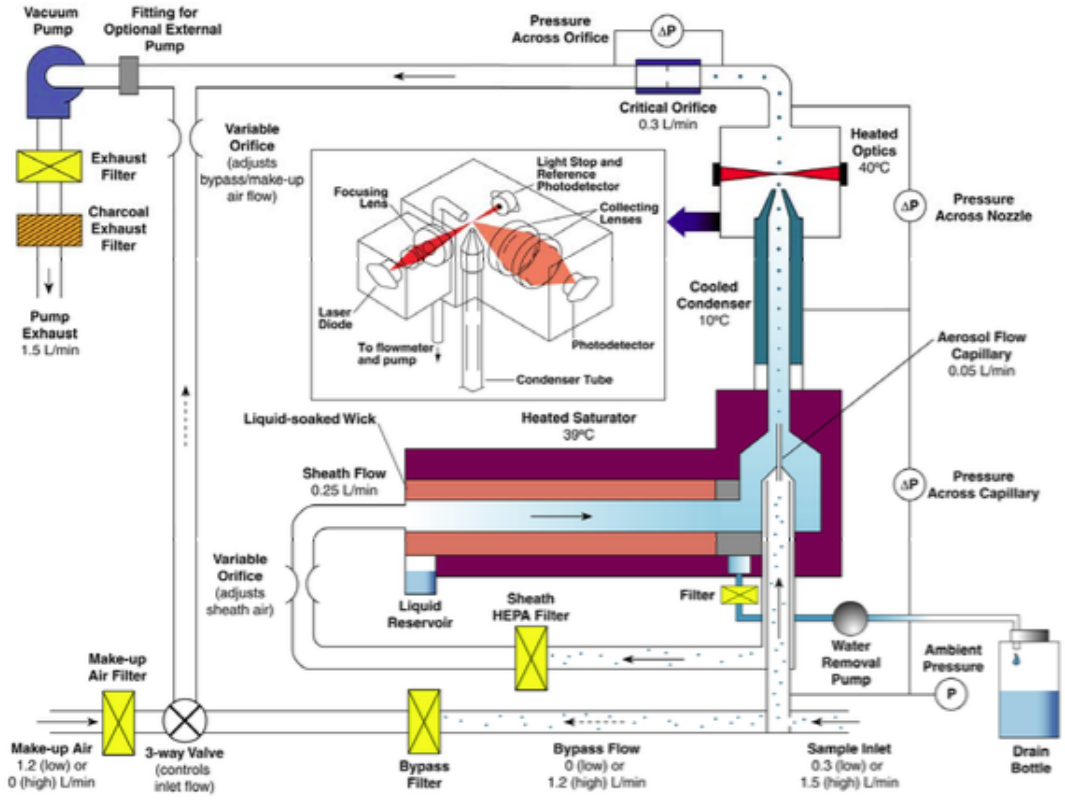

Figure 3.12: Flow schematic of the CPC (TSI, 2006). Either 0.3 l/min or 1.5 l/min are drawn at the sample inlet. Subsequent branching yields 0 l/min or 1.2 l/min bypass flow, respectively, thereby always maintaining 0.3 l/min through the measurement zone. The latter is split up into sheath flow (0.25 l/min) and aerosol flow (0.05 l/min). The former is saturated with working fluid, heated, and subsequently reunified with the other one, resulting in a laminar flow. An abrupt temperature drop along the tube causes super saturation followed by heterogeneous nucleation and condensation of butanol vapor on the sample particles. Consequent droplet growth to sizes around 10 µm allows detection and particle counting by optical means.

Since the counting happens by optical means, the investigated aerosol nanoparticles have to be enlarged first. This is achieved by heating and saturating the sheath flow in the saturator and remixing it with the aerosol flow in the condenser, where the butanol vapor condenses onto the particles of interest due to the present supersaturation.
It is worth noting that for measuring accurate number concentrations with the CPC correct flow adjustments, and thus pressures, must be guaranteed. Equally important are the temperatures of saturator and condenser. The investigated particles need to be activated, but homogeneous nucleation of the vapour itself must not be present under all circumstances, since previous non-existent particles contribute to the scattered light signal otherwise.

3.3.2 Measurements with the Faraday Cup Electrometer (FCE)

Determination of number concentrations in an FCE happens by measurement of an electric current, which is directly proportional to the charges carried by the particles. This happens by collecting the particles of interest on a filter inside a Faraday cage. Contrary to CPCs, number concentrations are measured in terms of current produced by the charged particles which relates to number concentration via

$$N = \frac{I}{Q \cdot e_0 \cdot i} \tag{3.29}$$

where N is the particle concentration, I the measured current, Q the volumetric flowrate, e_0 the elementary charge and i the charges on the particles. However, it is worth mentioning that this method requires that every particle carries solely one charge. Especially considering particles larger than $\sim$50 nm this assumption is not any more valid since the steady state charging probability for carrying two negative elementary charges from this size on increases above 1%, and is hence not negligible anymore. As a consequence, this phenomenon leads to the necessity of data inversion, see section 3.4

3.4 Retrieval of the Number Size Distribution

Number size distribution $\frac{dN}{d\ ln(D_p)}$ is typically measured by a DMA in combination with an appropriate particle detector (CPC or FCE). The measured raw data N_0 at a given size obtained by the detector needs to be corrected for several effects such as charging efficiency, diffusional losses/transfer function and detection efficiency. Retrieving the number size distribution thus requires proper data inversion.
The basic setup which allows such measurements is illustrated in figure 3.13. The sample flow, e.g. provided by a generator (see section 3.2) or just ambient air, initially is penetrating through a charger (see section 2.3). Subsequently, the aerosol particles move through an analyzing DMA (see section 3.1) where they are characterized according to their electrical mobility. The resulting sample flow is drawn by a particle counter.

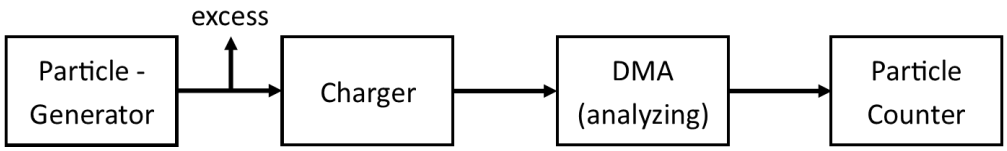

Figure 3.13: Basic experimental setup for measurements of the generated particles' size distribution. Charging (Charger), electrical mobility based classification (DMA) and subsequent counting (FCE or CPC) yields the size-dependent number distribution of the aerosol particles.

3.4.1 Inversion Factors

Every instrument is thoroughly discussed, including its by-effects, e.g. applicability ranges or limits of operation. All of these have to be taken into account, as well as sources for potential particle loss, in order to compute the correct number size distribution:

- The charger yields a steady state **charging probability** $\boldsymbol{\alpha(D_p, i)}$. Considering this allows the calculation of the total concentration as the DMA-selected fraction is known. For instance, for singly charged particles of D_p=20nm the corresponding charging probability equals $\alpha = 11\%$. Hence, only $11/100$ of the originally present particles are detectable. As a consequence, multiplication of the measured concentration by the inverse leads to the original concentration.

- The **sheath flow** $\boldsymbol{Q_{sh}}$ **and aerosol flow** $\boldsymbol{Q_a}$ enter the DMA, the former overlaying the latter. Due to the subsequent mixing procedure the aerosol particles are diluted in the ratio of $\beta = Q_a/Q_{sh}$. Again, the measured raw data have to be multiplied by the inverse of this fraction.

- Since concentrations as a function of D_p are desired the a priori Z-dependence must be transformed. Consequently the $\boldsymbol{\Psi}$**-function** must be taken into account the same way as the quantities before.

- **Particle losses η_{diff}** caused by diffusion processes are inevitable (Okazaki and Willeke, 1987), especially if particles smaller than 100nm are analysed. It is evident that these diffusional losses depend on the length of the sampling line L, the volumetric flow rate Q and the diffusion coefficient D. Numerical calculus of η_{diff}, as given in Hinds (1999), is possible using equations (3.30) to (3.32). Therein μ is a dimensionless deposition parameter, L the length of the sample tube, $\bar{U}$ the average flow velocity penetrating through the tube, and D the diffusion coefficient. The latter can be computed using equation (3.33), which is the Stokes-Einstein-equation weighted with the Cunningham slip correction $C(D_p)$

$$\mu = \frac{4 \cdot D \cdot L}{\pi \cdot D_p^2 \cdot \bar{U}} = \frac{D \cdot L}{Q} \tag{3.30}$$

$$\eta_{diff} = 1 - 5.5 \cdot \mu^{2/3} + 3.77\mu \qquad \text{for} \quad \mu < 0.009 \tag{3.31}$$

$$\eta_{diff} = 9.819 \cdot exp\,(-11.5 \cdot \mu) + 0.0975 \cdot exp\,(-70.1 \cdot \mu) \qquad \text{for} \quad \mu \geq 0.009 \tag{3.32}$$

$$D = \frac{kT \cdot C(D_p)}{3\pi \cdot \eta \cdot D_p} \tag{3.33}$$

  Examination of equations (3.30) to (3.32) shows an increase of η_{diff} as D_p decreases and D increases. The latter causes a lower η_{diff} if carrier gases, e.g. helium, with higher mean free paths λ, and thus exceeding $C(D_p)$ for all particle sizes, are present.
  Again, the crude data must be multiplied by the inverse quantity of η_{diff}.

- When using a CPC as particle counting instrument its **activation efficiency η_{act}** must be considered as well. For instance, if the CPC has a cut-off diameter of $D_{p,50}$=2nm just 50% of particles at 2nm are detected. As a consequence the real concentration is equal to the product of the inverse activation efficiency and the data obtained with the CPC.

Figure 3.14 depicts all inverted quantities for particles between 1nm and 100nm. The inverse charging efficiency spans over 2, the inverse efficiencies η_{diff} and η_{act} over 1 order of magnitude, respectively. In contrary, the inverse parameters β and Ψ show scarce change in D_p. The charging efficiency $\alpha(D_p, i = -1)$ is taken from Wiedensohler (1988).

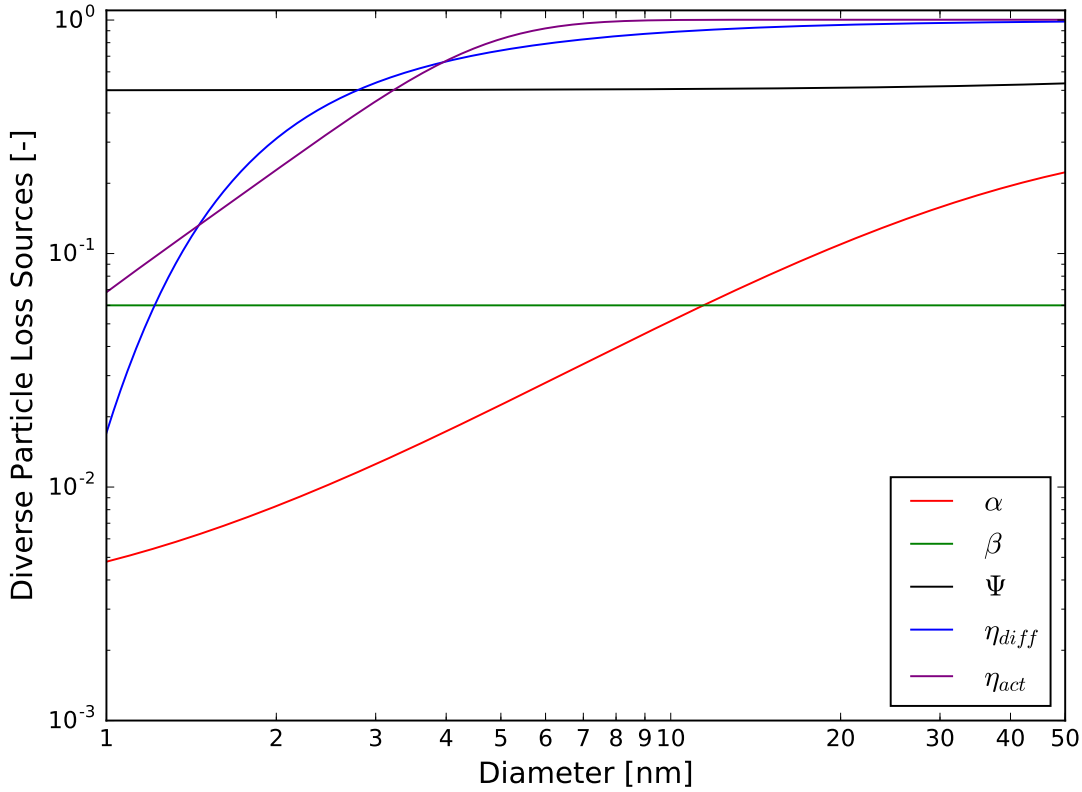

Figure 3.14: The D_p-dependency of all following factors for particles between 1 nm and 50 nm: The charging efficiency (red) is obtained from Wiedensohler (1988) for the case i=-1. The flow correction β=1.5/25=0.06 is representative for settings used further on. The Ψ-function (black) varies only by about 10%. The diffusion correction η_{diff} (blue) is attained using the equations given in Gormley and Kennedy (1949) inserting L=1m and Q=1.5 l/min. The parameters of the implemented activation efficiency η_{act} are taken from line 5 in table 1 in Hermann et al. (2007).

In conclusion, assuming just singly charged particles contributing to the CPC-Signal the number size distribution, according to Stolzenburg and McMurry (2008), can be written as

$$\frac{dN}{d\ lnD_p} = N_0(D_p) \cdot F(D_p) \tag{3.34}$$

where

$$F(D_p) = 1/\left[\alpha(D_p)_{i=1} \cdot \beta \cdot \Psi(D_p) \cdot \eta_{diff}(D_p) \cdot \eta_{act}(D_p)\right]. \tag{3.35}$$

3.4.2 Retrieval of the Full Size Distribution Function

Particles larger than 20 nm have non-negligible probabilities for being multiply charged. This results in fractions obtaining electrical mobilities equal to smaller, singly charged particles and hence superimposing their signal. Related corrections of retrieved data is thus inevitable. In order to carry out corresponding computations two necessary assumptions have to be fulfilled:

1. The size distribution must have an upper limit. This means the concentration of the largest measured particles has to equal zero. Otherwise the multiply charged fraction cannot be

computed correctly.

2. When performing an experiment the whole size distribution should change as little as possible. If this is not the case, e.g. when concentrations of larger particles vary, the contribution of larger to smaller sizes is calculated wrong as well.

For further discussion a generic size distribution in dependence on the applied DMA-voltage V is given in figure 3.15. Therein the dashed lines represent the corrected curve progression for doubly charged (red) and triply (green) particles. It is notable that the former starts at $\frac{1}{2}V_{max}$, the latter at $\frac{1}{3}V_{max}$, respectively. This circumstance is consistent when studying equation (3.16), wherein V is inversely proportional to Z: Particles which carry two (i=2) instead of one (i=1) elementary charge also possess the twofold electrical mobility. Hence, the doubly charged fraction of the largest detectable particles (classified at $V = V_{max}$ when singly charged) is observed at $\frac{1}{2}V_{max}$. Subsequently, the same considerations explain the contribution of the i-fold charged fraction starting at $\frac{1}{i} \cdot V_{max}$.

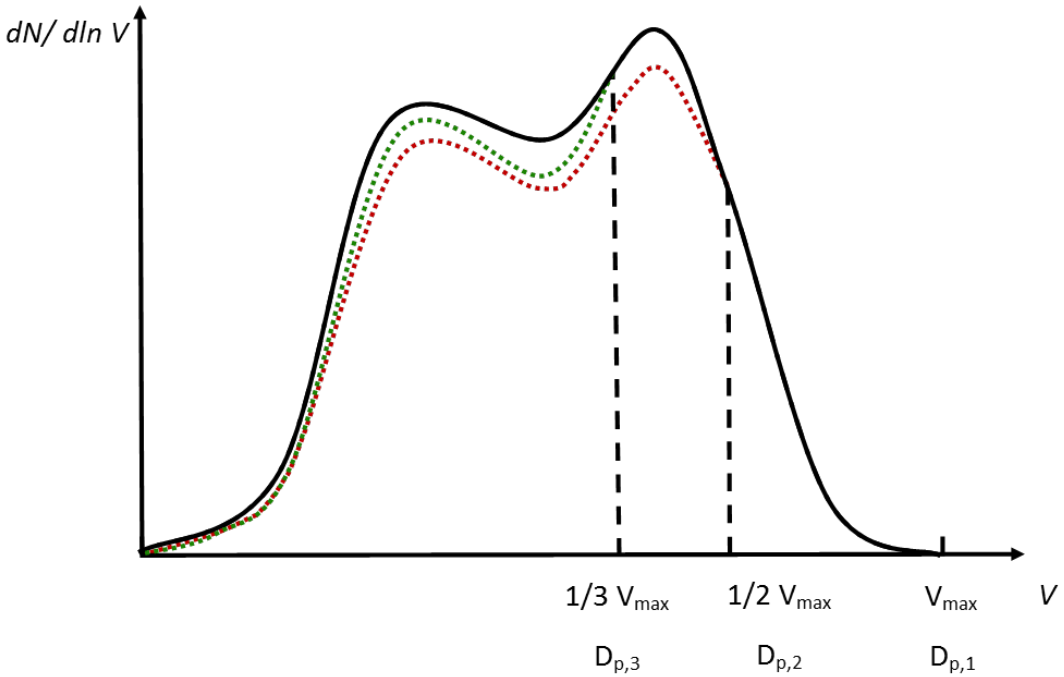

Figure 3.15: Exemplary size distribution (black) with respect to voltage V applied on the DMA. Correction solely for doubly charged particles contributing to the crude data is indicated as red dashed line. Subtraction of triply charged particles alone would yield the green dashed line. Corrections for i=2 and i=3 start at $\frac{1}{2}V_{max}$ and $\frac{1}{3}V_{max}$, respectively.

Equations 3.36 to 3.38 quantify the situation for the representative diameters $D_{p,1}$, $D_{p,2}$ and $D_{p,3}$ in the corresponding V-range.

$$\frac{1}{2}V_{max} < V < V_{max}: \quad N_0(D_{p,1}) = \frac{dN}{d\ lnD_{p,1}} \cdot \alpha(D_{p,1}, i=1) \cdot \beta \cdot \Psi(D_{p,1}) \cdot \eta_{diff}(D_{p,1}) \cdot \eta_{act}(D_{p,1}) \tag{3.36}$$

$$\begin{aligned}\frac{1}{3}V_{max} < V < \frac{1}{2}V_{max}: \quad N_0(D_{p,2}) = &\frac{dN}{d\ lnD_{p,2}} \cdot \alpha(D_{p,2}, i=1) \cdot \beta \cdot \Psi(D_{p,2}) \cdot \eta_{diff}(D_{p,2}) \cdot \eta_{act}(D_{p,2}) + \\ &\frac{dN}{d\ lnD_{p,1}} \cdot \alpha(D_{p,1}, i=2) \cdot \beta \cdot \Psi(D_{p,1}) \cdot \eta_{diff}(D_{p,1}) \cdot \eta_{act}(D_{p,1})\end{aligned} \tag{3.37}$$

$$\begin{aligned}\frac{1}{4}V_{max} < V < \frac{1}{3}V_{max}: \quad N_0(D_{p,3}) = &\frac{dN}{d\ lnD_{p,2}} \cdot \alpha(D_{p,3}, i=1) \cdot \beta \cdot \Psi(D_{p,3}) \cdot \eta_{diff}(D_{p,3}) \cdot \eta_{act}(D_{p,3}) + \\ &\frac{dN}{d\ lnD_{p,2}} \cdot \alpha(D_{p,2}, i=2) \cdot \beta \cdot \Psi(D_{p,2}) \cdot \eta_{diff}(D_{p,2}) \cdot \eta_{act}(D_{p,2}) + \\ &\frac{dN}{d\ lnD_{p,1}} \cdot \alpha(D_{p,1}, i=3) \cdot \beta \cdot \Psi(D_{p,1}) \cdot \eta_{diff}(D_{p,1}) \cdot \eta_{act}(D_{p,1})\end{aligned} \tag{3.38}$$

Attention should be paid to the expressions where $i \neq 1$. The related charging probabilities are multiplied by previously computed concentrations. In the case that no concentration was measured at one particular diameter, e.g. $D_{p,2}$, but it is essential for corrections regarding particles of smaller sizes, e.g. of diameter $D_{p,3}$, usually a fit of log-normal character between the adjacent diameters is computed, allowing the numerical determination of $\frac{dN}{d\ lnD_{p,2}}$.
As the correct retrieval of the size distribution function depends critically on the charge distribution charging probability as a function of particle size has to be precisely known. The following section describes a method for the experimental determination of charging probabilities.

3.5 Experimental Determination of the Charging Probabilities

Experimentally achieving the charging efficiency $\alpha\left(D_p, i\right)$ of unipolar (Covert et al., 1997) and bipolar (Kousaka et al., 1986) chargers is a well-established procedure. In principle the experimental setup conforms the one outlined in figure 3.16.

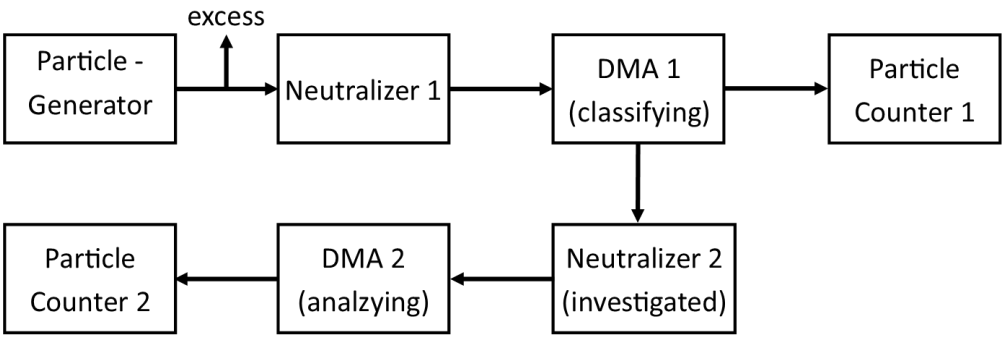

Figure 3.16: Schematic setup for measuring the charging efficiency. Aerosol particles exiting the generator are charged in neutralizer 1, classified in DMA 1, and counted in particle counter 1. The monomobile, but eventually polydisperse particles come into charge equilibrium in neutralzier 2 again. Subsequent analysing and counting yields a spectrum of all previously different charged fractions. Turning neutralizer 2 on and off or replacement with a dummy of same dimension allows computation of the charging probabilities.

Originating from a particle generator aerosol particles penetrate through neutralizer 1, wherein a steady state charging probability is achieved. Subsequently DMA 1 classifies particles of equivalent electrical mobilities, but different diameters and charging state. The sampled concentration N_1 is measured with CPC 1. Afterwards the classified aerosol particles are neutralized again, which results in a rearrangement of the multiply charged particles according to their respective $\alpha\left(D_p, i\right)$. Hence, quantitative information about the fraction, which previously carried more than one elementary charge, can be obtained when analyzing the aerosol with DMA 2. Particle Counter 2 provides the concentrations N_2 according to the observed particle sizes.
If neutralizer 2 is turned off particle counter 2 obtains the same signal as particle counter 1, when

1. adding up the concentrations of all analysed size bins.
2. including all correction factors discussed in section 3.4.1.

Consequently, the normalization N_{rel} is attainable, see equation 3.39 (Kallinger and Szymanski, 2015). There, Ch denotes one voltage step applied on DMA 2.

$$N_{rel} = \frac{\sum_{Ch} N_2(Ch)}{N_1} \tag{3.39}$$

Hereafter, the charging probability is obtained with equation 3.40.

$$\alpha(D_p, i) = \frac{N_{rel,on}}{N_{rel,off}} \tag{3.40}$$

The occurring sum must be computed according to the size range of the previously mutliply charged particles. The subscripts on and off denote, if neutralizer 2 is turned on or off. By means of the normalization no data inversion is required, since all factors (see section 3.4.1) cancel each other out.

3.6 Instrumental Considerations Related to Carrier Gas Properties

Both, experimental analysis of aerosol nanoparticles and subsequent data evaluation, i.e. achievement of the correct number size distribution, crucially depend on carrier gas properties. Differences in corresponding physical parameters are thus of great interest.
Initially, numerical values of densities ρ (Jousten, 2004, p.754), viscosities η [1] and mean free paths λ (Jousten, 2004, p.756) at standard temperature and pressure are listed listed below. The subscripts 'air' and 'he' denote, whether the values correspond to air or helium, respectively:

$$\rho_{air} = 1.293\,\mathrm{kg/m^3} \qquad \rho_{he} = 0.1785\,\mathrm{kg/m^3}$$
$$\eta_{air} = 17.3 \times 10^{-6}\,\mathrm{Pa\,s} \qquad \eta_{he} = 18.7 \times 10^{-6}\,\mathrm{Pa\,s}$$
$$\lambda_{air} = 67\,\mathrm{nm} \qquad \lambda_{he} = 175\,\mathrm{nm}$$

3.6.1 Density

The flow unit, which provides constant gas flows inside the DMA, as well as the used CPCs guarantee stable volumetric flow rates by means of critical orifices or adjustable valves.
The former utilizes a choked flow, that causes a steady gas flow output due to a constant mass flow $\dot{m}$. This is achieved by a tube fitting with a drilled hole of specific surface area A_0. Examination of equation (3.41), obtained from (Perry, 1997), shows that Q depends on both, ρ and A_0. Therein, C_0 denotes the discharge coefficient, i.e. the fraction of the surface area of the penetrating jet and A_0. The pressure across the orifice is labelled as Δp, and A equals the cross section of the tubing before the orifice.

$$Q = C_0 \cdot A_0 \cdot \sqrt{\frac{2 \cdot \Delta p}{\rho \cdot \left[1 - (A_0/A)^2\right]}} \tag{3.41}$$

Therefore, utilization of critical orifices with helium instead of air should cause significantly higher flow rates when taking the different values for ρ_{air} and ρ_{he} into account. Primary experiments confirmed this theoretical consideration and showed helium flow rates approximately twice as big as air flow rates.
In a similar way variable orifices, e.g. needle valves, cause different flow rates. Consequently, great care must be taken when operating a sensitive instrument such as CPCs with helium instead of air. Reconsidering figure 3.12 led to the concluding modifications of all CPCs:

- The critical orifice right after the optics was replaced by a variable orifice in order to achieve 0.3 l/min again.
- The variable orifice at the top left corner was substituted as well, since the present one was glued in such a way, that no adjustments were possible.

[1] https://www.engineeringtoolbox.com/gases-absolute-dynamic-viscosity-d_1888.html

Before every start of a measurement, that was carried out with helium as particle carrier gas, the orifices were adjusted in the following way.

1. Helium flow was provided and the CPC intake was set to 0.3 l/min. The variable orifice, which replaced the critical one, was carefully calibrated until the desired flow rate was drawn at the inlet.
2. The intake was still set to 0.3 l/min. The pre-existing variable orifice, which provides the sheath flow of 0.25 l/min, was also adjusted to maintain the correct gas penetration.
3. The flow rate intake was set to 1.5 l/min and the replaced orifice at the top left corner was also calibrated until 1.5 l/min were measured at the inlet.

The volumetric flow rates were always obtained using an automated volumetric bubble flow meter (Gilian Gilibrator-2 NIOSH Primary Standard Air Flow Calibrator).

3.6.2 Mean Free Path

The mean free path λ of aerosol particles in diverse carrier gases affects both, the Ψ-function as well as the Cunningham slip-correction $C(D_p)$. Corresponding functional correlations are given in equation (3.28) and (3.2), respectively. In the case of an increased mean free path, as given in the case of particles carried in helium, $C(D_p)$ increases (see figure 3.7), whereas Ψ decreases (see figure 3.7). Both changes contribute to the calculation of the number size distribution.
Examination of equation (3.16) yields the following consideration: If a higher λ is present, which is the case for helium, lower DMA-voltages are needed to classify the same particle size. If only accounting to this beneficial fact particles with mobility-equivalent diameters of up to $\simeq$63 nm would be characterized, when using a Vienna type DMA with $Q_{sh} = Q_{ex} = 25$ l/min and applying the maximum voltage of 10 kV.
However, λ also has huge impact on the DMA's breakdown voltage U_{break} (Paschen, 1889). In principal, the following mathematical derivation is only valid for homogeneous electric fields. However, this condition is not fulfilled for cylindrical capacitors since $E = E(r)$, i.e. the intensity changes with respect to the distance r from the centre (equation (3.1)). Despite this fact, a rough estimation of U_{break} can be acquired.
The physical relation is caused by the first Townsend coefficient τ, which equals the number of ionizations per length (**?**). It can be written as done in equations (3.42) and (3.43) (Liebermann and Lichtenberg, 2005, p.545).

$$\tau = \frac{\text{const}}{\lambda_e} \cdot \exp\left(-\frac{E_{iz}}{E \cdot \lambda_e}\right) \tag{3.42}$$

Here, E_{iz} corresponds to the ionization energy of the gas particles and E equals the present electric intensity. A more convenient way for concrete computation allows equation (3.43).

$$\frac{\tau}{p} = A \cdot \exp\left(-\frac{Bp}{E}\right) \tag{3.43}$$

Therein p represents the existing pressure, and the constants A and B are determined experimentally. Utilization of these values eases the theoretical computation of the breakdown voltage a lot, see equation 3.44 (Liebermann and Lichtenberg, 2005, p.546).

$$V_{break} = \frac{r \cdot ln\,(R_2/R_1) \cdot Bp}{ln\,(dpA) - ln\,[ln\,(1 + 1/\gamma)]} \tag{3.44}$$

The parameter r, R_1 and R_2 arise from substitution of equation (3.1) into equation (3.44), the constant γ represents the second Townsend coefficient. Even more simplification yields equation (3.45).

$$U_{break} = \frac{Bpd}{ln(A'pd)} \tag{3.45}$$

This relation was obtained from Massarczyk et al. (2016), where pairs of typical values for A' and B are provided as well. Implementation and comparison of all of these values results in the following breakdown voltage ranges for helium and air, respectively:

$$\begin{aligned} U_{break,he} &= 2280\,\text{V}...3920\,\text{V} \\ U_{break,air} &= 18\,610\,\text{V}...33\,590\,\text{V} \end{aligned} \tag{3.46}$$

If operated with dry air the DMA's factual breakdown voltage is known to be around 12000V, the above values for experiments conducted with helium should therefore be treated with care. Considering 3920 V as upper boundary, only particles up to $\simeq$39 nm are detectable.

Part I

Retrieval of Size Distributions of Helium-Carried Particles

4. Calibration of the DMA with Helium

Reliable measurement results in terms of correct particle diameters are only possible if the utilized DMA is calibrated for respective conditions. Corresponding procedures are thus conducted with the Vienna type nano DMA when operated with helium as carrier gas.
In simple terms, for every applied voltage the classified aerosol particle size must be known. A well-established procedure to achieve this knowledge is the analysis of aerosol standards, i.e. particles of known size and small deviations. Frequently used standards are gold nano-particles (Elzey et al., 2013), tetraheptyl ammonium bromide (THABr) (M. Gamero-Castaño, 2000), or PSL spheres (Li and Wang, 2003). The latter was used in this study, with a nominal diameter of

$$D_{p,norm} = (23 \pm 2)\,\text{nm} \tag{4.1}$$

It turned out, that the biggest difficulty consisted in generating aerosol particles, which only consisted one PSL-sphere, especially when carried in helium. Therefore experiments first were conducted in particle laden air. The principal setup and experimental procedure are explained in the following section.

4.1 Experimental Arrangement of DMA Calibration

When aiming for the calibration of a DMA the experimental assembly typically appears as given in figure 4.1.

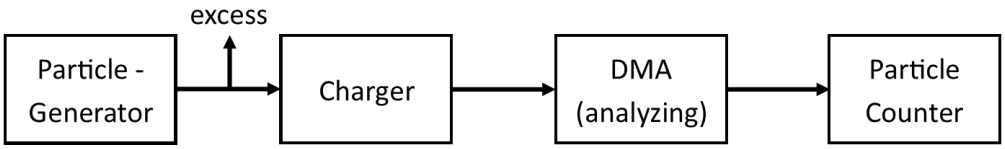

Figure 4.1: Principal setup for measurements on the spectra of aerosol nanoparticles. Particle laden gas flows through the charger/neutralizer, wherein a charge equilibrium is achieved. This yields a probability of known quantity corresponding to the particles' size. Subsequent analysis with the DMA by means of an electric field and measurement of the concentration with a particle counter yields a discrete spectrum.

A particle generator produces the particles of interest, subsequently a charger establishes a charged particle fraction. Thereafter, the DMA analyses the charged particles by means of an applied voltage, which discretely decreases, hence providing logarithmically equidistant size steps. At each size bin the corresponding number concentration is obtained using a particle counter.
Throughout the study on the DMA-calibration, two different particle generators were in use, namely the nebulizer and the electrospray (see section 3.2). An ^{241}Am alpha-ray ionizer was used as charger, an ultrafine CPC (UCPC, TSI 3776) provided the particle concentrations. Its intake flow rate was always set to 1.5 l/min, therefore the classified sampled flow Q_s always equalled the supplied aerosol flow Q_a. A flow unit always provided cleaned/dried sheath air Q_{sh}, whose volumetric flow rate always was equivalent to the non-classified DMA-excess air Q_{ex}.
Whenever experiments were performed with helium as carrier gas, the critical orifice at the flow unit, which maintained Q_{sh} and Q_{ex}, was replaced by one with a hole of smaller diameter. This substitution assured the required flow rates, see section 3.6.1. Furthermore, equally important modifications inside the CPC were achieved by installation and adjustment of variable orifices (see section 3.6.1).

4.2 Experimental Results of Nebulizer-Generated PSL-particles

At the beginning the nebulizer was used as particle generator. The schematic is given in figure 4.2.

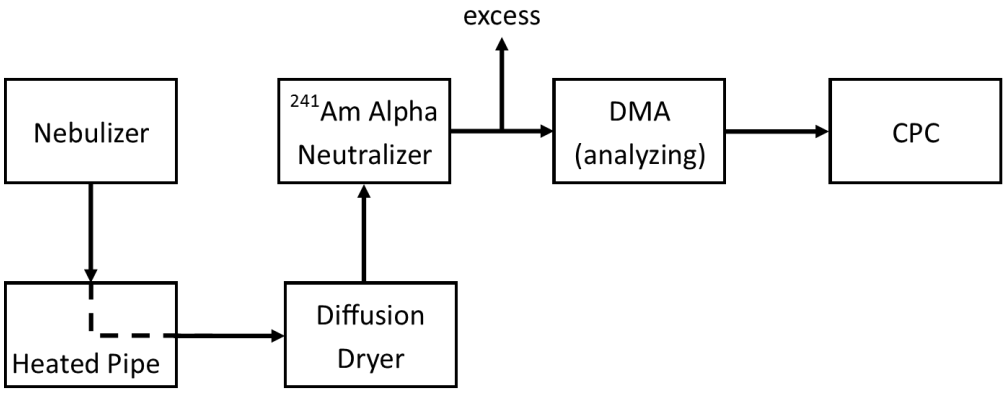

Figure 4.2: Schematic for generating aerosol particles containing only one PSL-sphere. A heated pipe and a diffusion dryer are implemented. The former causes evaporation of water molecules, the latter yields subsequent reduction of the relative humidity. Particles are charged (^{241}Am Alpha-Ray neutralizer), analyzed (DMA) and counted (CPC), hence a number size distribution is achieved.

After the aerosol generation the particle-laden gas flow penetrates through a heated pipe. This causes evaporation of the water, which previously is attached to the particles. Subsequent reduction of the relative humidity is achieved by the diffusion dryer, which is filled with silica gel. Further on the PSL-spheres are charged by an ^{241}Am Alpha-Ray neutralizer, analyzed in the DMA, and counted with the CPC in order to obtain a number size distribution.
The bottle, which provides the suspension for the nebulizer, was filled with 130 ml of ultra pure water mixed with 10 drops ($\simeq$0.5 ml) of the aqueous PSL-suspension. Nebulizing air pressure was

set to 2.1 bar, which yielded an aerosol outflow of 2.9 l/min. The heating element, and hence the pipe-penetrating water, was set to temperatures between 30 °C and 70 °C. The experimental results are illustrated in figure 4.3.

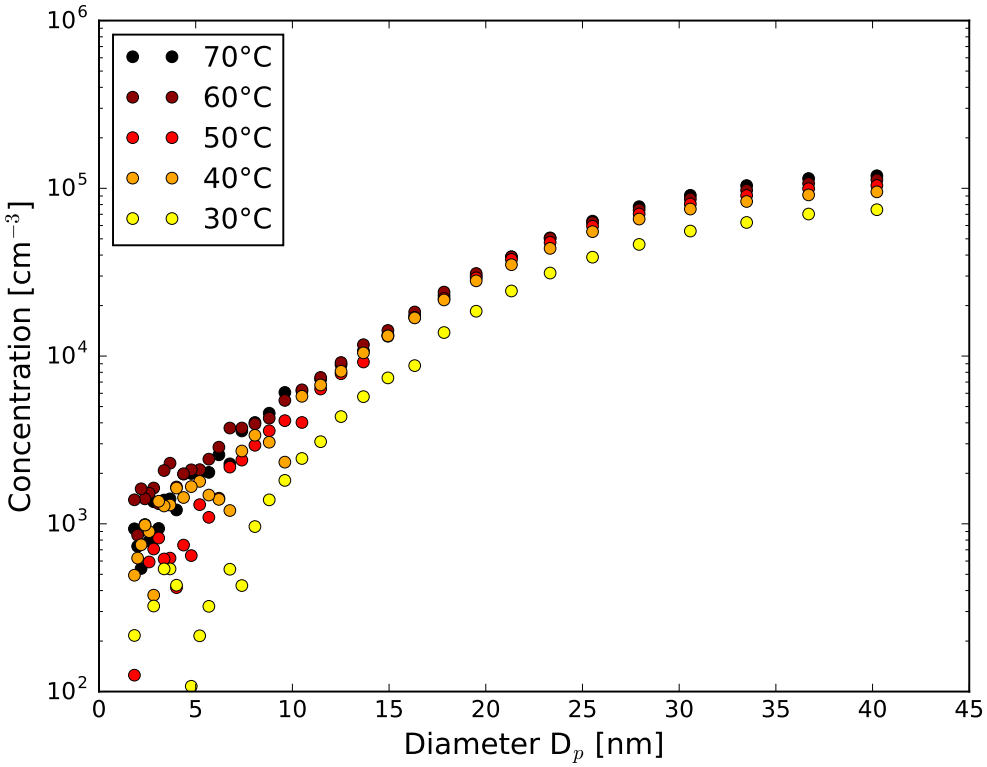

Figure 4.3: The obtained size distribution of nebulized PSL-spheres. The different colours indicate different sets of temperatures present in the heated pipe. It is obvious that this spectrum is dominated by contaminants in the water or other impurities. The envisaged improvement by means of the heated pipe and a diffusion dryer was not achieved.

It is evident that generated particle concentrations increase as temperatures in the heated tube are enhanced. Furthermore, no PSL-caused signal is observable since this would be expected around 23 nm. Due to their small size these particles are very likely lost through diffusion processes in the diffusion dryer. The resulting size distribution is thus caused by impurities in the water or residual substances in the diffusion dryer.

Although Peters et al. (1991) and Schmid et al. (2002) successfully produced PSL-particles of 65 nm and 60 nm in a similar way, respectively, corresponding attempts using spheres as small as 23 nm obviously involve further complications. In conclusion, generation of aerosol particles consisting of only one PSL-sphere of this small size is hardly possible when utilizing the nebulizer. Further experiments thus focus on electrosprayed PSL-particles, e.g. as done by Kim et al. (2005).

4.3 Experimental Results of Electrosprayed PSL-particles

Smooth operation of the electrospray aerosol generator (TSI, 3480) is a prerequisite for succesful particle generation, and hence DMA calibration. Initial experiments on the DMA-calibration were thus performed with air, and subsequently conducted with helium. Two buffer solutions were tested in air, i.e. 20 mM ammonium acetate buffer as well as pure methanol.

4.3.1 Electrosprayed PSL-particles in Air

In the beginning the 20 mM ammonium acetate buffer solution was used as suspension liquid. In order to produce this liquid 385 mg of ammonium acetate was dissolved in 250 ml ultrapure water. A standard sample vial was filled with 2ml of this solution, and subsequently 1 drop of PSL was suspended. Before each measurement start the sample vial was put into the designated mounting. Pressured air of 15 psi to 20 psi was applied, which was previously dried by use of a diffusion dryer and cleaned through activated carbon and a filter. Further on the electrosprayed PSL-particles were charged by means of an ^{241}Am Alpha-ray neutralizer, analyzed by the DMA and concentrations were obtained by using the CPC. The corresponding schematic setup is given in figure 4.4.

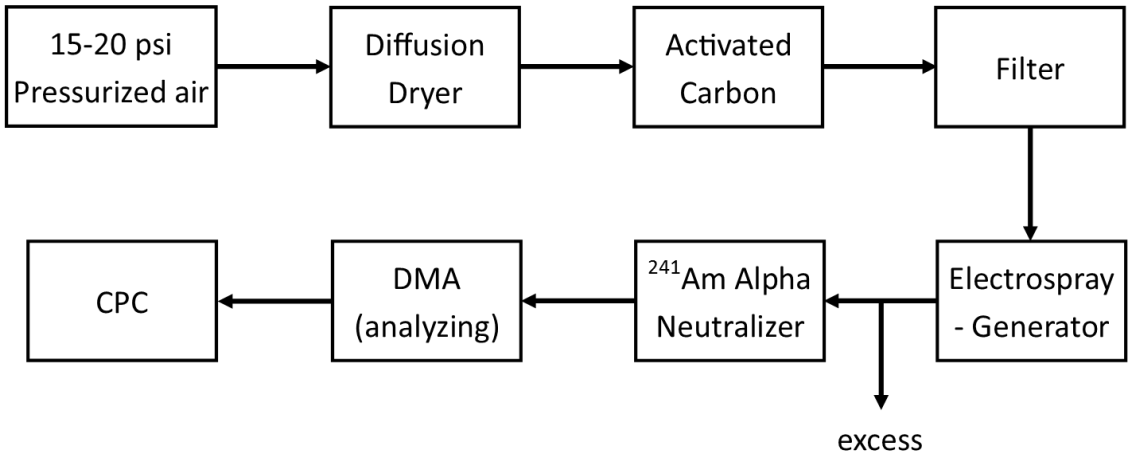

Figure 4.4: Schematic setup for generation and analysis of PSL-aerosols. Pressurized air is dried (diffusion dryer) and cleaned (activaed carbon and filter) and applied to the electrospray-generator. Subsequent particle Charging (^{241}Am alpha-ray ionizer), analyzing (DMA) and counting (CPC) yield the desired number size distribution.

Thus obtained concentrations are analyzed in terms of their corresponding DMA-voltage V, as well as the related mobility-equivalent diameters D_p. Experimental outcomes as well as two different fits (N_{norm} and N_{log}), see equations (4.2) and (4.3), are given in figure 4.5.

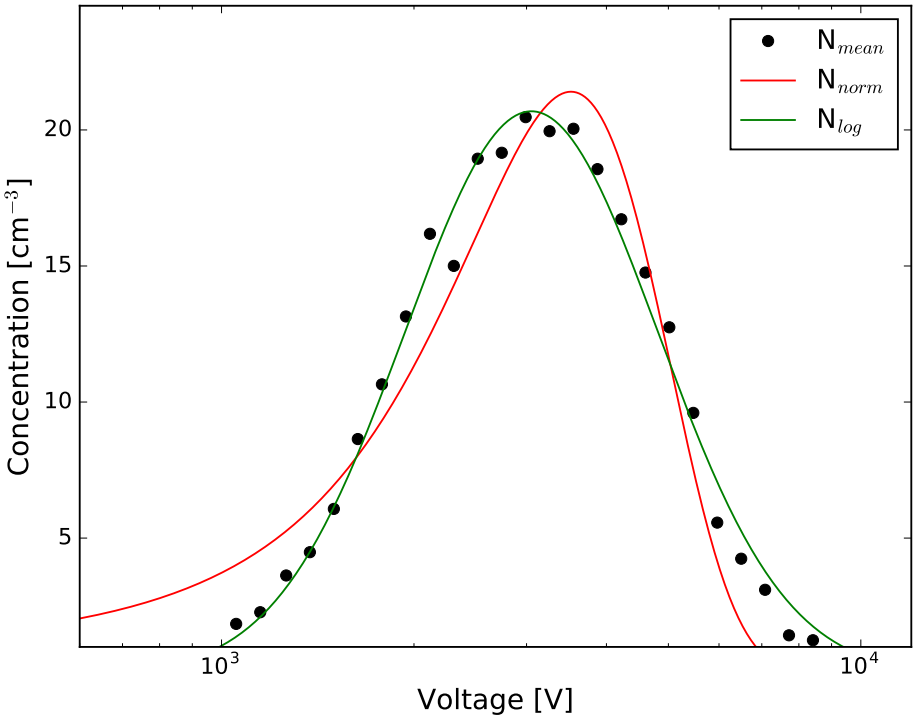

(a)

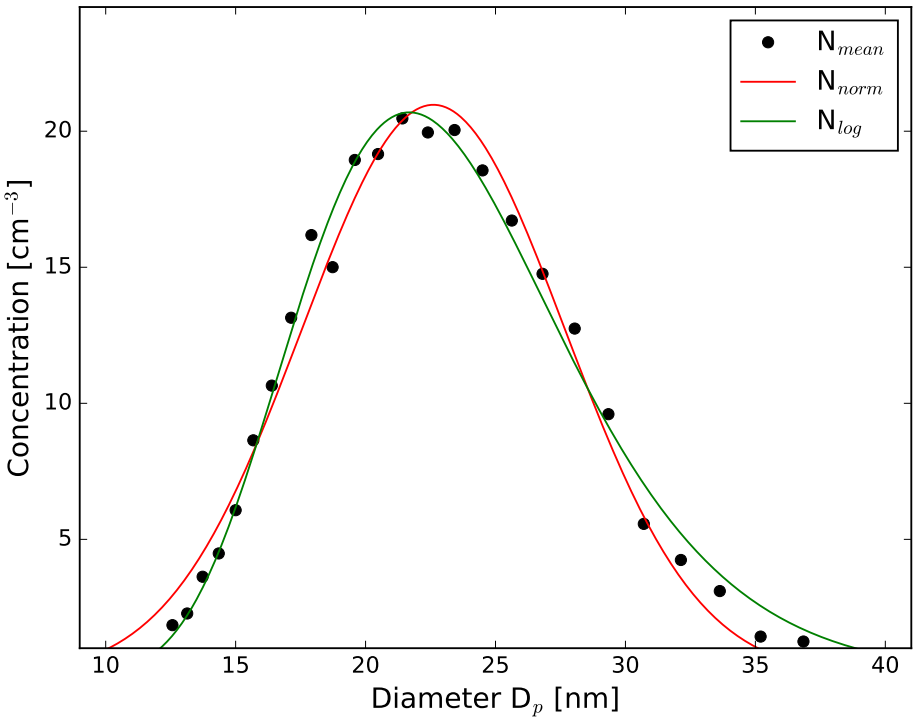

(b)

Figure 4.5: Averaged number concentration N_{mean} (black dots) in (a) V-dependence and (b) D_p-dependence for PSL-particles suspended in a 20 mM ammonium acetate buffer solution. Normal (red) and lognormal (green) distributions are fitted. The linear abscissa in (b) causes a symmetrical normal distribution, a logarithmically plotted one in (a) yields a symmetrical log-normal function. In both cases N_{log} shows better correlation to N_{mean}.

The comprised concentrations N_{mean} are mean values of 20 consecutively performed measurement runs. In each of these runs the same set of nominal voltages was applied. The fitted functions are normal (N_{norm}) and log-normal (N_{log}) distributions and their corresponding relations are given in equations (4.2) and (4.3) (Hinds, 1999, p. 362), respectively.

$$N_{norm} = A \cdot \frac{1}{\sqrt{2\pi}\sigma} \cdot exp\left[-\frac{(x-\mu)^2}{2 \cdot \sigma^2}\right] \tag{4.2}$$

$$N_{log} = A \cdot \frac{1}{\sqrt{2\pi} \cdot x \cdot ln\ \sigma_l} \cdot exp\left[-\frac{(ln\ x - ln\ \mu_l)^2}{2 \cdot ln\ \sigma_l^2}\right] \tag{4.3}$$

Therein, x corresponds to the fit variable, this is the mobility-equivalent diameter D_p or the DMA-voltage V, and the parameter A is the total particle concentration. In the former equation, μ represents the mean value, and the standard deviation is depicted as σ. In the latter μ_l is the median diameter/voltage, i.e. the value of D_p and V for which one half of all particles are detected at smaller diameters/voltages and the other half at higher quantities, and σ_l denotes the geometric standard deviation. When multiplying/dividing μ_l by σ_l the lower boundary $\mu_{l,\downarrow}$ and the upper boundary $\mu_{l,\uparrow}$ are achieved, respectively. Between these boundaries 67% of all particles are located.

Both fits are performed for $N_{mean}(V)$ and $N_{mean}(D_p)$. In order to achieve knowledge on the goodness of each fit the corresponding correlation coefficients are calculated using equation (4.4), which is obtained and adapted from Pearson (1900).

$$r_{norm/log} = \sqrt{\sum_i \left[N_{mean}(i) - N_{norm/log}(i)\right]^2} \tag{4.4}$$

In both cases r_{norm} exceeds r_{log}, therefore the according values for μ_l and σ_l of the lognormal fit are of more interest. However, for the sake of completeness μ and σ are listed below as well:

Normal:	$x = V$	$\mu = 3500\,\text{V}$	$\sigma = 1400\,\text{V}$	(4.5)
	$x = D_p$	$\mu = 22.6\,\text{nm}$	$\sigma = 5.1\,\text{nm}$	
Lognormal:	$x = V$	$\mu_l = 3760\,\text{V}$	$\sigma_l = 1.58$	(4.6)
		$\mu_{l,\uparrow} = 5940\,\text{V}$	$\mu_{l,\downarrow} = 2380\,\text{V}$	
	$x = D_p$	$\mu_l = 22.9\,\text{nm}$	$\sigma_l = 1.27$	
		$\mu_{l,\uparrow} = 29.12\,\text{nm}$	$\mu_{l,\downarrow} = 18.06\,\text{nm}$	

Considering the PSL spheres' nominal diameter of (23±2)nm the computed mean diameter shows reasonable agreement, however, more precise measurements are desired. Therefore analogous experiments were conducted by using pure methanol as buffer solution. Again, the experimental arrangement corresponds to the one depicted in figure 4.4. One drop of the PSL-suspension was mixed with 2 ml of pure methanol and the filled sample vial was put into the electrospray-generator. The obtained concentrations of 15 consecutively performed measurement runs were averaged and fitted again in terms of V and D_p. Both, the mean values and the numerical approximations, are given in figure 4.6.

For the V-dependent fit r_{log} exceeds r_{norm}, but when approximating the functional relation of N_{rel} to D_p it turns out that r_{log} is lower than r_{norm}. Again, the complete set of the fitted parameters is listed below:

Normal:	$x = V$	$\mu = 3400\,\mathrm{V}$	$\sigma = 770\,\mathrm{V}$	(4.7)
	$x = D_p$	$\mu = 22.7\,\mathrm{nm}$	$\sigma = 2.8\,\mathrm{nm}$	
Lognormal:	$x = V$	$\mu_l = 3460\,\mathrm{V}$	$\sigma_l = 1.27$	(4.8)
		$\mu_{l,\uparrow} = 4390\,\mathrm{V}$	$\mu_{l,\downarrow} = 2720\,\mathrm{V}$	
	$x = D_p$	$\mu_l = 22.79\,\mathrm{nm}$	$\sigma_l = 1.14$	
		$\mu_{l,\uparrow} = 25.98\,\mathrm{nm}$	$\mu_{l,\downarrow} = 19.99\,\mathrm{nm}$	

In conclusion, ammonium acetate buffer solutions as well as pure methanol allow the generation of aerosol nanoparticles composed of only one PSL-sphere. Although undesired contaminants might be present in both suspensions, application of the electrospray technique thus yields the desired outcome.
Additional second peaks caused by doubly charged fractions are scarcely observable, mainly due to the extremely low charging probabilities for particles of such small sizes. Furthermore, even if corresponding concentrations existed, their contribution would still lie in the primary peak, which is caused by singly charged particles. The existence of particles comprised of two spheres is not ascertainable, since particles larger than 40nm are beyond the detection limit.
Since utilization of pure methanol yields far narrower size distributions it is consequently used for analogous experiments performed with helium as carrier gas.

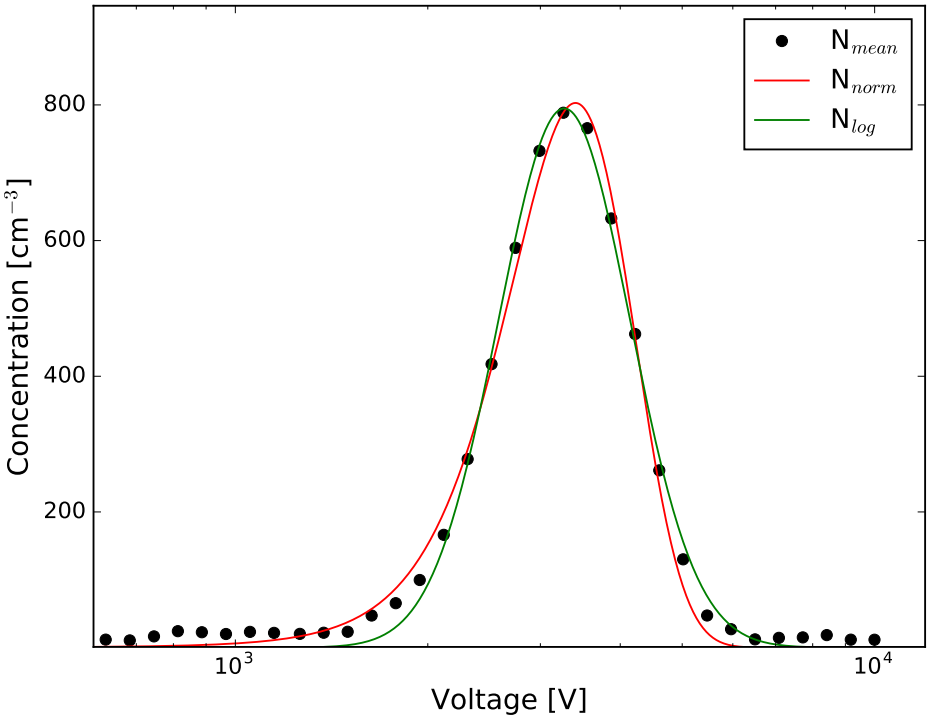

(a)

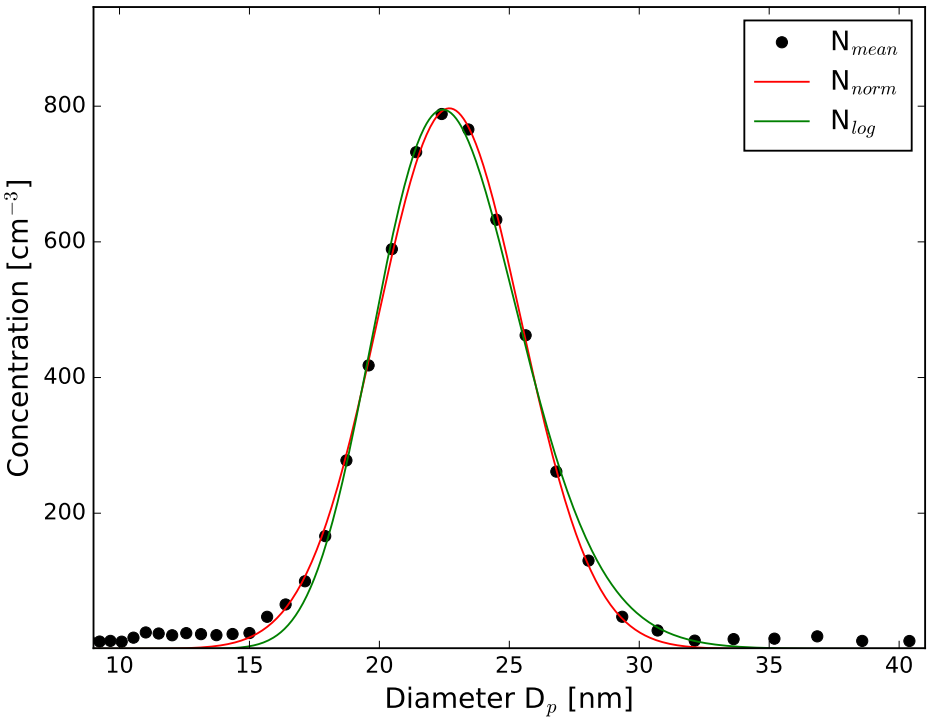

(b)

Figure 4.6: Averaged number concentration N_{mean} (black) in (a) V-dependence and (b) D_p-dependence for PSL-particles suspended in pure methanol. Normal (red) and log-normal (green) distributions are fitted. N_{log} shows better correlation to N_{mean} in (a), however, more satisfying approximation in (b) is achieved using N_{norm} .

4.3.2 Electrosprayed PSL-particles in Helium

Acquisition of corresponding peaks in the size distribution caused by helium-carried PSL-particles turned out to be rather labour intensive. This was mainly due to difficulties obtaining continuous output by means of the electrospray generator, which again involved further complications in the experimental conduction.

The schematic setup equalled the one already depicted in figure 4.4, with the exception that pressurized helium was used. Another difference compared to previous measurement conductions were reduced volumetric flow rate settings of sheath flow Q_{sh} and excess flow Q_{ex} . Decreasing these quantities to

$$Q_{sh} = Q_{ex} = 8.6\,\text{l/min}$$

resulted in enhancement of the upper detection limit. Exchange of the carrier gas, however, led to differences in the required generator settings. For instance, a minimum volumetric flow rate of 1.5 l/min had to be provided since this conformed the CPC's uptake. In order to achieve higher output the applied pressure was increased, which again led to the necessity of increased voltage. Variation of one parameter therefore initiates careful adaptations of all the others so that a Taylor cone, and thus steady particle production, are ensured. The respective ranges of all settings proved to be far narrower compared to corresponding intervals if operating with air.

Occasional clogging of the capillary tip inside the electrospray generator caused immediate measurement stops and additionally required subsequent rinsing and cleaning using a 20 mM KOH solution. Of course, when ensuing measurements were started, the whole arrangement again needed a certain amount of time until is was fully operating with helium, and thus correct flow rates present. As a consequence, stable particle output for longer durations than a couple of minutes were seldom achieved, but satisfying measurement results have been monitored nevertheless.

The most promising results can be seen in figure 4.7, which displays the obtained concentrations in dependency on DMA-voltage and mobility-equivalent diameter when using the same methanol-suspension as before.

It is worth noting that the latter depiction is based upon theoretical values for D_p, which are computed by the measurement software. Even though all essential parameters for helium (e.g. viscosity, mean free path, etc.) are implemented into the program, thus retrieved diameters are not correct. This matter of fact is crucial for further calculations on the correct size distribution function and it is evident when observing figure 4.7(b): The peak of the PSL-particles' distribution clearly deviates from its nominal 23 nm.

All fitted parameters corresponding to both, the voltage- and particle size-dependent distribution, are given in the table below, see (4.9) and (4.10). These values are again achieved using equations (4.2) and (4.3), and r_{log} exceeded r_{norm} both times.

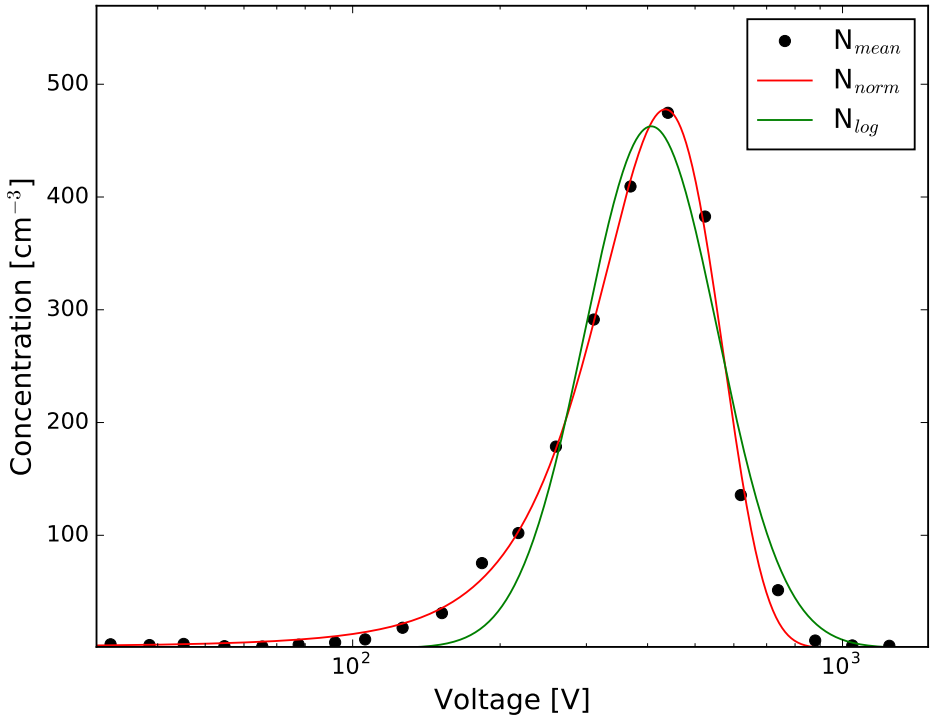

(a)

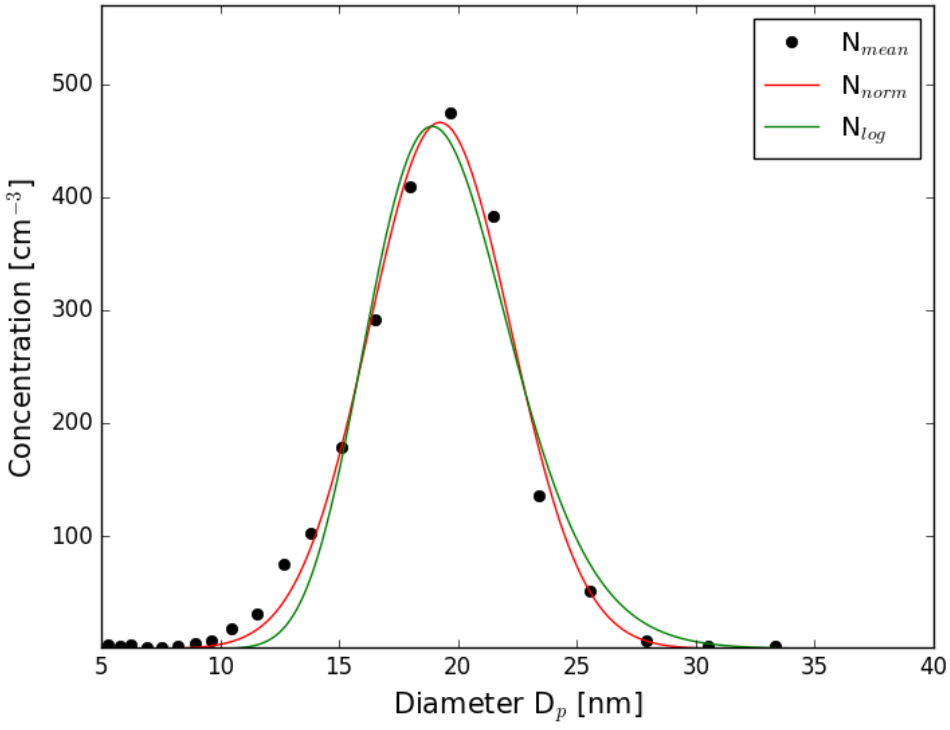

(b)

Figure 4.7: Averaged number concentration N_{mean} (black) in (a) V-dependence and (b) D_p-dependence for helium-carried PSL-particles suspended in pure methanol. Normal (red) and log-normal (green) distributions are fitted. N_{norm} shows better correlation to N_{mean} in both, (a) and (b).

Normal:	$x = V$	$\mu = 430\,\mathrm{V}$	$\sigma = 130\,\mathrm{V}$	(4.9)
	$x = D_p$	$\mu = 19.2\,\mathrm{nm}$	$\sigma = 3.0\,\mathrm{nm}$	
Lognormal:	$x = V$	$\mu_l = 450\,\mathrm{V}$	$\sigma_l = 1.37$	(4.10)
		$\mu_{l,\uparrow} = 620\,\mathrm{V}$	$\mu_{l,\downarrow} = 330\,\mathrm{V}$	
	$x = D_p$	$\mu_l = 19.4\,\mathrm{nm}$	$\sigma_l = 1.18$	
		$\mu_{l,\uparrow} = 22.9\,\mathrm{nm}$	$\mu_{l,\downarrow} = 16.4\,\mathrm{nm}$	

4.4 Data Evaluation for Further Analysis

Measurement results of the previous section allow subsequent computations on DMA calibration, which is done as follows:

1. Acquisition of the DMA's particular classification length
2. Computation of correct particle diameters corresponding to a set of applied voltages
3. Determination of the numerical parameter providing functional relation between thus obtained diameters and previously known values (computed by the measurement software)

Rearrangement of equation (3.16) yields the following:

$$L = \frac{3\pi \cdot \eta \cdot D_p}{i \cdot e_0 \cdot C(D_p)} \cdot \frac{1}{V} \cdot \frac{ln(R_2/R_1)}{2\pi} \cdot \frac{Q_{sh} + Q_{ex}}{2}. \tag{4.11}$$

Substitution of the found values for V and D_p from equation (4.9) consequently allows calculation of the DMA's classification length L_{he}, see equation (4.12). The related error is retrieved via Gaussian error propagation of corresponding standard deviations:

$$L_{he} = (15.9 \pm 5.2)\,\text{mm} \tag{4.12}$$

Reinsertion of L_{he} as well as the same set of applied voltages V as depicted in figure 4.7(a) into equation (3.16) results in an according multitude of diameters D_p^{he}. Due to the equation's transient character straight-forward calculations of uncertainties ΔD_p^{he} are impossible, which is why the length's lower and upper limit (10.7 mm and 21.1 mm, respectively) are computed with all values for V as well. Thus obtained data determines the uncertainties illustrated in figure 4.8. Therein, the abscissa represents the diameters D_p^{nom} taken from the measurement software.
In order to quantify the functional relation between the quantities D_p^{nom} and D_p^{he} the gradients of three linear fits were obtained. Each of these approximations corresponds to one specific DMA classification length:

- solid line: mean length L_{he}=15.9 mm
- dashed line: upper limit length L_{he}=21.1 mm
- dotted line: lower limit length L_{he}=10.7 mm

The slopes of the external fits determine the computed multiplier's M_D uncertainties:

$$M_D = 1.16 \pm 0.18 \tag{4.13}$$

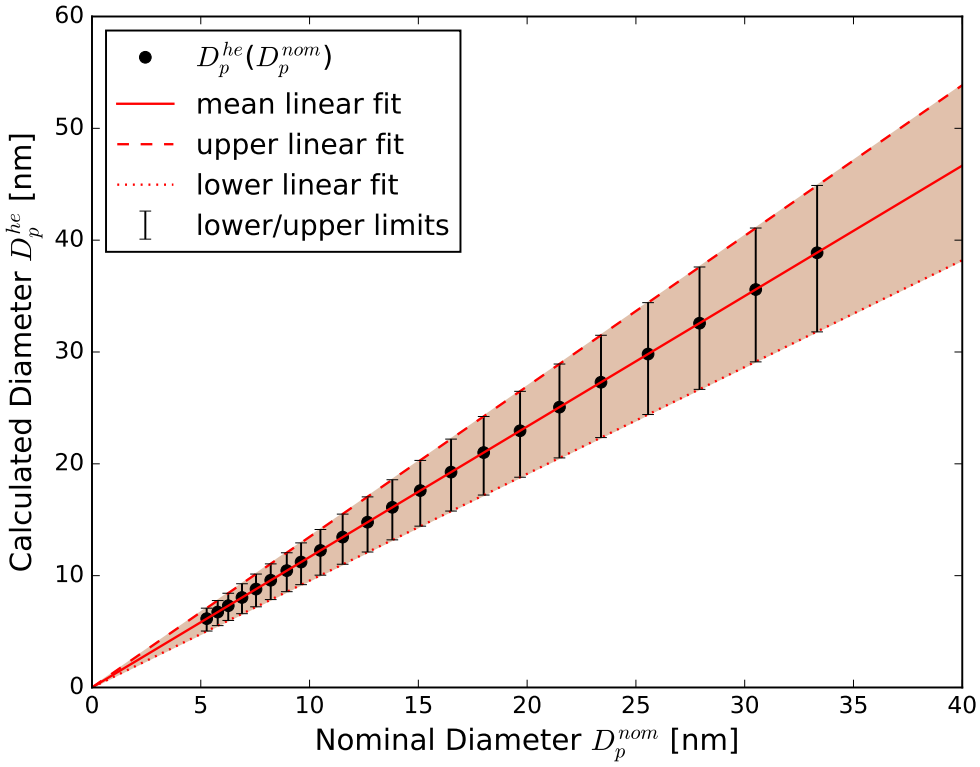

Figure 4.8: Numerical computation of the multiplying factor M_D. Three corresponding slopes allow retrieval of the upper (dashed line) and lower (dotted line) limit, as well as the mean value (solid line). The error bars depict these limits and relate to the mean values' uncertainties.

As a consequence, if the actual particle's diameters D_p^{he} are of interest when operating the DMA with helium, provided quantities D_p^{nom} solely have to be multiplied by M_D. This convenient operation significantly eases further computations targeting the full size distribution function (see section 7).

5. Measurement of the Charging Probability

5.1 Alternative Experimental Assembly

Although the experimental setup explained in section 3.5 should be first choice if measurements of $\alpha(D_p, i)$ are needed it sometimes may have practical drawback. First, two DMAs are absolutely essential, including correct flow provisions and high-voltage control. Second, if using different carrier gases than air, e.g. helium, maintaining flows only composed of the desired carrier gas needs a lot of time. In conclusion, performance of such measurements is a question of laboratory equipment and money. An alternative way for experimental determination of the charged fraction is presented here, yielding two major improvements:

1. Experimental accomplishment is possible using only one DMA.
2. Crucially less time is needed until the complete arrangement is filled with one gas type.

A schematic of this setup is given in figure 5.1. Compared to figure 3.16 DMA 2 is replaced by an ion trap. This instrument allows the removal of all charged particles of an aerosol up to a certain maximum electrical mobility by means of an electric field. Therefore, if the ion trap is turned on, only neutral aerosol particles reach particle counter 2, which obtains concentration N_2. As a consequence no signal is obtained if neutralizer 2 is turned off, since only charged particles are selected by the DMA. Otherwise, if neutralizer 2 is turned on a diameter-dependent steady state charging probability is achieved again. Hence, only neutral particles are able to penetrate through the ion trap. According reference measurements are carried by particle counter 1, yielding the concentration N_1. Sheath flow and excess flow (both set to 24.7 l/min, respectively) are provided by a flow unit and equal those present in analogous experiments when air-carrier particles are analyzed. This flow unit allows

- constant flow conditions using a pump in combination with a critical orifice.
- sufficient cleaning and drying of the particle laden air by use of a HEPA filter, silica gel and active carbon.

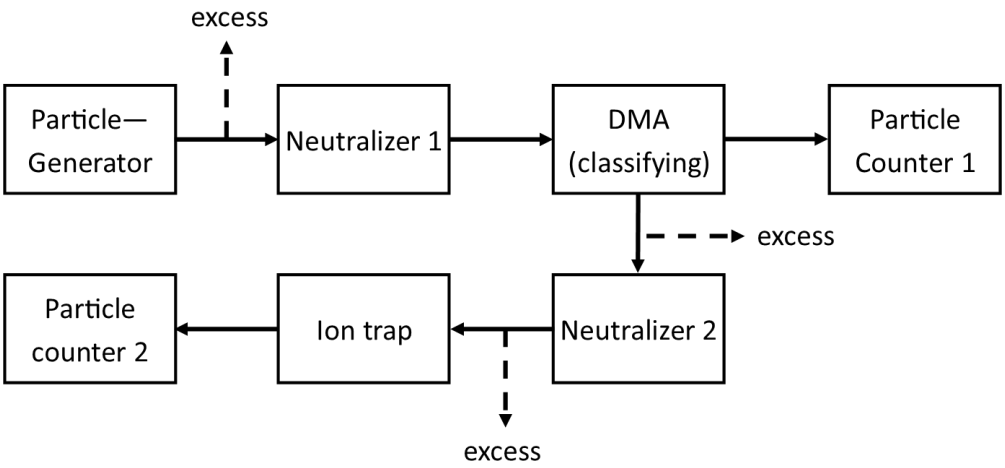

Figure 5.1: Alternative schematic for measurement of the charged particle fraction. Neutralizer 1 charges the generated aerosol particles, which subsequently are classified in the DMA. Following this, the selected particles are counted with particle counter 1, and again charged with neutralizer 2, yielding different electrical mobilities and neutral particles. The complete charged fraction is removed by applied voltage on the ion trap, hence only neutral particles are counted in particle counter 2. The dashed lines indicate the positions of the excess. The former ensures constant sample flow rates into the DMA, exchange of the latter two excess positions allows variation of corresponding flow rates through neutralizer 2.

Recalling the quantitative evaluation of the charging probability in section 3.5 allows an equivalent derivation for the current measurement setup. Depending on the neutralizer operating conditions (on or off) two relative particle concentrations are obtained:

$$N_{rel,off} = \frac{N_{2,off}}{N_1} \tag{5.1}$$

$$N_{rel,on} = \frac{N_{2,on}}{N_1} \tag{5.2}$$

The subscripts on and off denote whether the ion trap was turned on or off. The probability for particles being not charged, i.e. the neutralization probability/efficiency P_{neu}, can then be written as follows:

$$P_{neu} = \frac{N_{rel,on}}{N_{rel,off}} \tag{5.3}$$

Besides its crucial experimental advantages the presented method has one large drawback: Not the charging efficiency is determined, but the probability for particles not being charged. Therefore one does not acquire noteworthy information on the number of elementary charges the particles are carrying. Considering this, reliable analysis is only possible for smaller particles ($<$20 nm), i.e. when their probability for carrying two or more elementary charges is negligible.

5.2 Measurement Results of the Charging Efficiency in Air

In order to test the proposed measurement technique the neutralization probability of particles penetrating through a soft X-ray charger (Advanced Aerosol Neutralizer, TSI 3088) was determined using air as carrier gas. The experimental arrangement corresponds to the one given in 5.1. A tungsten oxide - generator was used as particle source, providing a particle laden flow of 3 l/min. Two X-ray Chargers operated as neutralizers and two CPCs (UCPC, TSI 3776) provided particle concentrations. A non-commercial ion trap completed the assembly. The inlet flow rate of CPC 1 was always set to 1.5 l/min, the one of CPC 2 was changed in order to achieve different flows penetrating through neutralizer 2. Furthermore, the position of the last exhaust was changed as well, also yielding different charger flow rates.
The charging probabilities are computed using equations (5.1), (5.2) and (5.3). The inserted particle concentrations were achieved by calculation of mean values over 100s ending 10s before the ion trap was turned on, as well as averaging for 100s starting 10s after activation of the ion trap. This averaging processes are indicated in figure 5.2, where the temporal trends of the concentrations N_1 and N_2 (measured with CPC 1 and CPC 2) are illustrated. Concentration N_1 (blue) only shows little fluctuations in time. Therefore, a constant particle output of the WO_x-generator can be assumed. N_2 (green) slightly decreases when the ion trap is turned on (left dashed line) and drops to zero when neutralizer 2 is turned off (right dashed line). The red bars mark the averaging periods.
The concentration gap between N_1 and N_2 arises from diffusional losses. Reconsideration of figure 5.1 shows that particles contributing to N_2 additionally penetrate through another X-ray charger as well as the ion trap. The neutralizer's equivalent length for such losses equals 1.51 m, the trap measures 0.05 m. Substituting these quantities, as well as the particle's mobility-equivalent diameter (5 nm) and present flow rates (1.5 l/min) into equation (3.31) results in the following penetration efficiency:

$$\eta \simeq 0.73$$

Average values of both concentrations in the left part of figure 5.2 are as follows:

$$N_1 = (35600 \pm 3600)\ \text{cm}^{-3}$$

$$N_2 = (24600 \pm 2500)\ \text{cm}^{-3}$$

Inclusion of diffusional losses thus clearly shows, that both concentration can be assumed equal within their uncertainties:

$$N_2 \simeq N_1 \cdot \eta$$

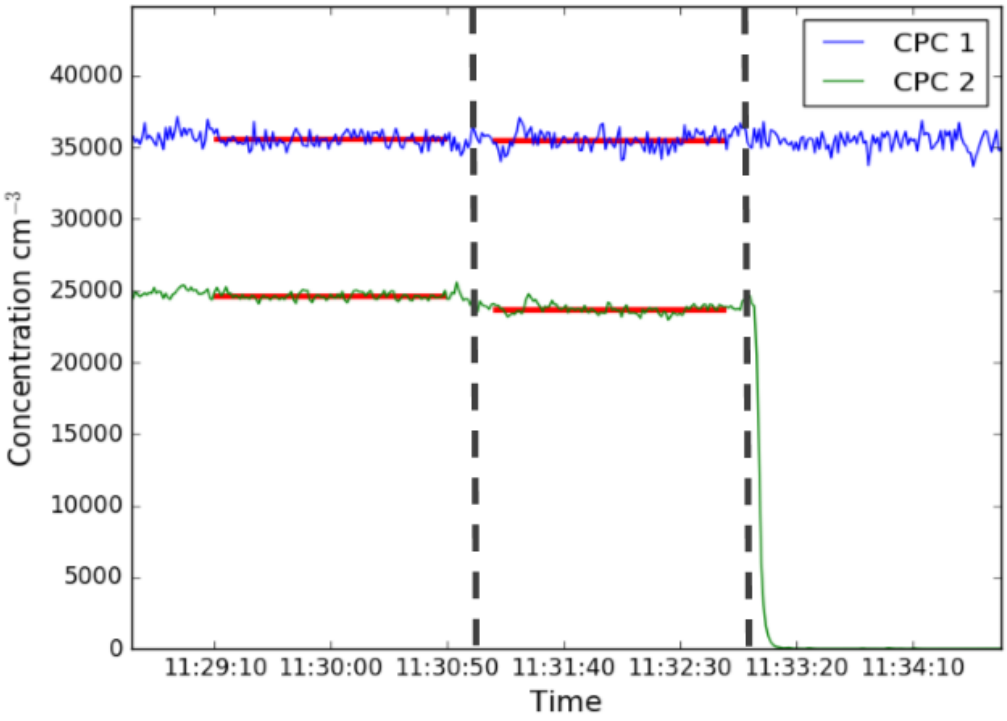

Figure 5.2: Time-resolved concentrations measured with CPC 1 (blue) and CPC 2 (green). The left dashed line marks the time when the ion trap was turned on, the right one indicates the moment when neutralizer 2 was turned off. With respect to these process N_2 decreases as only neutral particles / no particles are detectable, respectively. The red lines displays the time, during which the data was averaged.

Figure 5.3 comprises the computed charging probabilities for three different excess flow settings illustrated with different colours:

blue:	excess position: before DMA	CPC 2 intake: 1.5 l/min
red:	excess position: before neutralizer 2	CPC 2 intake: 0.3 l/min
green:	excess position: after neutralizer 2	CPC 2 intake: 1.5 l/min

Very small variations in the probabilities allow the assumption that the probabilities do not change with respect to the excess position or the intake flow rate of CPC 2. Consequently, for the considered flow rates the charger residence time is found to achieve charge equilibrium. Furthermore, the obtained data show very good agreement with the theoretical values.
Black lines represent the probabilities for particles carrying one elementary charge, independent of the sign. Corresponding computations were concluded as done by Wiedensohler (1988) and Fuchs (1963), respectively, thus yielding the solid and dashed line. The counter probability (orange line) for particles being neutral (i=0), i.e. the charged fraction, is again based on calculations given by Fuchs (1963). Respective values according to Wiedensohler (1988) are not illustrated as they show non-physical behaviour and provide no additional insight.
In conclusion of the data depicted below, the proposed measurement technique meets the desired conditions and is therefore also carried out with helium as carrier gas.

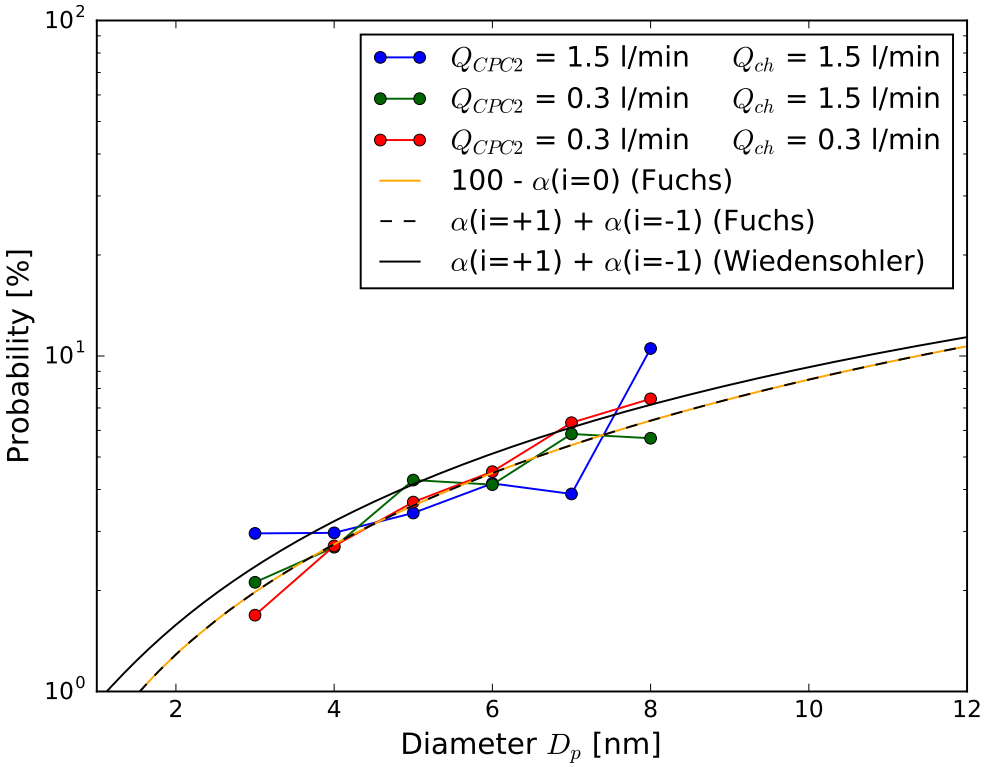

Figure 5.3: Measured charging probabilities of tungsten-oxide particles. Three different combinations of excess position and CPC 2 - intake adjustments were used, yielding two different charger flowrates. Black lines mark the complementary probabilities of particles being not charged (i=0) according to Wiedensohler (1988) (solid) and Fuchs (1964) (dashed), respectively. The orange line indicates the probability for particles carrying one negative (i=-1) or positive (i=+1) charge, again as given by Fuchs (1964). Relative uncertainties of all probabilities are between 5% and 15% and are not displayed for a better overview.

5.3 Measurement Results of the Charging Probability in Helium

When performing analogous experiments with helium the specific carrier gas properties (section 3.6) should be reconsidered. In summary, the following experimental setup rearrangements or measurements were conducted:

- The flow rates in the CPC were adjusted by installation of two variable orifices
- The time the system needed in order to fully operate with helium was measured.
- An FCE was utilized as particle counter 1 because:
  - after classification by the DMA all particles are charged, and thus detectable by the FCE
  - flow rate adjustments require less time

For the proper operation of the DMA with helium the critical orifice of the flow unit was replaced in order to achieve correct sheath and excess flow rates of 24 l/min. Furthermore, the maximum voltage, that can be applied on the DMA, was obtained. The schematic setup (see figure 5.4) is slightly different to the one when charging probabilities in air were measured. Instead of the WO_x - generator the hot-wire generator, containing an installed tungsten wire, was used as a particle source. Again, an aerosol flow of 4 l/min was provided. The same X-ray chargers were used as in the previous experiments. An FCE and a CPC were operated as particle counter 1 and particle counter 2, respectively. The intake flow rate of both was set to 1.5 l/min. Furthermore, it is noteworthy that the excess flow was not connected with an exhaust line, but just a HEPA filter. Otherwise the desired flow conditions were not achieved, which might be linked to slight, but significant additional uptakes , thus causing unreasonable measurement results.

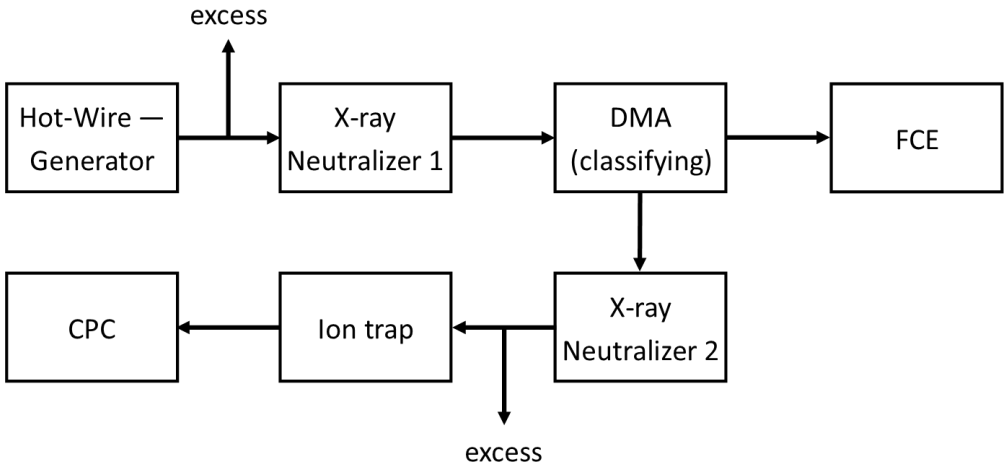

Figure 5.4: Detailed schematic for measurement of the charged particle fraction in helium. Nanoparticles are produced in the hot-wire generator containing a heated tungsten-wire. Again, two X-ray neutralizers operate as chargers. The total particle number concentration after the DMA is measured by means of an FCE instead of a CPC.

The maximum DMA-voltage was found to be ∼1.2 kV, which is even less than the expected value of 2.28 kV ... 3.92 kV. As a consequence, only particles up to mobility-equivalent diameters of ∼21 nm are selectable. However, the ion trap's breakdown voltage was found to be ∼ 300 V, which is why an upper limit of 11 nm is imposed.
Two measurements were performed, which aimed for the charging probabilities. In both cases the excess was put right after the hot-wire - generator, which implies a flow rate of 1.5 l/min penetrating through X-ray neutralizer 2. The obtained data is given in figure 5.5.

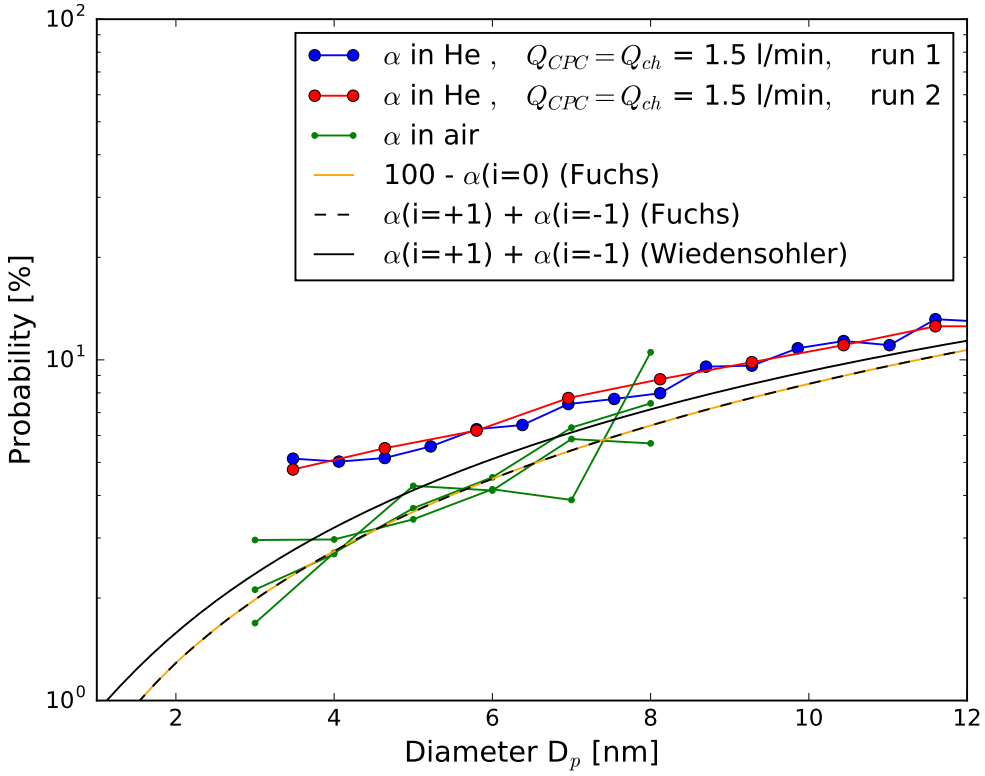

Figure 5.5: Two consecutively conducted measurement runs (blue and red) of charging probabilities in helium performed with a charger flow rate Q_{ch} of 1.5 l/min. The green dots denote previous data obtained when using air as carrier gas. Again, black lines (dashed and solid) indicate theoretically computed probabilities according to Fuchs (1964) and Wiedensohler (1988), respectively, for singly charged particles in air. The orange line marks the complementary probability for air-carried particles being neutral accoring to Fuchs (1964) .

The measured probabilities for particles carried in helium (red and blue) only show little deviation compared to each other. Previous measurement outcomes in air (green dots) are significantly lower, i.e. by a factor of 1.12 ... 1.89 if averaged at each size. This particle size dependent difference casts doubt whether the achieved data is reasonable over the obtained size range and led to the assumption, that unknown charging mechanisms in the neutralizers might contribute to this effect. In order to examine this consideration the helium flow through the hot-wire - generator was increased and the exhaust was located behind X-ray neutralizer 2. This rearrangement resulted in a larger charger flow. Again, two measurement runs were performed, each with a different charger flow, which was obtained with

$$Q_{ch} = Q_{CPC} + Q_{ex}. \tag{5.4}$$

Therein, Q_{CPC} equals 1.5 l/min and the excessing flow Q_{ex} was achieved using an automated volumetric bubble flow meter (Gilian Gilibrator-2 NIOSH Primary Standard Air Flow Calibrator). The measured charging probabilities (orange and red) are depicted in figure 5.6, as well as the previously measured probabilities (blue), when helium was used as aerosol gas as well.

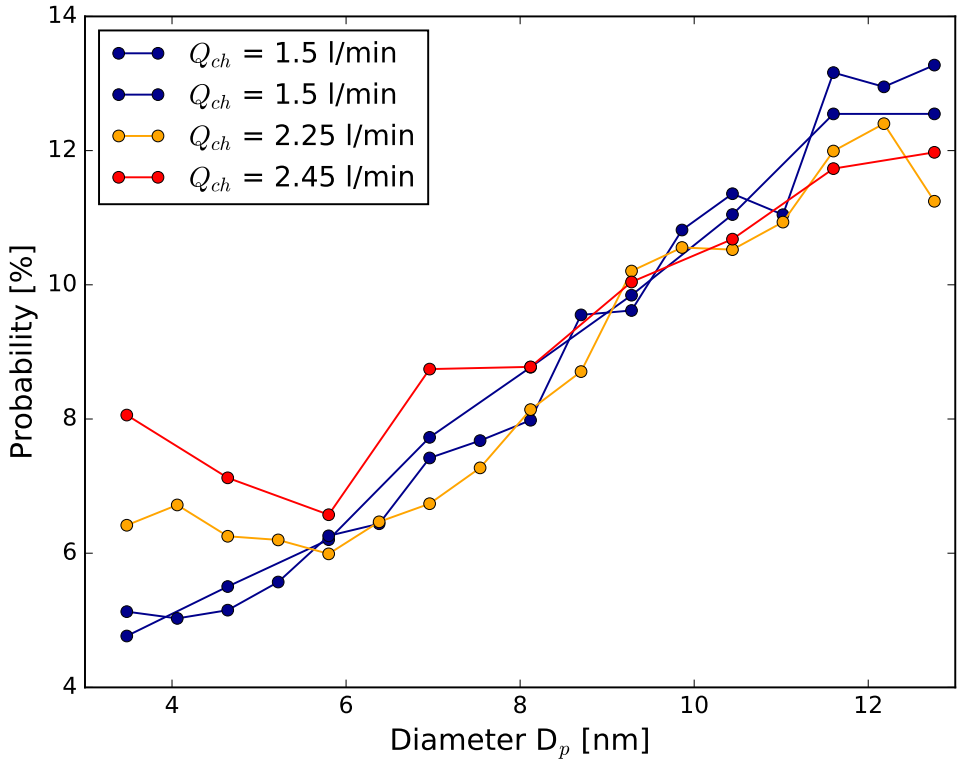

Figure 5.6: Measured charging probabilities in helium performed with charger flow rates of 1.5 l/min (blue), 2.25 l/min (orange) and 2.45 l/min (red), respectively. For particles <6 nm the obtained efficiencies increase when higher flows penetrate through X-ray charger 2.

It is evident, that charging probabilities of smaller sized particles increase when enhancing the charger flow rate. This fact is very likely due to particles of lower diameter requiring a longer residence time in X-ray neutralizer 2 in order to reach a charge equilibrium. Similar size dependencies of charged fractions were also found by Alonso et al. (1997), who measured corresponding charging probabilities of particles below 10 nm after one to five chargers, thus obtaining information on residence time depending mechanisms.
Further examination of the charging probabilities obtained at charger flowrates of Q_{ch}=1.5 l/min, see figure 5.5 (red and blue) and figure 5.6 (blue), is carried out in the following section. This allows the numerical retrieval of continuous information on the helium carried tungsten particles' charging probabilities.

5.4 Charging Probability Data Evaluation

Continuous information on the functional relation of charging probabilities α with respect to particle diameters D_p is essential for subsequent computations of size distributions. Derivation of this dependency is achieved using the function as given in Wiedensohler (1988), wherein two corrected parameters, stated in Flagan (2008), are implemented. The resulting, partly averaged data, is given in figure 5.7 (black).

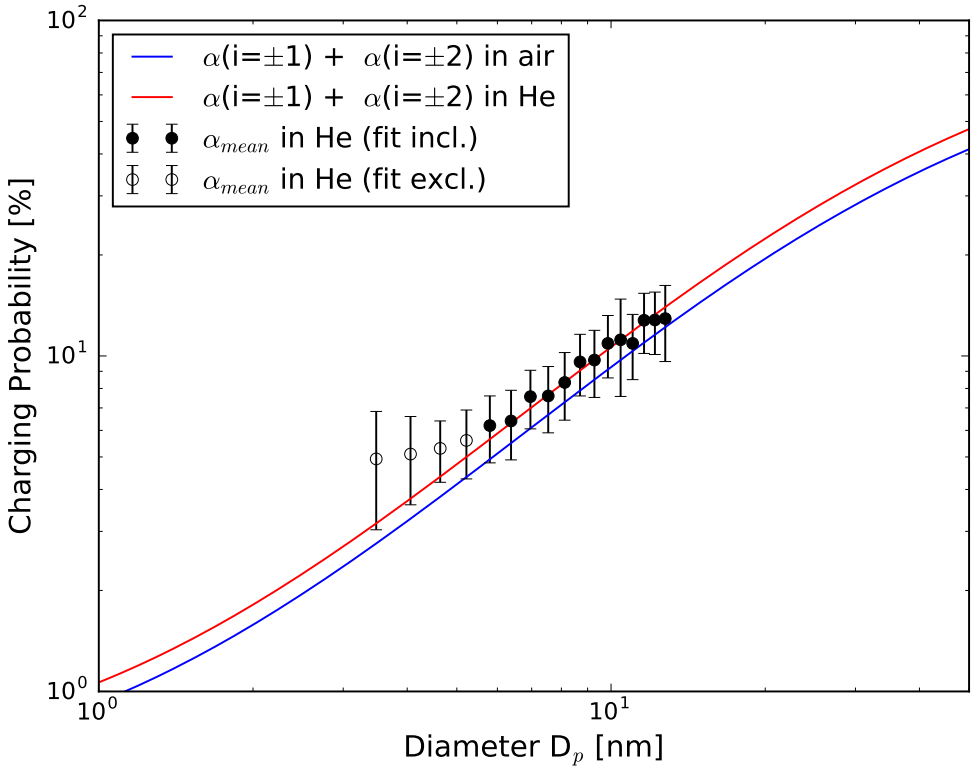

Figure 5.7: The partially averaged charging probabilities (black) of particles carried in helium. The filled/empty circles mark the data, which was included / not included for the numerical fit (red). The blue curve denotes the singly and doubly charged fraction according to Wiedensohler (1988). If multiplied by a_0 the blue line yields the red one. The error bars originate from the propagation of uncertainties, these are the standard deviations of the averaged CPC-data, when calculating the neutralization probability according to equation (5.3).

The original probabilities are already depicted in figure 5.5 (blue and red) and figure 5.6 (blue). However, since two measurement runs were performed the data was treated as follows: The probabilities of integer diameters were averaged, efficiencies referring to the half integer ones were just taken from the higher resolved data. Furthermore, values for α corresponding to particles of diameters smaller than 6nm are not included. The function representing the probabilities for neutral particles is not used due to its non-physical character regarding smaller particles. Therefore, $\alpha(D_p)$ for i=±1 and i=±2 are added and multiplied by the fit parameter a_0.

The theoretically computed curve (blue), which represents the sum of the charging probabilities in air, as well as the consequent fitted curve (red), valid for helium, are sketched as well. The fit parameter was found to be

$$a_0 = 1.148 \pm 0.075. \tag{5.5}$$

Both functions are drawn between 1 nm and 25 nm. Since the fitted data just covers the size range from 6 nm to 13 nm the red line is an extrapolation between 1nm and 3nm, as well as from 13 nm to 25 nm. If one certain charging probability for particles in helium α_{he} is desired, the corresponding function α_{air}, which quantifies the same efficiency in air, just needs to be multiplied by a_0:

$$\alpha_{he} = a_0 \cdot \alpha_{air} \tag{5.6}$$

In figure 5.8, this is done for particles carrying one (i=-1) or two negative charges (i=-2) in air and helium. In either case, the probability for i=-2 does not exceed 0.1%.

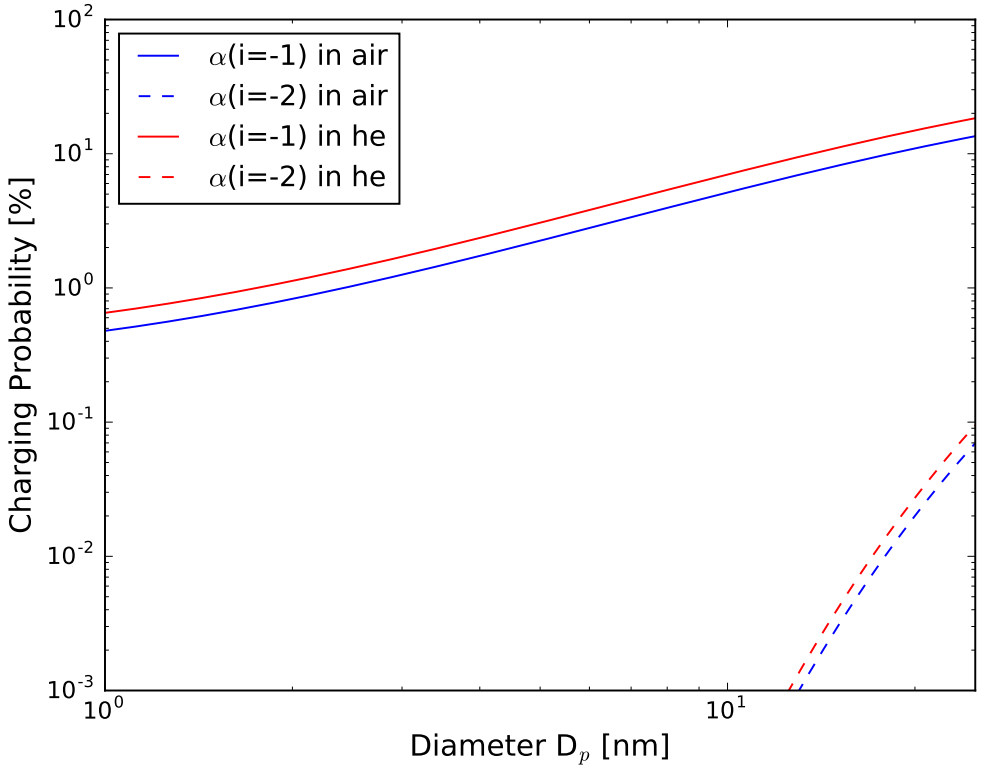

Figure 5.8: Charging probabilities for aerosol particles in air (blue) and helium (red) of diameters up to 25nm. The curves representing the latter case are achieved using equation (5.6). The solid lines mark the fraction carrying one elementary charge e, the dashed lines depict the case of doubly charged particles.

6. Characterization of Diffusional Losses and Cut-off Curves

As shown in section 3.4.1 knowledge on size-dependent diffusional sampling losses η_{diff} and activation efficiencies of CPCs η_{act} are essential for retrieval of correct concentrations, especially when observing sub-10 nm particles (see figure 3.14). Consideration of the former case is necessary in usual tubing as well as in measurement devices and attention is thus paid to the often used X-ray charger. Shortage of investigations on counting efficiencies when examining particles in helium therefore led to related experiments.

6.1 Transmission of the X-ray Charger

Exact quantification of the X-ray charger's transmission η_{char} entails the possibility of estimations on additional losses caused by other parts in the setup. This is due to the following reason: Irrespective of the analyzed instrument conventional data evaluation on diffusional losses yield an equivalent tube length, which corresponds to the same transmission. Derivation of this length is typically done by means of least mean square fitting of the experimentally determined $\eta_{diff}(D_p)$ with equations given by Gormley and Kennedy (1949).

6.1.1 Experimental Setup for Transmission Analysis

The measuring arrangement is given in figure 6.1. Nanometer-sized particles are produced using the hot-wire generator which contains a heated tungsten filament. After being charged by neutralizer 1 classification happens inside the DMA, which is kept at constant voltage for each measurement run, monodisperse particles are counted via FCE 1. Further on, the other fraction either penetrates through (investigated) neutralizer 2 and is subsequently analyzed by FCE 2, or counting happens right after the T-splitting, which connects the DMA and FCE 1. These two positions of FCE 2 thus allow measurements of losses due to the investigated X-ray charger using FCE 1 as reference. It is worth mentioning that neutralizer 2 was turned off throughout the experiment, since the FCE would otherwise fail to count particles sufficiently. The uptake of both electrometers was set to 1.5 l/min and continuously checked.

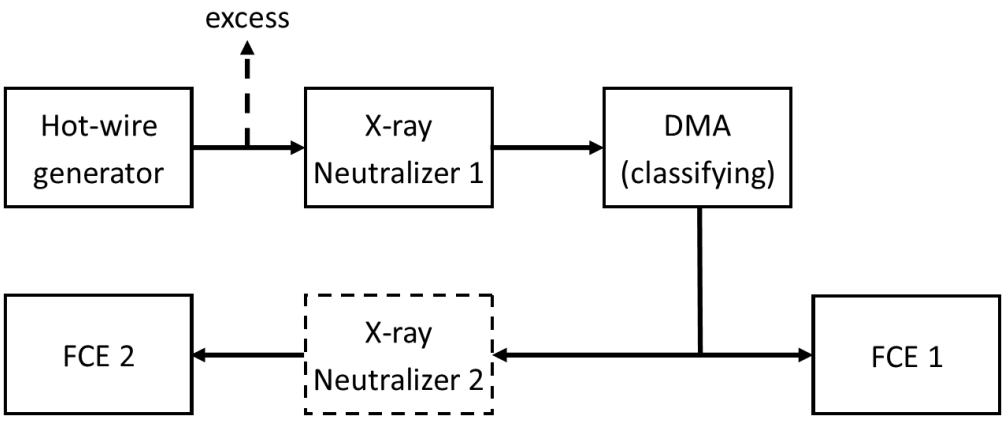

Figure 6.1: Schematic setup for analysis on the X-ray charger's size-dependent transmission efficiency η_{char}. After generation (hot-wire generator), charging (X-ray Neutralizer 1) and classification (DMA) monodisperse particles are counted by FCE 1. The remaining helium flow is either directly analyzed via FCE 2 or previously penetrates through X-ray neutralizer 2, therefore allowing calculations on η_{char}.

In order to obtain reasonable data the current of both FCEs was averaged for 1 minute, respectively, as soon as a constant particle flow was present. Thereafter, X-ray charger 2 was put between FCE 1 and FCE 2 and, as soon as stable concentrations were achieved again, the particle caused current was averaged once more. This cross-check yields two values before (I_1^{bef} and I_2^{bef}) and after (I_1^{aft} and I_2^{aft}) the exchange, respectively. Furthermore, before (after) each retrieval of $I_{1,2}^{bef}$ ($I_{1,2}^{aft}$) a background measurement of both electrometers was performed:

before charger installation:	FCE 1: I_1^{bef}	FCE 2: I_2^{bef}
after charger installation:	FCE 1: I_1^{aft}	FCE 2: I_2^{aft}

6.1.2 Results of Retrieved Transmission Efficiencies

Substituting the above quantities into equation (6.1) results in the charger's transmission efficiency η_{char} for one specific diameter:

$$\eta_{char} = \frac{I_2^{aft}}{I_1^{aft}} / \frac{I_2^{bef}}{I_1^{bef}} \tag{6.1}$$

This was done for various particle sizes in two consecutive measurement runs and constant volumetric flow rates. Mean values as well as a fitted function η_{fit} for diffusional losses (Gormley and Kennedy, 1949) are illustrated in figure 6.2. Uncertainties of each obtained transmission arise from corresponding standard deviations of all detected currents and subsequent computation of Gaussian error propagation of equation (6.1).

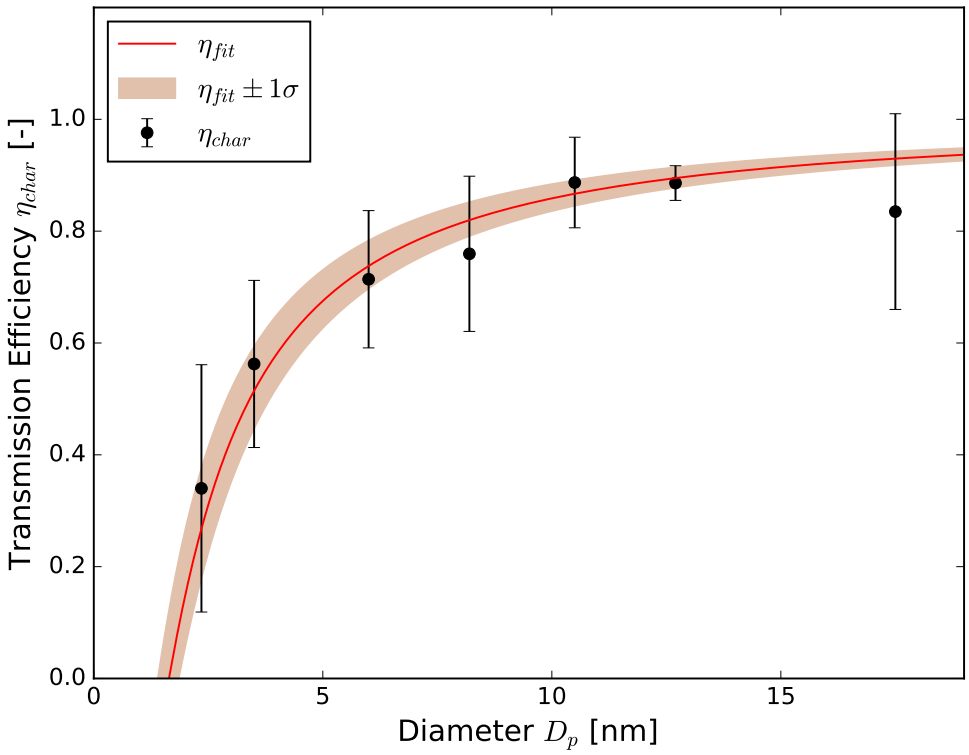

Figure 6.2: Experimentally achieved size-dependent transmission efficiencies (black) and their corresponding uncertainties of the X-ray neutralizer. Least mean square fitting of the retrieved data was done using equations given by Gormley and Kennedy (1949), thus yielding an equivalent length of (0.90 ± 0.25) m. Diffusional losses corresponding to this length (solid line) and including its standard deviations (filled area) are depicted as well.

The best fit η_{fit} was given for an equivalent length of

$$L_{char} = (0.90 \pm 0.25)\,\text{m} \tag{6.2}$$

and thus stands in contrast to calculated lengths if measurements are conducted with air, as done by Dominik Stolzenburg. These result in

$$L_{char}^{air} = (1.50 \pm 0.10)\,\text{m}. \tag{6.3}$$

The cause for this clear deviation compared to the expected value can be either practical or theoretical. First, positioning of the investigated neutralizer leads to an uptake interruption of particle-laden helium by FCE 1. Even though this case was considered and an appropriate amount of time passed until I_1^{aft} and I_2^{aft} were measured, residual air and/or contaminants in the tubing cannot be fully excluded. However, numerical approximations are based on equations which in principal solely quantify the behaviour of particles carried in air, even though corresponding carrier gas properties, i.e. mean free path λ and viscosity η, were implemented.
It is therefore very likely that application on the presented data, which is achieved when analyzing particle-laden helium, thus results in deviating equivalent lengths.

6.2 Activation of the CPC

Due to the CPC's working principle (see section 3.3.1), i.e. the condensation of vaporised working fluid on sampled aerosol particles, a cut-off diameter $D_{p,50}$ is found in the sub-10 nm range. This parameter marks the particle size, whose probabilities for successful/unsuccessful acquisition are equal. Moreover, $D_{p,50}$ is only a part of the particle material dependent cut-off curve, which provides continuous, quantitative information on each particle size's detection efficiency η_{act}.

6.2.1 Experimental Determination of Activation Efficiencies

In order to test the CPC's efficiency on analysis of small particles reference measurements via an FCE are inevitable. Both instruments and the complete measuring arrangement are given in figure 6.3. Helium penetrates through the hot-wire generator and the particle-laden flow further penetrates through an X-ray neutralizer and enters the DMA. The former yields a steady state charge equilibrium, the latter classifies particles according to their electrical mobility and thus yields a monodisperse output. The CPC's uptake of 1.5 l/min is ensured through proper orifice adjustments explained in section 3.6.1.

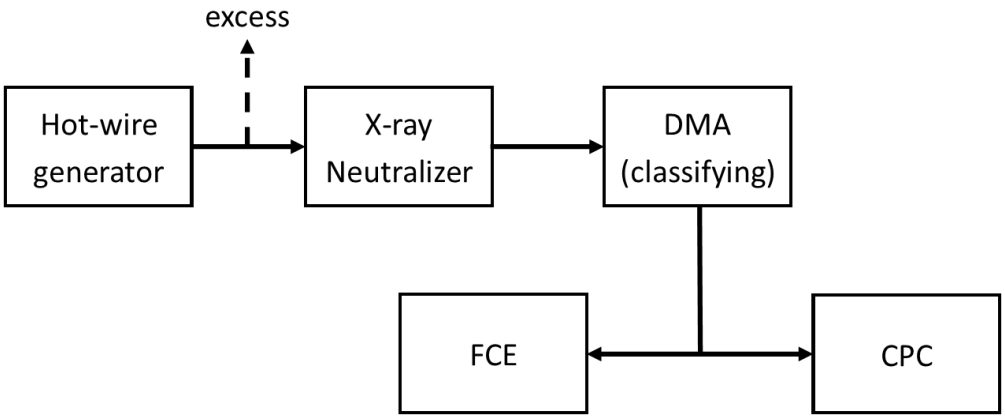

Figure 6.3: Scheme of experimental setup for retrieval of the cut-off curve of the CPC. Nanoparticles are produced in the hot-wire generator and are further on led into a charger (X-ray neutralizer) by a constant helium flow. Following this, classification (DMA) and subsequent counting of monodisperse particles (CPC and FCE) results in two obtained concentrations (N_{CPC} and N_{FCE}, respectively)

Considering the investigated size range the multiply charged fraction is negligibly small and subsequent counting by means of CPC and FCE will not be affected. The latter instrument has no lower cut-off with respect to particle sizes, since it counts the current corresponding to their carried charges. Hence, after subtraction of the respective background, conversion of this quantity into related concentrations N_{FCE} using equation (3.29) allows comparison of the CPC's obtained values N_{CPC}.
It is worth noting, that both measurement devices' uptake was set to 1.5 l/min and continuously checked for equality. This is crucial for uniform flow splitting via the T-piece before FCE and CPC, since even small flow rate anomalies lead to divergent measurement outcomes.

6.2.2 Results of Obtained Efficiencies

Two measurement runs between 2 nm and 12 nm were performed and the obtained efficiencies $\eta_{act}(D_p)$, see equation (6.4), averaged. To retrieve continuous knowledge on the CPC's cut-off curve a combination of functions, i.e. $\eta_{Gorm}(D_p)$ and $\eta_{Gomp}(D_p)$, provided by Gormley and Kennedy (1949) and Gompertz (1825), respectively, was used to approximate the data via least mean square fitting. This results in $\eta_{fit}(D_p)$, see equation (6.5), which allows the best approach to $\eta_{act}(D_p)$ and additionally accounts for diffusional losses in CPC tubing. Parameters depicted in square brackets are fitting coefficients of its respective function.

$$\eta_{act}(D_p) = \frac{N_{CPC}(D_p)}{N_{FCE}(D_p)} \tag{6.4}$$

$$\eta_{fit}(D_p) = \eta_{Gorm,[b,c]}(D_p) \cdot \eta_{Gomp,[L_{act}]}(D_p) \tag{6.5}$$

where

$$\eta_{Gomp,[b,c]}(D_p) = a \cdot e^{-b \cdot e^{-c \cdot D_p}} = 1 \cdot e^{-b \cdot e^{-c \cdot D_p}} \tag{6.6}$$

The latter equation is adapted and parameter a was set to 1, since the fit function otherwise would slightly exceed 1, which is non-physical.

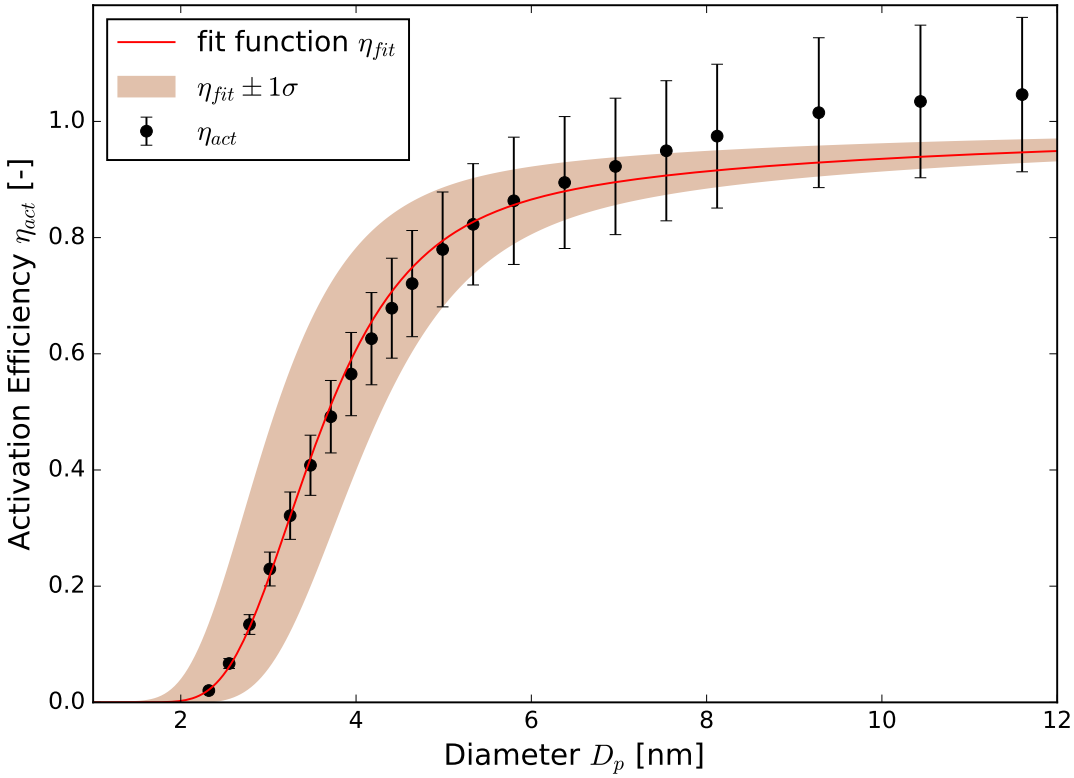

Figure 6.4: Obtained size-dependent activation efficiencies (black) and corresponding uncertainties of the CPC. Least mean square fit using modified equations of Gormley and Kennedy (1949) and Gompertz (1825) yield η_{fit} (solid line) and its standard deviation (filled area). The retrieved fitting parameters are b=(106±31), c=(1.49±0.14) and L_{act}=(0.26 ± 0.14) m. The cut-off diameter was found to be $D_{p,50}$= (3.68±0.60)nm.

The averaged obtained activation efficiencies $\eta_{act}(D_p)$ (black) as well as the fit-function $\eta_{fit}(D_p)$ (red line) and its corresponding standard deviation (red area) are given in figure 6.4. The error bars for each data point arise from Gaussian error propagation computations of equation (6.4). Comparison of $\eta_{act}(D_p)$ and $\eta_{fit}(D_p)$ shows good coincidence and the fitted parameters are as follows:

$$\begin{aligned} b &= 106 \pm 31 \\ c &= 1.49 \pm 0.14 \\ L_{act} &= (0.26 \pm 0.14)\,\text{m} \\ D_{p,50} &= (3.68 \pm 0.60)\,\text{nm} \end{aligned} \tag{6.7}$$

The computed cut-off diameter agrees well with the one provided by Hermann et al. (2007). This leads to the conclusion that the adjusted settings of condenser (T_C=15 °C), saturator (T_S=35 °C) and optics temperature (T_O=40 °C) are suitable when studying helium-carried particles. This set was found through stepwise reduction of T_C and T_S, until no homogenous nucleation of the working fluid, and hence no erratic particle counting, inside the CPC was measured.
It is also notable, that the error bars' sizes increase for higher particle diameters, which is primarily due to higher concentrations (and thus uncertainties) obtained by the CPC. This elevated signal hardly arises due to enhanced η_{act}, but mainly originates from the hot-wire generator's output, i.e. concentrations of particles $>$5 nm are considerably larger than for smaller ones. Subsequent error computations result in heightened error bars and broadening of the fit function's standard deviation.

7. Computation of the Number Size Distribution

Theoretical equations on correct computation of size distributions $d\mathrm{N}/d\ln D_p$, see chapter 3.4, as well as therein comprised instrument characteristics, see chapters 3.5, 4 and 6, allow concluding application on exemplary raw data. Furthermore, discussions on the resulting $d\mathrm{N}/d\ln D_p$ as well as the contributive low/high impact of all found parameters and their uncertainties are possible. The significance of these parameters is again outlined and further on illustrated in the following section.

7.1 Review of Instrument Characterization Parameters

For the sake of clarity a summary of all fitted quantities is given in table 7.1, which further states both, the dedicating chapter and thus characterized instruments. It is noteworthy, that all values below were retrieved after multiplying all particle diameters D_p by the magnification factor M_D.

chapter 4	DMA classification length	L_{he}=(15.9 ± 5.2) mm
	Correction factor for particle diameters	M_D=1.16±0.18
chapter 5	Multiplying factor for charging efficiency functions given by Wiedensohler (1988)	a_0 = 1.148 ± 0.075
chapter 6	Equivalent Charger length for diffusional losses	L_{char}=(0.90 ± 0.25) m
	Equivalent CPC length for diffusional losses	L_{act}=(0.26 ± 0.14) m
	Fit parameter for the adapted Gompertz-function	b = 106 ± 31
	Fit parameter for the adapted Gompertz-function	c = 1.49 ± 0.14

Tabelle 7.1: Summary of all fitted parameters which are implemented in further equations for retrieval of the size distribution

For the purpose of clear comprehension, the impact of all parameters on corresponding diffusional losses (L_{act} and L_{char}), charging efficiency (a_0), activation efficiency (b and c) and particle diameter correction (D_p) are illustrated in figures 7.1, 7.2 and 7.3.

Figure 7.1 depicts the efficiencies of the X-ray neutralizer's charging (yellow line) and its transmission (blue line) as well as the CPC's activation and transmission (red) with respect to the corresponding particle diameters D_p, as well as all corresponding standard deviations (hatched areas of same colours as lines). The product of all efficiencies η_{tot} (black line) approaches the charging efficiency for increasing D_p since both other curves converge to 1. Uncertainties of η_{tot} arise from all other deviations and show strong decrease with increasing particle diameters. For instance, relative values of standard deviations and absolute values ($\Delta\eta_{tot} : \eta_{tot}$) are below 10% for D_p >4.5 nm.

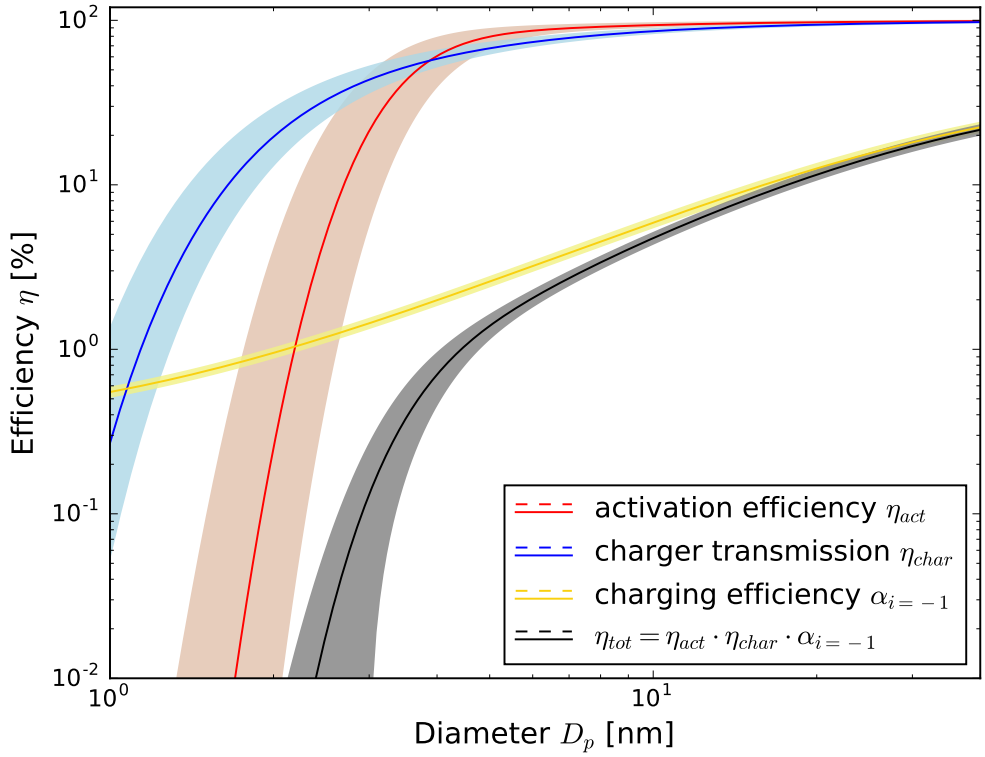

Figure 7.1: Efficiencies of activation and penetration of the CPC η_{act} (red line), transmission η_{char} of the X-ray charger (blue), corresponding particle charging $\alpha_{i=-1}$ (yellow line), as well as the total product η_{tot} of all quantities (black). Standard deviations are expressed as hatched areas of the same colour, respectively.

Figure 7.2 entails the same efficiencies as before (solid lines) and additionally provides information on these functions' progress if computed without inclusion of the particle diameter magnification factor M_D (dashed lines). Hatched areas again represent related standard deviations. It is evident, that due to M_D all curves acquire a shift with respect to the abscissa and deviations between one set of dashed/solid lines above 10 nm are only higher than 10% for charging efficiencies. However, consideration of particular errors shows an overlap of η_{char} and η_{act} throughout the whole size range, respectively. A split of both η_{tot} functions' hatched areas, and hence significant distinction, is observable at 4 nm.

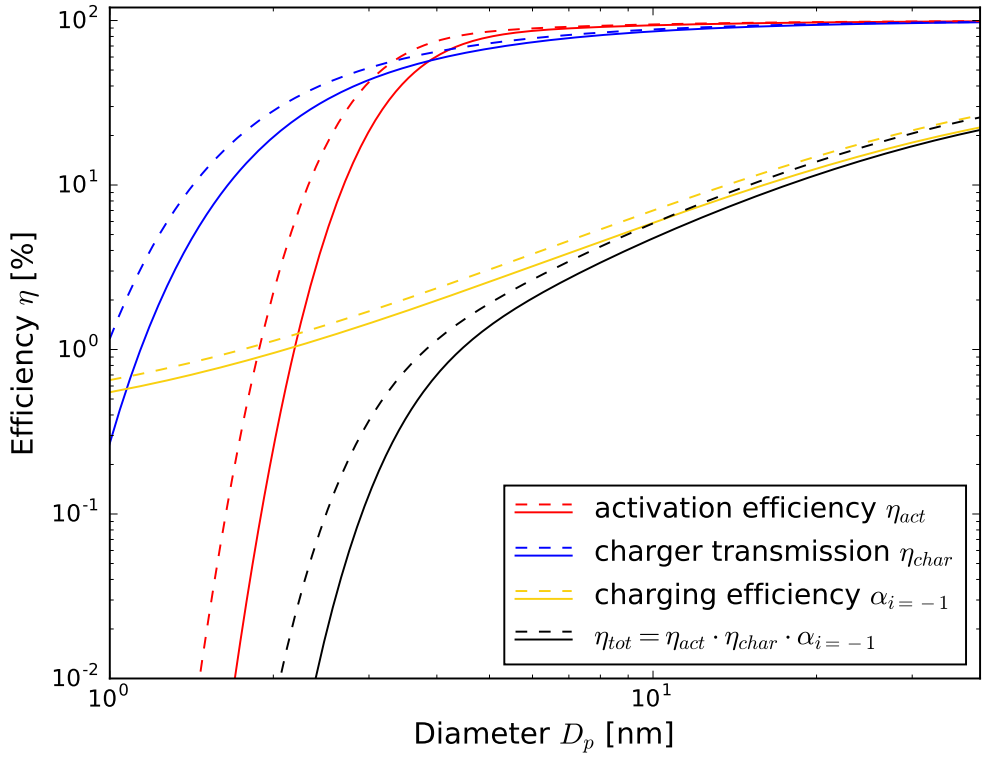

Figure 7.2: Efficiencies of activation and penetration of the CPC η_{act} (red lines), transmission η_{char} of the X-ray charger (blue lines), corresponding particle charging $\alpha_{i=-1}$ (yellow lines), as well as the total product η_{tot} of all quantities (black line). All curves were computed including/excluding particle size correction (solid/dashed line). Standard deviations are again expressed as hatched areas of the same colour. Significant distinction of one set of lines is only possible for charging probabilities (complete size range) and the total product below 4 nm.

Figure 7.3 provides additional information on all above-mentioned size dependent efficiencies. Each quantity is illustrated by means of three lines, which represent previous particle size corrected and -dependent values (solid line), as well as the corresponding outcome if implementing the multiplier's M_D lower/upper bound (0.98 and 1.34), which determine its uncertainty (dotted lines). Considering standard deviations (hatched areas of the same colour) allows the following conclusions:

- Including uncertainties of M_D as well as corresponding errors of η_{act} and η_{char} results in vast inaccuracies for smaller particles. The assumption of lower/upper limits ($\pm\Delta\eta_{act}$ and $\pm\Delta\eta_{char}$) to be determined by smallest/highest deviations of the inferior/posterior dotted lines results in relative values ($\Delta\eta_{act}/\eta_{act}$ and $\Delta\eta_{char}/\eta_{char}$) lower than 10% for particles exceeding sizes of 6.6 nm and 7 nm, respectively.
- Even though uncertainty intervals of $\alpha_{i=-1}$ and η_{tot} (partially) do not overlap the outer error limits ($\pm\Delta\alpha_{i=-1}$ and $\pm\Delta\eta_{tot}$) should be taken into account. Relative uncertainties for charging efficiency ($\Delta\alpha_{i=-1}/\alpha_{i=-1}$) occur between 17% and 25%. Corresponding values of the total product ($\Delta\eta_{tot}/\eta_{tot}$) are below 40%, 30% and 20% for particles larger than 6 nm, 10 nm and 30 nm, respectively.

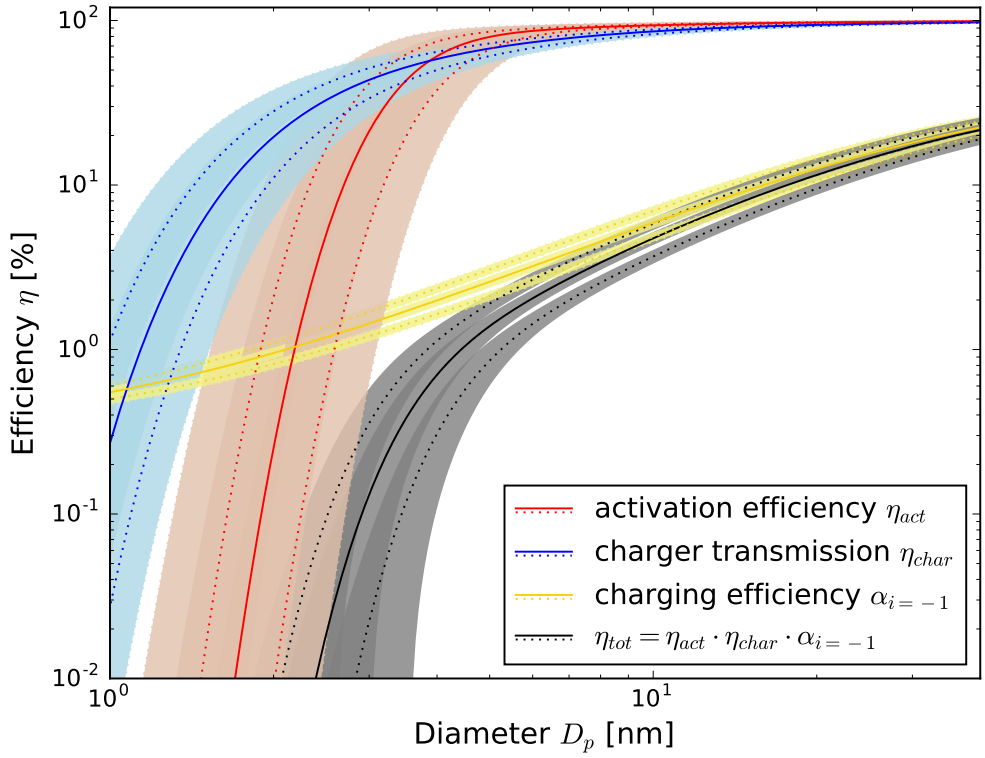

Figure 7.3: Particle size D_p dependent efficiencies of activation (red) and charger transmission (blue), as well as charging efficiency (yellow) and the product of all aforementioned quantities (black). Solid lines illustrate the result when considering the average value of M_D =(1.16± 0.18), dotted lines those when implementing its upper/lower boundary, i.e. 0.98 and 1.34.

An overview of all these relative values of all efficiencies with respect to particle diameters D_p is given in figure 7.4. Therein, dashed lines are valid if no particle size correction and hence no further error are considered, inclusion of M_D and ΔM_D yields solid lines of the same colour. Relative errors $\Delta\eta_{tot}/\eta_{tot}$ (black) converge to those lines indicating $\Delta\alpha_{i=-1}/\alpha_{i=-1}$ for higher particle diameters, which is the reason for the slow decrease of the solid black line. All errors acquire significant shifts upwards and consequently approach lower values at higher particle diameters. This is emphasized by means of four different shades of grey, which represent equivalent percentages of relative aberration (10%, 20%, 30% and 40%).
Retrieved knowledge on total transmission and its uncertainty is inevitable for computations of size distributions, whose numerical conduction with typical experimental data is explained in the following section.

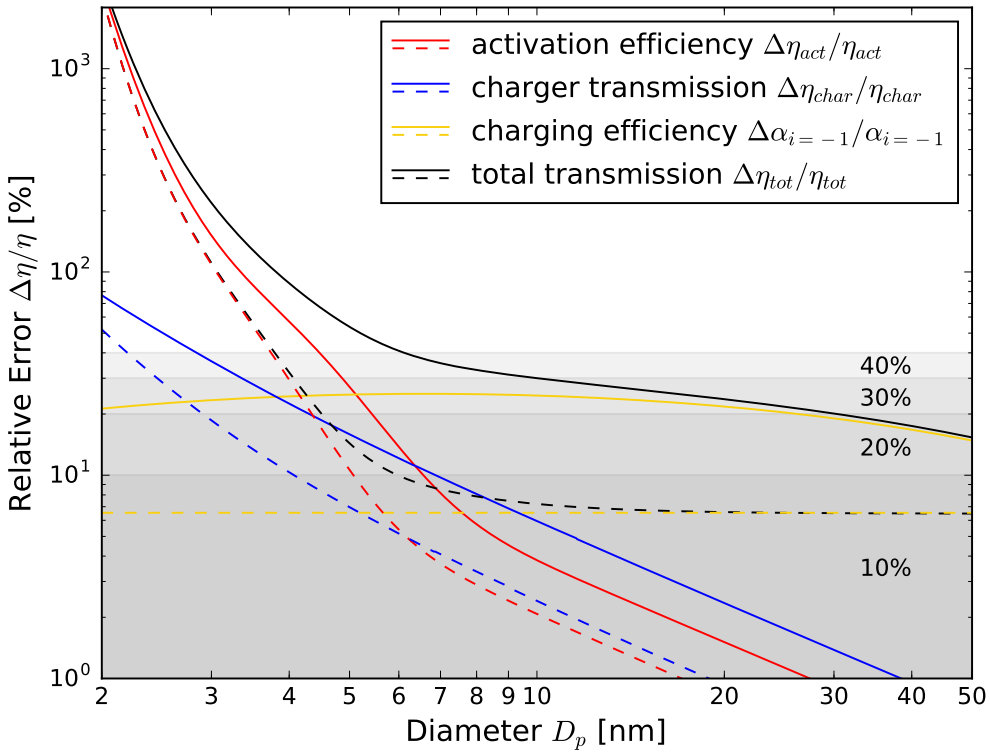

Figure 7.4: Particle size D_p dependent relative Errors of all efficiencies, i.e. activation $\pm\Delta\eta_{act}$ (red), transmission $\Delta\eta_{char}/\eta_{char}$ (blue), charging $\Delta\alpha_{i=-1}/\alpha_{i=-1}$ (yellow) as well as corresponding values $\Delta\eta_{tot}/\eta_{tot}$for the product of all quantities (black). Solid lines indicate resulting values when considering particle size corrections via M_D. Dashed lines illustrate the corresponding outcome for non-corrected data. Different colour gradation visualizes equivalent relative aberrations of standard deviation against efficiency magnitude (10%, 20%, 30% and 40%).

7.2 Review and Application of Essential Equations

Equations (7.1) and (7.2) have already been discussed in chapter 3.4.2, but are repeated below as well since subsequent adaptations are necessary. Following this, an exemplary size distribution, including all corrections, deviations and modifications is provided and explained.

$$\frac{1}{2}V_{max} < V < V_{max}: \quad N_0(D_{p,1}) = \frac{dN}{d\ lnD_{p,1}} \cdot \alpha(D_{p,1}, i=1) \cdot \beta \cdot \Psi(D_{p,1}) \cdot \eta_{diff}(D_{p,1}) \cdot \eta_{act}(D_{p,1}) \tag{7.1}$$

$$\begin{aligned}\frac{1}{3}V_{max} < V < \frac{1}{2}V_{max}: \quad N_0(D_{p,2}) = &\frac{dN}{d\ lnD_{p,2}} \cdot \alpha(D_{p,2}, i=1) \cdot \beta \cdot \Psi(D_{p,2}) \cdot \eta_{diff}(D_{p,2}) \cdot \eta_{act}(D_{p,2}) + \\ &\frac{dN}{d\ lnD_{p,1}} \cdot \alpha(D_{p,1}, i=2) \cdot \beta \cdot \Psi(D_{p,1}) \cdot \eta_{diff}(D_{p,1}) \cdot \eta_{act}(D_{p,1})\end{aligned} \tag{7.2}$$

In order to compute the final size distribution, these equations are rearranged so that $\frac{dN}{d\ lnD_{p,1}}$ and $\frac{dN}{d\ lnD_{p,2}}$ are calculated, respectively. Additional modifications or implementations were conducted as well:

- η_{diff} is the product of all particle loss rates due to utilized instruments, see equation (7.3). Therein comprised equivalent lengths L_{act}, L_{char} and L_{DMA} account for losses in the CPC, X-ray charger and DMA, respectively:

$$\eta_{diff} = \eta(L_{act}) \cdot \eta(L_{char}) \cdot \eta(L_{DMA}) \tag{7.3}$$

- Corrections for triply charged particles were not considered, which has two reasons: First, no essential quantitative information on corresponding charging probabilities were achieved. Second, their contribution to obtained concentrations is insignificant, which is shown later. Equation (7.2) was thus assumed to hold true for all voltages lower than $\frac{1}{3}V_{max}$ as well.
- DMA voltages below $\frac{1}{2}V_{max}$ not always exactly equal half the magnitude of previously applied values. Information on diameters and concentrations of doubly charged particles found below $\frac{1}{2}V_{max}$ is thus not instantly known. This is why lognormal V-dependent fits for $\frac{dN}{d\ lnD_p}$ and D_p were performed using known (adjacent) values.

Utilization of the above equations yields size distributions presented in figure 7.5. The green dots depict concentrations computed via equations 7.1 (between V_{max} and $\frac{1}{2}V_{max}$) and 7.2 (between $\frac{1}{2}V_{max}$ and V_{min}), which includes corrections for doubly charged particles. Corresponding non-corrected $\frac{dN}{d\ lnD_p}$ are illustrated as red dots. Furthermore, standard deviations of the latter concentrations are displayed as well (red hatched area).

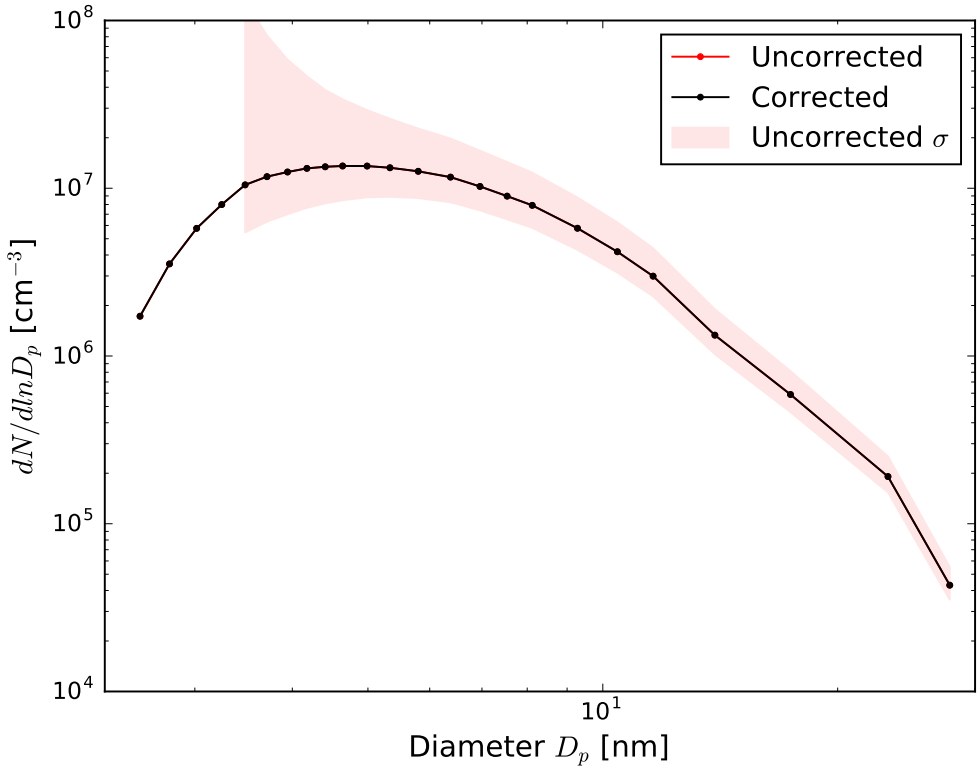

Figure 7.5: Computed size distributions of tungsten aerosol particles with (red) and without (black) consideration of doubly charged particles. The latter is found within the former's standard deviation (red hatched area) throughout the whole size range. Furthermore, no visible difference between the given distributions is present. Corrections attributed to particles carrying two charges thus scarcely show an effect.

It is obvious, that doubly charged particle corrected concentrations are within uncertainties of related non-corrected ones for the complete illustrated size range. Considering this, computation of the former concentrations has to be treated with care. The main reason for these vast uncertainties is the enhanced error when correcting particles for their diameter D_p, i.e. multiplication of the magnification factor M_D=(1.16±0.18). In order to acquire knowledge on its effect on size distribution calculations the same measurement outcome as given in figure 7.5 was analyzed without inclusion of M_D.

Resulting concentrations are displayed in figure 7.6, which comprises previous data as well. Novel information, i.e. size distributions which include/exclude corrections for doubly charged particles, are illustrated as green and red lines, respectively. It is worth noting, that all fitted parameters, e.g. for CPC activation, X-ray charger transmission, etc., change with respect to (non) considered M_D and thus yield a different set, which of course is implemented in the line plots. Again, standard deviations for all obtained concentrations are depicted hatched areas (grey). Explicit distinction between two deviation intervals is only valid for higher D_p, however, an overlap for smaller particles ($\simeq$ 10 nm) is only due to increasing deviations of M_D-corrected concentrations. The broadening gap towards lower D_p is thus not negligible.

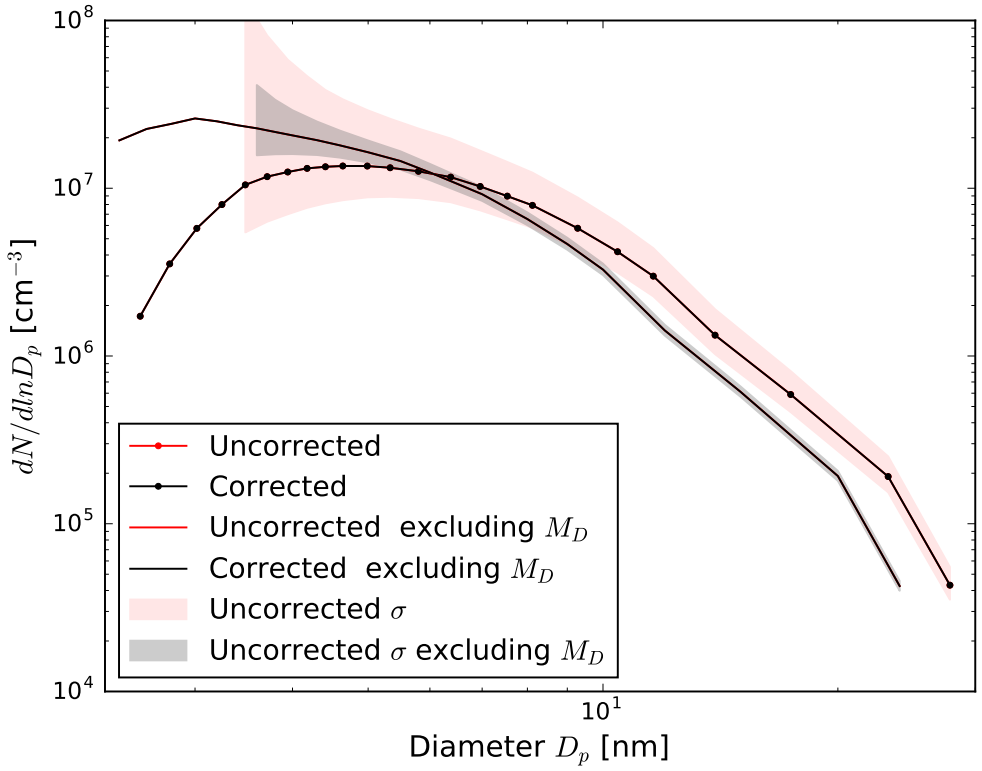

Figure 7.6: Computed size distributions of tungsten aerosol particles with (red) and without (black) consideration of doubly charged particles as well as including (dots) and excluding (lines) DMA calibration. An overlap of both standard deviations (red and grey hatched area, respectively) is present below 10 nm. Furthermore, no siginificant gap, caused by corrections for doubly charged particle fraction, between corresponding concentrations (lines and dots, respectively) is present. Red dots and lines are thus behind the black counterparts, and hence not visible.

Both size distributions show no change if corrected for a doubly charged fraction, even though high particle concentrations are present. This circumstance is due to low corresponding probabilities and resulting differences are only noticeable for particles of exceeding diameters. In order to clarify the importance of related corrections at larger scales analysis of tungsten particles was further conducted utilizing a larger DMA. Equal flows (Q_{sh} and Q_{ex}) and the same setup were used as before. However, this DMA was not calibrated with PSL spheres, which is why the same value for M_D was used. This implies an unknown error, and resulting size distributions should thus be treated with care, see figure 7.7.

Again, lines depict concentrations if disregarding particle size corrections, dots represent corresponding values if including M_D. Corrections for doubly charged particles (black) are now evident, since non-corrected lines/dots (red) clearly deviate to each other. Nevertheless, black and red line pairs are within the other's related standard deviations for all particle diameters. It should be also noted that no correction for doubly charged particles at the three largest sizes exists. Corresponding values, however, would scarcely have significant impact due to the sharp concentration decrease in this size range.

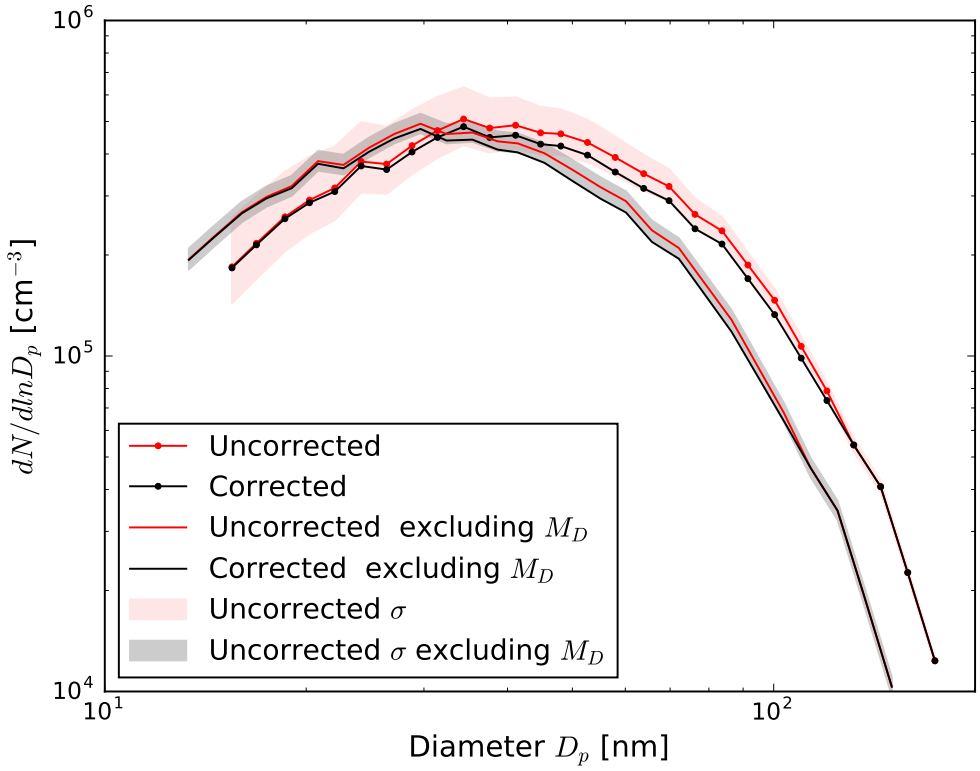

Figure 7.7: Computed size distributions of tungsten aerosol particles with (red) and without (black) consideration of doubly charged particles as well as including (dots) and excluding (lines) calibration parameter M_D (only valid for the small DMA). An overlap of both standard deviations (red and grey hatched area, respectively) is present above 50 nm, however, an unknown error of M_D when applied on nominal diameters of the utilized long DMA is not considered in the above distributions. The lack of doubly charged corrections at larger sizes can be neglected due to the sharp concentration drop.

Part II

Comparative Experiments of DMA-Train and Nano-SMPS

8. Intercomparison Between the nano-SMPS and the DMA-Train

Knowledge of aerosol particle size-distribution has become inevitable if analysis on complex aerosol dynamics is carried out (Kulmala et al., 2013). Closer insight on nucleation- and NPF-processes in particular necessitates high-time-resolution investigations of sub-10 nm particles (McMurry et al., 2000), which is due to fast initial and subsequent growth (Kulmala et al., 2004) as well as non-negligible coagulation losses (Lehtinen et al., 2007). Further consideration calls for continuous and high-time-resolved size-distributions, starting at 1...2 nm.
This information is achieved by combination of the DMA-train (Stolzenburg et al., 2017) and a nano-SMPS (Wang and Flagan, 1990). The latter approximately covers size ranges from $\sim$10 nm to 65 nm, the first obtains concentrations of particle sizes between $\sim$2 nm and 10 nm. Furthermore, they are both intensively used in the CLOUD-experiment (see section 2.2). The second-mentioned instrument is well-established and consists of a DMA and a CPC. With this method the applied DMA-voltage V is continuously scanned, thus allowing fast particle size scans. On the other hand, the DMA-train's operating principle uses fixed voltages in various channels (Stolzenburg et al., 2017) which is briefly discussed in the following section. After this, conventional analysis of particle growth and comparative experiments regarding DMA-train and nano-SMPS are outlined.

8.1 Operating Principle of the DMA-train

The DMA-train comprises 6 Vienna-type DMAs (Grimm S-DMA), each of them operating at fixed voltages and hence mobility equivalent particle diameters, and 6 consecutive particle counters, which are all working parallel and draw their corresponding sample flow from one common inlet. This initial intake is split into two further flows, which both are penetrating through X-ray chargers (Advanced Aerosol Neutralizer, TSI 3088), by which means steady-state charging probabilities of the sampled aerosol particles are achieved. Following this, the two flows are divided into three sub-flows, respectively, which subsequently enter the DMAs and CPCs.
The DMA-train's setup is given in figure 8.1, which was taken from Stolzenburg et al. (2017). In addition the scheme shows the different types of the operating particle counters, these are ultrafine CPCs (UCPC, TSI 3776), particle size magnifiers (PSM, Airmodus A10), and a nano water-based CPC (N-WCPC, TSI 3788) .

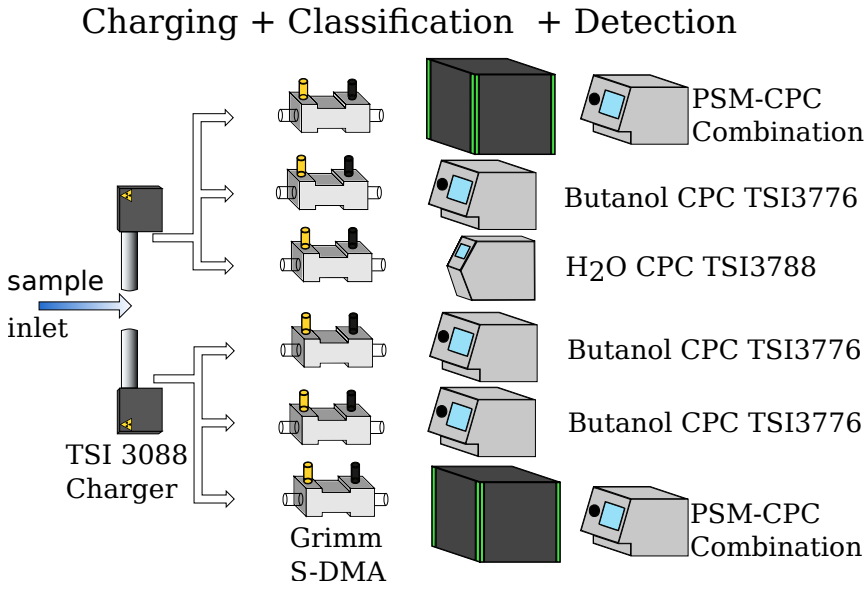

Figure 8.1: Schematic setup of the DMA-train taken from Stolzenburg et al. (2017). Two chargers provide steady state charging probabilities of the drawn aerosol. Six parallel-operating DMAs at different, but fixed voltages classify the sampled particles according to their electrical mobility, subsequently the corresponding concentrations are obtained by means of diverse particle counters.

The explained experimental configuration entails two main advantages compared to the nano-SMPS or similar instruments: Firstly, the DMA-train provides size-dependent concentrations every second, whereas SMPS systems require ∼50 s for each measurement run. As a result improved statistics for further calculus are obtained. Secondly, the sampled particles are all in the size range of 1 nm to 10 nm, and thus below the SMPS' detection limit.
As already mentioned, both instruments yield continuous and time- resolved information on size-dependent particle concentrations, and thus -growth, which is why they are used in parallel at the CLOUD-campaign. The corresponding growth rates (GR) are usually calculated for suitable size ranges, i.e. where a linear correlation of the so-called appearance times is given. Additional information is given in the next section.

8.2 Introduction to the Calculus of Particle Growth Rates

Various procedures aiming for computations of nano-particle growth rates exist, for example the maximum-concentration method and the log-normal distribution function method (Kulmala et al., 2012), or the appearance time method (Lehtipalo et al., 2014). In the following, the latter will be discussed more detailed, since it is utilized in the analysis of the data achieved by the DMA-train as well.

Different procedures of the appearance time method exist. One possible way is based on using total concentrations obtained by particle counters, e.g. CPC or PSMs, with different cut-off diameters $D_{p,50}$. The points of time, when 5% of the maximum total concentrations are detected, determine the corresponding appearance times of the respective $D_{p,50}$. However, the DMA-train continuously counts classified particles of six invariable diameters. Therefore, the six related concentrations are used in order to estimate the corresponding appearance times. These are again equal to the points of time, when 50% of the particular total concentrations are present. Computations are done by means of equation (8.1), which approximates the time-resolved particle concentration $N(t)$ by means of least-mean-square - fitting.

$$N(t) = \frac{a-b}{1+(t/c)^d} + b \tag{8.1}$$

The parameters a and b equal the minimum and maximum of this sigmoid function, respectively, whereas d determines the function's curvature. The appearance time and its uncertainty are immediately achieved since they equal c and its standard deviation.
Further calculus is done as follows: The determined appearance times are plotted against the corresponding diameters and subsequently linear interpolations are performed in favoured size ranges. Thus obtained slopes equal the growth rates (usually indicated in nm/h), which are valid in the chosen size ranges. Additional information is given in (Lehtipalo et al., 2014).

8.3 Intercomparison Experiments

A qualitative difference of obtained size-resolved number concentrations is already provided by Stolzenburg et al. (2017). Therein, the high time-resolution of the DMA-train compared to the nano-SMPS is emphasized by analysis of size-increasing tungsten oxide particles. In the following, even deeper insight and experimental comparison of both instruments, when operating in parallel, is provided.
When combining the evolution of the size-distributions, and taking all factors from section 3.4.1 into account, the resulting propagation of size-dependent concentrations equals the one depicted in figure 8.2. A small deviation of concentrations at 8 nm, i.e. the overlapping size region between DMA-train and nano-SMPS, is evident. Therefore, DMA-train or the nano-SMPS either over- or underestimate the correct number concentrations, respectively. Closer analysis of the time-evolving tungsten oxide nanoparticles' spectrum is thus conducted in four periods of time. Within these sections all concentrations obtained with both, nano-SMPS and DMA-train, are averaged and subsequently relative values calculated.

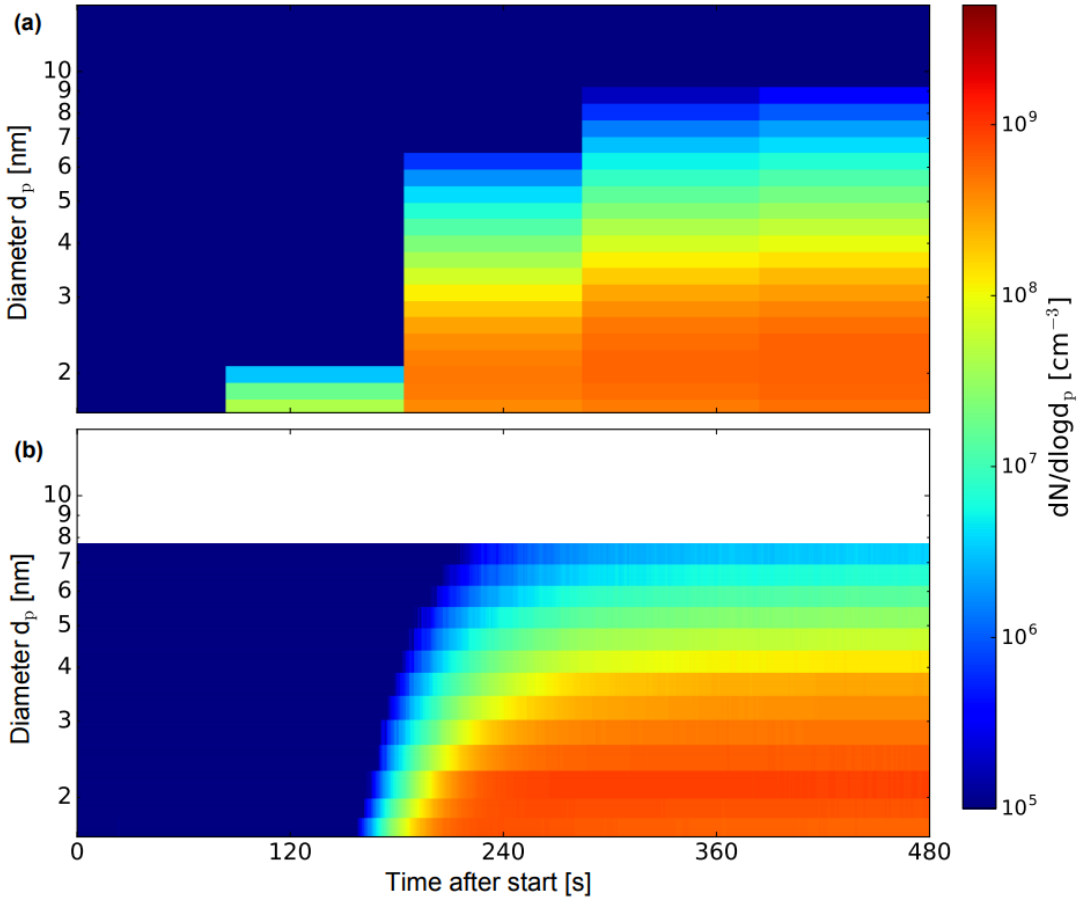

Figure 8.2: Time-evolving concentrations of size-increasing tungsten oxide particles between 2 nm and 10 nm obtained with the DMA-train and the nano-SMPS, respectively. The former clearly shows the size distribution's propagation towards larger particle sizes in very high temporal resolution if compared to the latter. Closer inspection of respective concentrations at 8 nm reveals a non satisfying gap.

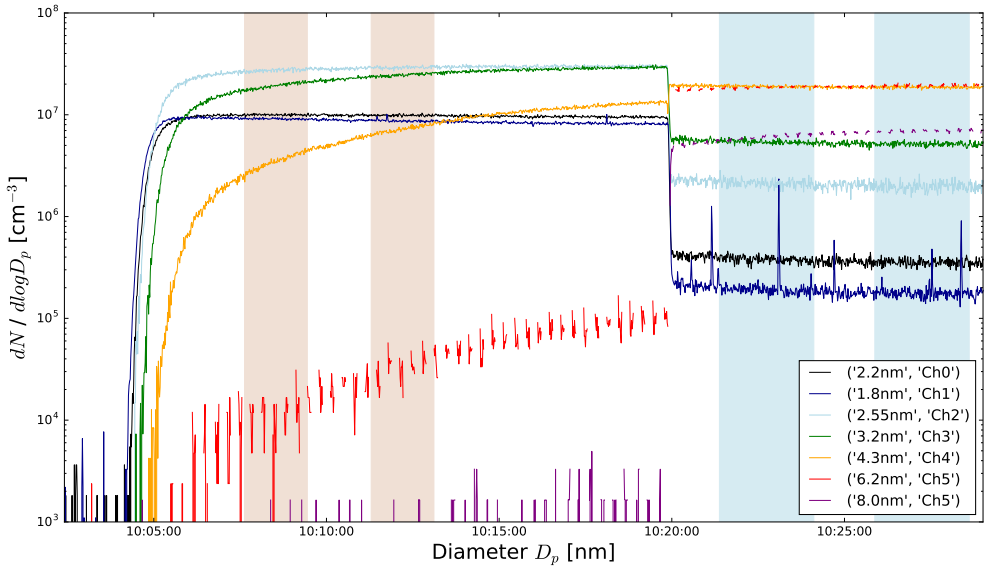

Figure 8.3: Time-evolving concentrations of particles between 1.8 nm and 8.2 nm obtained with the DMA-train. Two sets of hatched ranges (red and blue) illustrate intervals, which were selected for closer analysis and comparison of corresponding nano-SMPS data. Concentrations of particles larger than 2.2 nm are still rising in the first two segments (red), however, no considerable changes are present in the latter sections (blue) for all analyzed particle sizes.

Figure 8.3 shows the DMA-train's time-propagating concentrations for particles in various sizes between 1.8 nm and 8 nm, as well as the examined time zones, which are depicted as red and blue hatched areas. During the first two periods of time (red) the tungsten-oxide generator was still warming up, which is why concentrations of larger particles did not yet achieve constant values. The second set of time zones (blue), however, allows the analysis of constant spectra. The former set of concentration ratios (DMA-train / nano-SMPS) was averaged during 2 nano-SMPS runs (110 seconds), the latter one for 3 corresponding cycles (165 seconds). It is worth noting, that the concentration jumps around 10:20 are the result of adapted temperature settings at the WO_x-generator.

All acquired relative values are given in figure 8.4, wherein the former set is illustrated as red and orange, the latter as blue and green points with respect to particle diameters D_p. Two things are evident: Considering constant spectra, the DMA train obtains higher concentrations for smaller particles, however, this enhanced signal decreases for increasing D_p and approaches the one achieved by the nano-SMPS. On the contrary, time evolving spectra show that the DMA-train still acquires exceeding $dN/dlogD_p$ compared to the nano-SMPS of particles smaller than 5 nm. Above this size, however, the latter shows enhanced concentrations, which is why relative values are between 0.1 and 0.2 at 8 nm. This non-satisfying huge gap stands in sharp contrast to the expectation of quotients close to 1, since size-dependent correction factors and thus uncertainties decrease for particles of larger diameters.

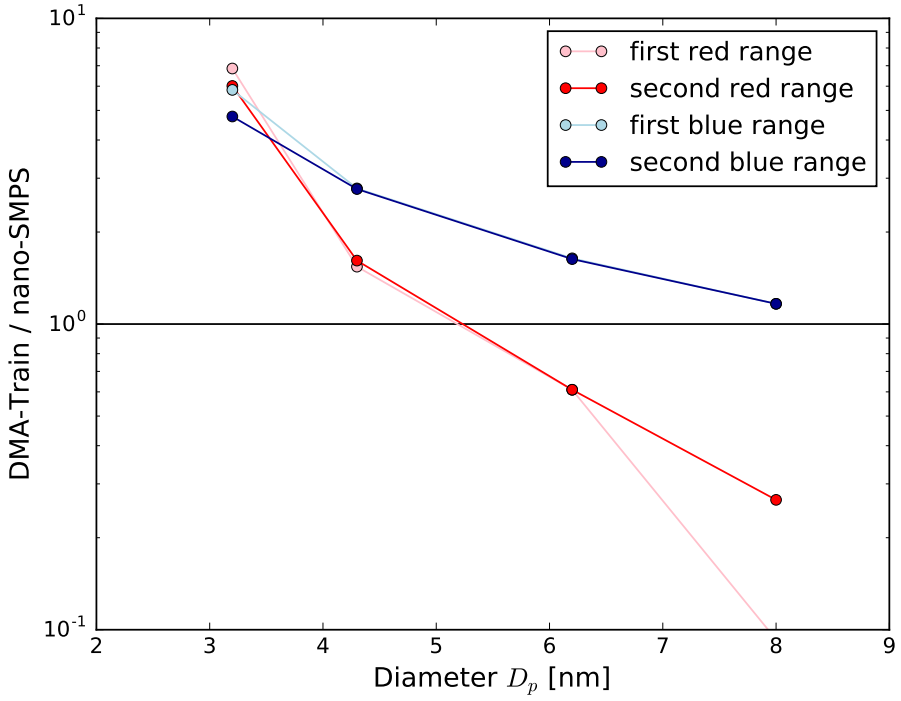

Figure 8.4: Relative values of size dependent particle concentrations obtained with the DMA-train and the nano-SMPS. (Light) red dots and lines result from the first two red stages, (light) blue markers represent corresponding values in blue time intervals in figure 8.3. It is evident, that retrieved concentrations approach each other with respect to increasing particle diameters if no considerable changes in spectra are observable (blue). Related outcomes for non-constant concentrations, however, drastically decrease if concentrations are still increasing during measurement evaluations. According relative values fall below 1 (solid, black line) for particles between 5 nm to 5.5 nm and even drop below 0.1 at 8 nm.

Comparison of maximum concentrations ($10^7\,cm^{-3}$) present in the previous experiment when tungsten oxide particles were analyzed and prevailing values in the CLOUD-chamber during a nucleation event shows, that the former exceeds the latter by a factor of 100 to 1000. Furthermore, corresponding growth rates and chemical compositions are different. In order to test the sensitivities of both instruments for lower particle concentrations a typical measurement run of the CLOUD11 campaign was analyzed. Related time-propagating and size-dependent concentrations (colour-coded) obtained with the nano-SMPS are displayed in figure 8.5. Values within grey, hatched areas were averaged and compared with corresponding DMA-train data, respectively. Corresponding relative values are depicted in figure 8.6.

Considering the first two segments (black and grey) it is evident, that concentrations of particles with diameters of 4.3 nm obtained with the DMA-train exceed those retrieved by the nano-SMPS by a factor of 2.68 and 3.34, respectively. Disregarding the fifth comparing run (dark green), all other results at the mentioned size are between 0.85 and 1.61. The first-mentioned outlier might be attributed to the provided statistics' deficiency if averaging an insufficient number of nano-SMPS runs: During the composing seven cycles scarce numbers of particles were detected in this small size range, whereas in the following set (sixth run, light green) high concentrations were obtained. These exceeding values are additionally apparent from figure 8.5, wherein one size bin shows no concentration at all (fifth hatched area), however, the subsequent interval indicates (relatively) high particle numbers.

Relative values of larger particles (6.2 nm and 8 nm, respectively) show decrease in both, scatter and average value. Both might be attributed to the instruments' higher sensitivity and thus less necessity for computations aiming for concentration corrections (see section 3.4.2).

Overall, retrieved concentrations of the DMA-train exceed those obtained with the nano-SMPS by a factor of 2.05, 1.56 and 1.16 for particle diameters of 4.3 nm, 6.2 nm and 8 nm, respectively. Utilization of the latter instrument provided no information on particles smaller than 4.3 nm due to its minor sensitivity. Again, this circumstance highlights the benefit of applying the DMA-train for measurements on systems such as the CLOUD-chamber, wherein lower particle numbers are pre-dominant, however, high-time resolution of according concentrations are of interest.

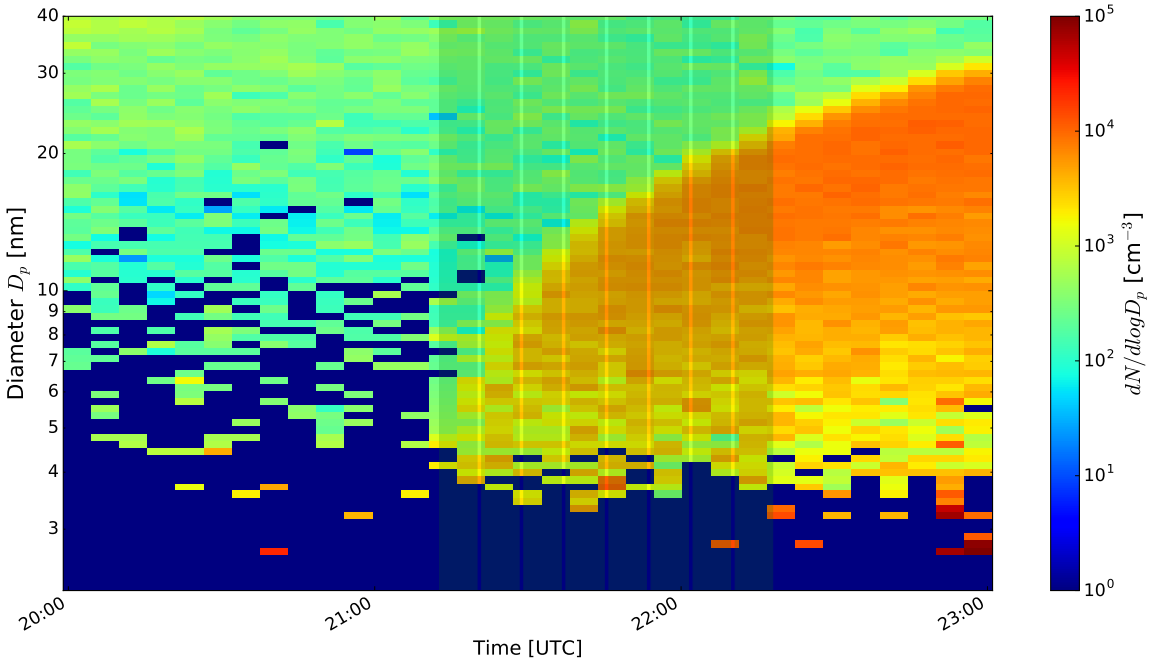

Figure 8.5: Evolution of size-dependent particle concentrations during a typical CLOUD11 measurement run. The abscissa denotes the current time, whereas the ordinate states the particle diameters. Corresponding concentrations are illustrated as colour-coded boxes, whose length imply the averaging time period, i.e. 4.5 minutes in this case. Formation of particles due to vapor uptake during the depicted two hours is evident, since concentrations increase for particles between 20 nm and 40 nm. Values comprised in grey, hatched areas were averaged and compared with those obtained with the DMA-train.

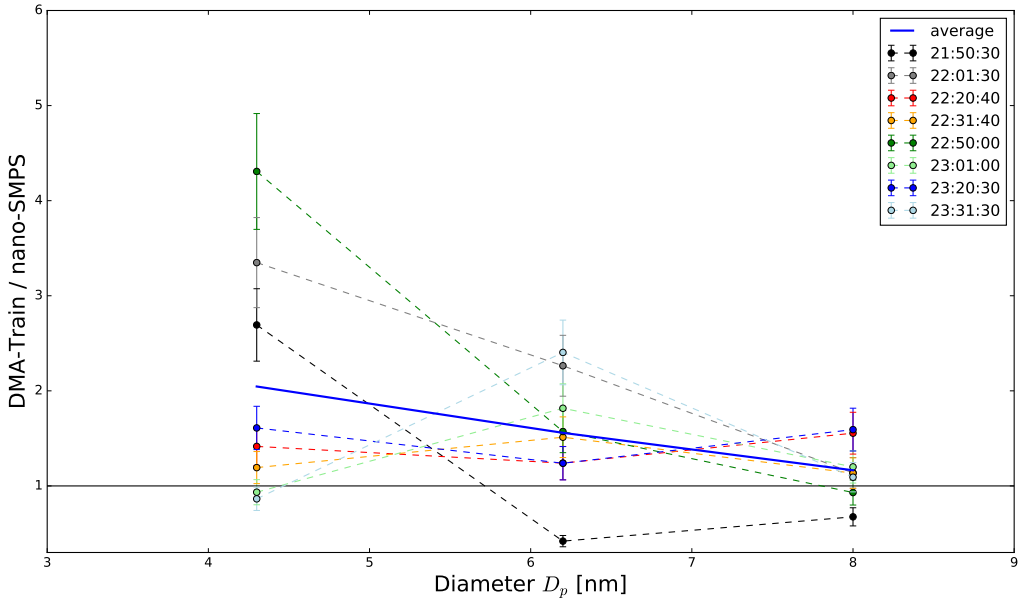

Figure 8.6: Ratios (dots and dashed lines) of particle concentrations obtained with both, DMA-train and nano-SMPS for various particle sizes below 10 nm during 8 periods of time. Respective start times of averaging processes are given in the legend, and each interval was set to 7 nano-SMPS measurement runs, which in return equal 6.5 minutes. The solid, blue line illustrates mean values of all depicted particle sizes and approaches 1 (solid, black line) for increasing diameters. Nano-SMPS concentrations exceed corresponding values of the DMA-train six times, and no noticeable time-dependency is present.

Conclusion

The fast-changing environment of freshly nucleated aerosol particles calls for high-time resolution measurements which provide correct size distributions starting at low single-digit nanometer ranges. Based on experiments described in this thesis corresponding computations are now also possible when operating a conventional DMPS-system, i.e. a particle source, charger, DMA and CPC, with particle-laden helium.

Initial Experiments targeting the calibration of the utilized DMA were achieved through the analysis of electrosprayed PSL-particles. Generation, sizing and detection of corresponding airborne aerosol particles carrying only one sphere proved to function properly. Analysis of helium-carried PSL-particles evoked a couple of difficulties, however, sufficient reasonable data was obtained. Comparison of the theoretical and experimentally achieved peak voltages showed a significant, but small gap. The DMA's classification length L=(15.9 ± 5.2) mm, whose value was determined by the PSL-particles' distribution, yields an elevated error in the resulting particle size magnification factor M_D=(1.16±0.18). If higher precision is needed, this inconvenient circumstance could be minimized through conduction of further experiments with different size standards than those used in this study.

Further investigations targeting the particles' charging state after penetration of the X-ray charger are crucial for these calculations. Implementation of an ion trap instead of an additional DMA significantly simplified the necessary setup and reduced the needed amount of helium. It is worth mentioning, however, that this new technique has the drawback of quantifying only the complete charged fraction, i.e. no information on positively/negatively charged particles is attained. Application to relative values for positively/negatively and singly/doubly charged particles, provided by Wiedensohler (1988), yield respective charging probabilities, which are higher by a factor of (1.148 ± 0.075), nevertheless.

Subsequent experiments on the transmission of the X-ray charger as well as the CPC's cut off function provided satisfying outcomes. The former was found to have an equivalent transmission length of L_{char}=(0.90 ± 0.25) m, the CPC's corresponding quantities are L_{act}=(0.26 ± 0.14) m and $D_{p,50}$=(3.68 ± 0.60) nm.

It is worth noting, however, that implementation of the found quantities into computations aiming for the retrieval of size distributions yield elevated uncertainties as well. Reduction of these errors is scarcly possible, since they solely are present due to the particle counters' errors. One remaining possibility is a less conservative assumption of their propagation to corresponding fitting parameters since their absolute values have been taken into account.

Comparative experiments of the DMA-train and nano-SMPS proved higher sensitivities of the former instrument for particles smaller than 5 nm in both studied concentration ranges. Elevated detection signals are especially present in fast-changing environments, thus pointing out the DMA-train's measurement principle's benefit.
Further experiments, however, are still necessary in order to find the factor(s), which cause existing concentration deviations. Aberrations at 6.2 nm and 8 nm above and below when analyzing tungsten oxide particles (high concentrations) raise as much question as the slow approximation towards 1 of related values depicting CLOUD11 data. As a summary, manifold questions regarding this topic are yet to be answered.

References

Allen, M. D. and O. G. Raabe (1985). Slip correction measurements of spherical solid aerosol particles in an improved millikan apparatus. *Aerosol Science and Technology 4*(3), 269–286.

Almeida, J., S. Schobesberger, A. Kürten, I. K. Ortega, O. Kupiainen-Määttä, A. P. Praplan, A. Adamov, A. Amorim, F. Bianchi, M. Breitenlechner, A. David, J. Dommen, N. M. Donahue, A. Downard, E. Dunne, J. Duplissy, S. Ehrhart, R. C. Flagan, A. Franchin, R. Guida, J. H. A. Hansel, M. Heinritzi, H. Henschel, T. Jokinen, H. Junninen, M. Kajos, J. Kangasluoma, H. Keskinen, A. Kupc, T. Kurtén, A. N. Kvashin, A. Laaksonen, K. Lehtipalo, M. Leiminger, J. Leppä, V. Loukonen, W. Makhmutov, S. Mathot, M. J. McGrath, T. Nieminen, T. Olenius, A. Onnela, T. Petäjä, F.Riccobono, I. Riipinen, M. Rissanen, L. Rondo, T. Ruuskanen, F. D. Santos, N. Sarnela, S. Schallhart, R. Schnitzhofer, J. H. Seinfeld, M. Simon, M. Sipilä, Y. Stozhkov, F. Stratmann, A. Tomé, J. Tröstl, G. Tsagkogeorgas, P. Vaattovaara, Y. Viisanen, A. Virtanen, A. Vrtala, P. E. Wagner, E. Weingartner, H. Wex, C. Williamson, D. Wimmer, P. Ye, T. Yli-Juuti, K. S. Carslaw, M. Kulmala, J. Curtius, U. Baltensperger, D. R. Worsnop, H. Vehkamäki, and J. Kirkby (2013). Molecular understanding of sulphuric acid–amine particle nucleation in the atmosphere. *Nature 502*, 359–363.

Alonso, M., Y. Kousaka, T. Nomura, N. Hashimoto, and T. Hashimoto (1997). Bipolar charging and neutralization of nanometer-sized aerosol particles. *Journal of Aerosol Science 28*(8), 1479 – 1490.

Als-Nielsen, J. and D. McMorrow (2011). *Elements of Modern X-ray Physics* (2 ed.). Wiley.

Brooks, R. A. and G. D. Chiro (1975). Beam hardening in x-ray reconstructive tomography. *Physics in Medicine and Biology 21*, 390–398.

Brunelli, N. A., R. C. Flagan, and K. P. Giapis (2009). Radial differential mobility analyzer for one nanometer particle classification. *Aerosol Science and Technology 43*(1), 53–59.

Burtscher, H. (1992). Measurement and characteristics of combustion aerosols with special consideration of photoelectric charging and charging by flame ions. *Journal of Aerosol Science 23*(6), 549–595.

Carslaw, K. S., L. A. Lee, C. L. Reddington, K. J. Pringle, A. Rap, P. M. Forster, G. W. Mann, D. V. Spracklen, M. T. Woodhouse, L. A. Regayre, and J. R. Pierce (2013). Large contribution of natural aerosols to uncertainty in indirect forcing. *Nature 503*, 67–71.

Chang, J. S., P. A. Lawless, and T. Yamamoto (1991). Corona discharge processes. *IEEE Transactions on Plasma Science 19*(6), 1152–1166.

Charlson, R. J. and S. Schwartz (1992). Climate forcing by anthropogenic aerosols. *Science 255*(5043), 423.

Covert, D., A. Wiedensohler, and L. Russell (1997). Particle charging and transmission efficiencies of aerosol charge neutralizes. *Aerosol Science and Technology 27*(2), 206–214.

Cruz, C. N. and S. N. Pandis (1997). A study of the ability of pure secondary organic aerosol to act as cloud condensation nuclei. *Atmospheric Environment 31*(15), 2205–2214.

Cunningham, E. (1910). On the velocity of steady fall of spherical particles through fluid medium. *The Royal Society 83*, 357–365.

Dunne, E. M., H. Gordon, A. Kürten, J. Almeida, J. Duplissy, C. Williamson, I. K. Ortega, K. J. Pringle, A. Adamov, U. Baltensperger, P. Barmet, F. Benduhn, F. Bianchi, M. Breitenlechner, A. Clarke, J. Curtius, J. Dommen, N. M. Donahue, S. Ehrhart, R. C. Flagan, A. Franchin, R. Guida, J. Hakala, A. Hansel, M. Heinritzi, T. Jokinen, J. Kangasluoma, J. Kirkby, M. Kulmala, A. Kupc, M. J. Lawler, K. Lehtipalo, V. Makhmutov, G. Mann, S. Mathot, J. Merikanto, P. Miettinen, A. Nenes, A. Onnela, A. Rap, C. L. S. Reddington, F. Riccobono, N. A. D. Richards, M. P. Rissanen, L. Rondo, N. Sarnela, S. Schobesberger, K. Sengupta, M. Simon, M. Sipilä, J. N. Smith, Y. Stozkhov, A. Tomé, J. Tröstl, P. E. Wagner, D. Wimmer, P. M. Winkler, D. R. Worsnop, and K. S. Carslaw (2016). Global atmospheric particle formation from cern cloud measurements. *Science*.

E. O. Knutson, K. T. W. (1975). Aerosol classification by electric mobility: apparatus, theory, and applications. *Journal of Aerosol Science 6*(6), 443–451.

Elzey, S., D. Tsai, L. Yu, M. Winchester, M. E. Kelley, and V. A. Hackley (2013). Real-time size discrimination and elemental analysis of gold nanoparticles using es-dma coupled to icp-ms. *Analytical and Bioanalytical Chemistry 405*(7), 2279–2288.

Facchini, M. C., S. Decesari, M. Rinaldi, C. Carbone, E. Finessi, M. Mircea, S. Fuzzi, F. Moretti, E. Tagliavini, D. Ceburnis, and C. D. O'Dowd (2008). Important source of marine secondary organic aerosol from biogenic amines. *Environmental Science & Technology 42*, 9116–9121.

Flagan, R. C. (2008). Differential mobility analysis of aerosols: A tutorial. *KONA Powder and Particle Journal 26*, 254–268.

Fuchs, N. A. (1963). On the stationary charge distribution on aerosol particles in bipolar ionic atmosphere. *Pure and Applied Geophysics 56*(1), 185–193.

Fuchs, N. A. (1964). *The Mechanics of Aerosols*, pp. 27. Pergamon Press.

Ghosh, D., D. Bergmann, R. Schwering, J. Wölk, R. Strey, S. Tanimura, and B. E. Wyslouzil (2010, January). Homogeneous nucleation of a homologous series of n-alkanes in a supersonic nozzle. *The Journal of Chemical Physics 132*(2), 024307–1–024307–17.

Gompertz, B. (1825). On the nature of the function expressive of the law of human mortality, and on a new mode of determining the value of life contingencies. *Philosophical Transactions of the Royal Society of London 115*, 513–583.

Gordon, H., K. Sengupta, A. Rap, J. Duplissy, C. Frege, C. Williamson, M. Heinritzi, M. Simon, C. Yan, J. Almeida, J. Tröstl, T. Nieminen, I. K. Ortega, R. Wagner, E. Dunne, A. Adamov, A. Amorim, A. Bernhammer, F. Bianchi, M. Breitenlechner, S. Brilke, X. Chen, J. Craven, A. Dias, S. Ehrhart, L. Fischer, R. F. A., Franchin, C. Fuchs, R. Guida, J. Hakala, C. Hoyle, T. Jokinen, H. Junninen, J. Kangasluoma, J. Kim, J. Kirkby, M. Krapf, A. Kürten, A. Laaksonen, K. Lehtipalo, V. Makhmutov, S. Mathot, U. Molteni, S. Monks, A. Onnela, O. Peräkylä, F. Piel, T. Petäjä, A. Praplan, K. Pringle, N. Richards, M. Rissanen, L. Rondo, N. Sarnela, S. Schobesberger, C. Scott, J. Seinfeld, S. Sharma, M. Sipilä, G. Steiner, Y. Stozhkov, F. Stratmann, A. Tomé, A. Virtanen, A. Vogel, A. Wagner, P. Wagner, E. Weingartner, D. Wimmer, P. Winkler, P. Ye, X. Zhang, A. Hansel, J. Dommen, N. Donahue, D. Worsnop, U. Baltensperger, M. Kulmala, J. Curtius, and K. Carslaw (2016). Reduced anthropogenic aerosol radiative forcing caused by biogenic new particle formation. *Proceedings of the National Academy of Sciences 113*(43), 12053–12058.

Gormley, P. G. and M. Kennedy (1949). Diffusion from a stream flowing through a cylindrical tube. *Proceedings of the Royal Irish Academy. Section A: Mathematical and Physical Sciences 52*, 163–169.

Grimm (2005). *Nano Aerosol Generator Model 7.860*.

Hermann, M., B. Wehner, O. Bischof, H.-S. Han, T. Krinke, W. Liu, A. Zerrath, and A. Wiedensohler (2007). Particle counting efficiencies of new TSI condensation particle counters. *Journal of Aerosol Science 38*(6), 674–682.

Hinds, W. C. (1999). *Aerosol Technology: Properties, Behavior, and Measurement of Airborne Particles* (2 ed.). John Wiley & Sons, INc.

Hoffmann, T., R. Bandur, and U. M. M. Linscheid (1998). Molecular composition of organic aerosols formed in the a-pinene/o3 reaction: Implications for new particle formation processes. *Journal of Geophysical Research: Atmospheres 103*(D19), 25569–25578.

Hogan, C. J. and P. Biswas (2008). Narrow size distribution nanoparticle production by electrospray processing of ferritin. *Journal of Aerosol Science 39*(5), 432–440.

Jacobson, M. Z. (2001). Strong radiative heating due to the mixing state of black carbon in atmospheric aerosols. *Nature 409*, 695–697.

Jaques, P. A. and C. S. Kim (2000). Measurement of total lung deposition of inhaled ultrafine particles in healty men and women. *Inhalation Toxicology 12*(8), 715–731.

Jones, A., D. Roberts, and A. Slingo (1994). A climate model study of indirect radiative forcing by anthropogenic sulphate aeorosols. *Nature 370*, 450–453.

Jousten, K. (2004). *Wutz Handbuch Vakuumtechnik* (8 ed.). Vieweg Taschenlexikon Technik.

J.P. Santos, J. P., E. H. nón, E. Ramiro, and M. Alonso (2009). Performance evaluation of a high-resolution parallel-plate differential mobility analyzer. *Atmospheric Chemistry and Physics 9*(7), 2419–2429.

Kallinger, P. and W. W. Szymanski (2015). Experimental determination of the steady-state charging probabilities and particle size conservation in non-radioactive and radioactive bipolar aerosol chargers in the size range of 5–40 nm. *Journal of Nanoparticle Research 17*(4).

Kannosto, J., A. Virtanen, M. Lemmetty, J. M. Mäkela, J. Keskinen, H. Junninen, T. Hussein, P. Aalto, and M. Kulmala (2008). Mode resolved density of atmospheric aerosol particles. *Atmospheric Chemistry and Physics 8*, 5327–5337.

Kim, J. H., G. Mulholland, S. R. Kukuck, and D. Y. H. Pui (2005). Slip correction measurements of certified psl nanoparticles using a nanometer differential mobility analyzer (nano-dma) for knudsen number from 0.5 to 83. *Journal of Research of the National Institute of Standards and Technology 110*(1), 31–54.

Kirkby, J. (2011). Role of sulphuric acid, ammonia and galactic cosmic rays in atmospheric aerosol nucleation. *Nature 476*, 429–4333.

Kleinman, L. I., P. H. Daum, Y.-N. Lee, E. R. Lewis, A. J. S. III, G. I. Senum, S. R. Springston, J. Wang, J. Hubbe, J. Jayne, Q. Min, S. S. Yum, and G. Allen (2012). Aerosol concentration and size distribution measured below, in, and above cloud from the doe g-1 during vocals-rex. *Atmospheric Chemistry and Physics 12*(1), 207–223.

Kousaka, Y., K. Okuyama, M. Adachi, and T. Mimura (1986). Effect of brownian diffusion on electrical classification of ultrafine aerosol particles in differential mobility analyzer. *Journal of Chemical Engineering of Japan 19*(5), 401–407.

Kulmala, M., J. Kontkanen, H. Junninen, K. Lehtipalo, H. E. Manninen, T. Nieminen, T. Petäjä, M. Sipilä, S. Schobesberger, P. Rantala, A. Franchin, T. Jokinen, E. Järvinen, M. Äijälä, J. Kangasluoma, J. Hakala, P. P. Aalto, P. Paasonen, J. Mikkilä, J. Vanhanen, J. Aalto, H. Hakola, U. Makkonen, T. Ruuskanen, R. L. Mauldin, J. Duplissy, H. Vehkamäki, J. Bäck, A. Kortelainen, I. Riipinen, T. Kurten, M. V. Johnston, J. N. Smith, M. Ehn, T. F. Mentel, K. E. J. Lehtinen, A. Laaksonen, V. Kerminen, and D. R. Worsnop (2013). Direct observations of atmospheric aerosol nucleation. *Science 339*(6122), 943–946.

Kulmala, M., L. Laakso, K. E. J. Lehtinen, I. Riipinen, M. Dal Maso, T. Anttila, V.-M. Kerminen, U. Hõrrak, M. Vana, and H. Tammet (2004). Initial steps of aerosol growth. *Atmospheric Chemistry and Physics 4*(11/12), 2553–2560.

Kulmala, M., T. Petäjä, T. Nieminen, M. Sipilä, H. E. Manninen, K. Lehtipalo, M. D. Maso, P. P. Aalto, H. Junninen, P. Paasonen, I. Riipinen, K. E. J. Lehtinen, A. Laaksonen, and V.-M. Kerminen (2012). Measurement of the nucleation of atmospheric aerosol particles. *Nature Protocols 7*(9), 1651–1667.

Kupc, A., A. Amorim, J. Curtius, A. Danielczok, J. Duplissy, S. Ehrhart, H. Walther, L. Ickes, J. Kirkby, A. Kürten, J. Lima, S. Mathot, P. Minginette, A. Onnela, L. Rondo, and P. Wagner (2011). A fibre-optic {UV} system for {H2SO4} production in aerosol chambers causing minimal thermal effects. *Journal of Aerosol Science 42*(8), 532–543.

Lehtinen, K. E., M. D. Maso, M. Kulmala, and V. Kerminen (2007). Estimating nucleation rates from apparent particle formation rates and vice versa: Revised formulation of the kerminen–kulmala equation. *Journal of Aerosol Science 38*(9), 988–994.

Lehtipalo, K., J. Leppä, J. Kontkanen, J. Kangasluoma, A. Franchin, D.Wimmer, S. Schobesberger, H. Junninen, T. Petäjä, M. Sipilä, J. Mikkilä, J.Vanhanen, D. R. Worsnop, and M. Kulmala (2014). Methods for determining particle size distribution and growth rates between 1 and 3 nm using the particle size magnifier. *Boreal Environment Research 19 (suppl. B)*, 215–236.

Li, Z. and H. Wang (2003). Drag force, diffusion coefficient, and electric mobility of small particles. i. theory applicable to the free-molecule regime. *American Physical Society 68*(6).

Liebermann, M. A. and A. J. Lichtenberg (2005). *Principles of Plasma Discharges and Materials Processing* (2 ed.). John Wiley & Sons.

Liu, B. Y. H. (1975). Aerosol generation, measurement, sampling, and analysis. In *Fine Particles*. Academic Press, Inc.

M. Gamero-Castaño, J. F. d. l. M. (2000). Mechanisms of electrospray ionization of singly and multiply charged salt clusters. *Analytica Chimica Acta 406*, 67–91.

Massarczyk, R., P. Chu, S. R. Elliott, and K. Rielage (2016). Paschen's law studies in cold gases.

McMurry, P. H., K. S. Woo, R. Weber, D. Chen, and D. Y. H. Pui (2000). Size distributions of 3–10 nm atmospheric particles: implications for nucleation mechanisms. *Philosophical Transactions of the Royal Society of London A: Mathematical, Physical and Engineering Sciences 358*(1775), 2625–2642.

Merikanto, J., D. V. Spracklen, G. W. Mann, S. J. Pickering, and K. S. Carslaw. (2009). Impact of nucleation on global ccn. *Atmospheric Chemistry and Physics 9*(21), 8601–8616.

Millikan, R. A. (1913). On the elementary electrical charge and the avogadro constant. *Phys. Rev. 2*, 109–143.

Mäkelä, J. M., P. Aalto, and V. Jokinen (1997). Observations of ultrafine aerosol particle formation and growth in boreal forest. *Geophysical Research Letters 24*, 1219–1222.

Mäkelä, J. M., M. Riihelä, A. Ukkonen, V. Jokinen, and J. Keskinen (1996). Comparison of mobility equivalent diameter with kelvin-thomson diameter using ion mobility data. *The Journal of Chemical Physics 105*(4), 1562–1571.

Novakov, T. and J. Penner (1992). Large contribution of organic aerosols to cloud-condensation-nuclei concentrations. *Nature 365*, 823–826.

Okazaki, K. and K. Willeke (1987). Transmission and deposition behavior of aerosols in sampling inlets. *Aerosol Science and Technology 7*(3), 275–283.

Paschen, F. (1889). Ueber die zum funkenübergang in luft, wasserstoff und kohlensäure bei verschiedenen drucken erforderliche potentialdifferenz. *Annalen der Physik 273*(5), 69–96.

Pearson, K. (1900). On the criterion that a given system of deviations from the probable in the case of a correlated system of variables is such that it can be reasonably supposed to have arisen from random sampling. *The London, Edinburgh, and Dublin Philosophical Magazine and Journal of Science 50*(302), 157–175.

Perry, R. H. (1997). *Perry's Chemical Engineers' Handbook*, Volume 7, Chapter 6, pp. 6–21. Mc Graw-Hill Companies.

Peters, C., J. Gebhart, C. Roth, and S. Sehrt (1991). Test of high sensitive laser particle counters with psl-aerosols and a cnc reference. *Journal of Aerosol Science 22*(Supplement 1), 363–366. Proceedings of the 1991 European Aerosol Conference.

Qi, X. M., A. J. Ding, W. Nie, T. Petäjä, V.-M. Kerminen, E. Herrmann, Y. N. Xie, L. F. Zheng, H. Manninen, P. Aalto, J. N. Sun, Z. N. Xu, X. G. Chi, X. Huang, M. Boy, A. Virkkula, X. Q. Yang, C. B. Fu, and M. Kulmala (2015). Aerosol size distribution and new particle formation in the western yangtze river delta of china: 2 years of measurements at the sorpes station. *Atmospheric Chemistry and Physics 15*(21), 12445–12464.

Reischl, G., J. Mäkelä, R. Karch, and J. Necid (1996). Bipolar charging of ultrafine particles in the size range below 10 nm. *Journal of Aerosol Science 27*(6), 931–949.

Riccobono, F., S. Schobesberger, C. E. Scott, J. Dommen, I. K. Ortega, L. Rondo, J. Almeida, A. Amorim, F. Bianchi, M. Breitenlechner, A. David, A. Downard, E. M. Dunne, J. Duplissy, S. Ehrhart, R. C. Flagan, A. Franchin, A. Hansel, H. Junninen, M. Kajos, H. Keskinen, A. Kupc, A. Kürten, A. N. Kvashin, A. Laaksonen, K. Lehtipalo, V. Makhmutov, S. Mathot, T. Nieminen, A. Onnela, T. Petäjä, A. P. Praplan, F. D. Santos, S. Schallhart, J. H. Seinfeld, M. Sipilä, D. V. Spracklen, Y. Stozhkov, F. Stratmann, A. Tomé, G. Tsagkogeorgas, P. Vaattovaara, Y. Viisanen, A. Vrtala, P. E. Wagner, E. Weingartner, H. Wex, D. Wimmer, K. S. Carslaw, J. Curtius, N. M. Donahue, J. Kirkby, M. Kulmala, D. R. Worsnop, and U. Baltensperger (2014). Oxidation products of biogenic emissions contribute to nucleation of atmospheric particles. *Science 344*(6185), 717–721.

Rosen, J. M. and D. J. Hofmann (1986, Feb). Optical modeling of stratopheric aerosols: present status. *Applied Optics 25*(3), 410–419.

Schmid, O., M. B. Trueblood, N. Gregg, D. E. Hagen, and P. D. Whitefield (2002). Sizing of aerosol in gases other than air using a differential mobility analyzer. *Aerosol Science and Technology 36*(3), 351–360.

Shi, J. P., D. E. Evans, A. Khan, and R. M. Harrison (2001). Sources and concentration of nanoparticles (¡10 nm diameter) in the urban atmosphere. *Atmospheric Environment 35*(7), 1193–1202.

Sihto, S.-L., M. Kulmala, V.-M. K. M., D. Maso, T. Petäjä, I. Riipinen, H. Korhonen, F. Arnold, R. Janson, M. Boy, A. Laaksonen, and K. E. J. Lehtinen (2006). Atmospheric sulphuric acid and aerosol formation: implications from atmospheric measurements for nucleation and early growth mechanisms. *Atmospheric Chemistry and Physics 6*(12), 4079–4091.

Steiner, G., M. Attoui, M. Sipilä, G. Reischl, D. Wimmer, and M. Kulmala (2006). Performance evaluation of the grimm 7.860 wox generator. Technical report, Universität Wien and Universite Paris XII Val de Marne and University of Helsinki.

Stolzenburg, D., G. Steiner, and P. M. Winkler (2017). A dma-train for precision measurement of sub-10nm aerosol dynamics. *Atmospheric Measurement Techniques 10*(4), 1639–1651.

Stolzenburg, M. R. and P. H. McMurry (2008). Equations governing single and tandem DMA configurations and a new lognormal approximation to the transfer function. *Aerosol Science and Technology 42*(6), 421–432.

Sun, Y., W. Du, P. Fu, Q. Wang, J. Li, X. Ge, Q. Zhang, C. Zhu, L. Ren, W. Xu, J. Zhao, T. Han, D. Worsnop, and Z. Wang (2016). Primary and secondary aerosols in beijing in winter: sources, variations and processes. *Atmospheric Chemistry and Physics 16*, 8309–8329.

Taylor, G. (1964). Disintegration of water drops in an electric field. *Proceedings of the Royal Society of London A: Mathematical, Physical and Engineering Sciences 280*(1382), 383–397.

Tröstl, J., W. K. Chuang, H. Gordon, M. Heinritzi, C. Yan, U. Molteni, L. Ahlm, C. Frege, F. Bianchi, R. Wagner, M. Simon, K. Lehtipalo, C. Williamson, J. S. Craven, J. Duplissy, A. Adamov, J. Almeida, A. Bernhammer, M. Breitenlechner, S. Brilke, A. Dias, S. Ehrhart, R. C. Flagan, A. Franchin, C. Fuchs, R. Guida, M. Gysel, A. Hansel, C. R. Hoyle, T. Jokinen, H. Junninen, J. Kangasluoma, H. Keskinen, J. Kim, M. Krapf, A. Kürten, A. Laaksonen, M. Lawler, M. Leiminger, S. Mathot, O. Möhler, T. Nieminen, A. Onnela, T. Petäjä, F. M. Piel, P. Miettinen, M. P. Rissanen, L. Rondo, N. Sarnela, S. Schobesberger, K. Sengupta, M. Sipilä, J. N. Smith, G. Steiner, A. Tome, A. Virtanen, A. C. Wagner, E. Weingartner, D. Wimmer, P. M. Winkler, P. Ye, K. S. Carslaw, J. Curtius, J. Dommen, J. Kirkby, M. Kulmala, I. Riipinen, D. R. Worsnop, N. M. Donahue, and U. Baltensperger (2016). The role of low-volatility organic compounds in initial particle growth in the atmosphere. *Nature 53*(7604), 527–531.

TSI (2006). *Model 3776 - Ultrafine Condensation Particle Counter*.

Vaaraslahti, K., A. Laitinen, and J. Keskinen (2002). Spray charging of droplets in a wet scrubber. *Journal of the Air & Waste Management Association 52*(2), 175–180.

Wang, L., A. F. Khalizov, J. Zheng, W. Xu, Y. Ma, V. Lal, and R. Zhang (2010). Atmospheric nanoparticles formed from heterogeneous reactions of organics. *Nature Geoscience 3*, 238–242.

Wang, S. C. and R. C. Flagan (1990). Scanning electrical mobility spectrometer. *Aerosol Science and Technology 13*(2), 230–240.

Wang, X., J. Chen, T. Cheng, R. Zhang, and X. Wang (2014). Particle number concentration, size distribution and chemical composition during haze and photochemical smog episodes in shanghai. *Journal of Environmental Sciences 26*(9), 1894–1902.

Wiedensohler, A. (1988). An approximation of the bipolar charge distribution. *Aerosol Science and Technology 19*(3), 387–389.

Winklmayr, W., G. Reischl, A. Lindner, and A. Berner (1991). A new electromobility spectrometer for the measurement of aerosol size distributions in the size range from 1 to 1000 nm. *Journal of Aerosol Science 22*(3), 289–296.

Index of Figures

Index of Tables